Acoustofluidique de microbulles non-sphériques : physique et interaction mécanique avec des cellules biologiques

Maxime Fauconnier

To cite this version:

Maxime Fauconnier. Acoustofluidique de microbulles non-sphériques : physique et interaction mécanique avec des cellules biologiques. Acoustics [physics.class-ph]. Université de Lyon, 2021. English. NNT : 2021LYSE1242 . tel-03678056

HAL Id: tel-03678056
https://theses.hal.science/tel-03678056

Submitted on 25 May 2022

N° d'ordre NNT : 2021LYSE1242

Thèse de Doctorat

en vue de l'obtention du grade de

Docteur de l'Université de Lyon

Discipline : **Acoustique**

Laboratoire d'Applications Thérapeutiques des Ultrasons

École Doctorale MEGA n°162
Mécanique, Énergétique, Génie civil, Acoustique

Présentée et soutenue publiquement le 19 novembre 2021, par

Maxime Fauconnier

Acoustofluidics of nonspherical microbubbles: physics and mechanical interaction with biological cells.

Directeur de Thèse : Jean-Christophe Béra
Co-directeur de Thèse : Claude Inserra

Devant la commission d'examen formée de :

Docteure	Hélène Delanoë-Ayari	*Université de Lyon, France*	Examinatrice
Professeur	Bertrand Dubus	*Université de Lille, France*	Rapporteur
Docteure	Valeria Garbin	*Université de Technologie de Delft, Pays-Bas*	Examinatrice
Professeur	Michiel Postema	*Université de Tampere, Finlande*	Rapporteur

Laboratoire d'Applications
Thérapeutiques des Ultrasons
151 Cours Albert Thomas
69003 Lyon, France

École doctorale MEGA n°162
37 Avenue Jean Capelle
69100 Villeurbanne, France

Université Claude Bernard – LYON 1

Président de l'Université	M. Frédéric FLEURY
Président du Conseil Académique	M. Hamda BEN HADID
Vice-Président du Conseil d'Administration	M. Didier REVEL
Vice-Président du Conseil des Etudes et de la Vie Universitaire	M. Philippe CHEVALLIER
Vice-Président de la Commission de Recherche	M. Petru MIRONESCU
Directeur Général des Services	M. Pierre ROLLAND

COMPOSANTES SANTE

Département de Formation et Centre de Recherche en Biologie Humaine	Directrice : Mme Anne-Marie SCHOTT
Faculté d'Odontologie	Doyenne : Mme Dominique SEUX
Faculté de Médecine et Maïeutique Lyon Sud - Charles Mérieux	Doyenne : Mme Carole BURILLON
Faculté de Médecine Lyon-Est	Doyen : M. Gilles RODE
Institut des Sciences et Techniques de la Réadaptation (ISTR)	Directeur : M. Xavier PERROT
Institut des Sciences Pharmaceutiques et Biologiques (ISBP)	Directrice : Mme Christine VINCIGUERRA

COMPOSANTES & DEPARTEMENTS DE SCIENCES & TECHNOLOGIE

Département Génie Electrique et des Procédés (GEP)	Directrice : Mme Rosaria FERRIGNO
Département Informatique	Directeur : M. Behzad SHARIAT
Département Mécanique	Directeur M. Marc BUFFAT
Ecole Supérieure de Chimie, Physique, Electronique (CPE Lyon)	Directeur : Gérard PIGNAULT
Institut de Science Financière et d'Assurances (ISFA)	Directeur : M. Nicolas LEBOISNE
Institut National du Professorat et de l'Education	Administrateur Provisoire : M. Pierre CHAREYRON
Institut Universitaire de Technologie de Lyon 1	Directeur : M. Christophe VITON
Observatoire de Lyon	Directrice : Mme Isabelle DANIEL
Polytechnique Lyon	Directeur : Emmanuel PERRIN
UFR Biosciences	Administratrice provisoire : Mme Kathrin GIESELER
UFR des Sciences et Techniques des Activités Physiques et Sportives (STAPS)	Directeur : M. Yannick VANPOULLE
UFR Faculté des Sciences	Directeur : M. Bruno ANDRIOLETTI

Je vous souhaite des rêves à n'en plus finir et l'envie furieuse d'en réaliser quelques-uns.

Jacques Brel

Acknowledgments

Please excuse me for what I will say, but all of you whom I must thank do not make my life easier. You should understand that this specific acknowledgments part is certainly not the easiest one to write, and as a consequence, without you, this very difficult writing exercise would never take place. Also, I have to say that without all of you, this thesis work and manuscript would obviously not have seen the day light. For this, I would like to thank you very much with all my heart. So let me give it a try, I will do my best.

Dear Jean-Christophe and Claude, you should know that meeting you, learning acoustics from you and then spending three years working with you on such an exciting topic was most likely one of the most enjoying experience I have ever lived. I could never have hoped for greater thesis supervisors than you two.

Jean-Christophe, first of all, I will never thank you enough for having given me the opportunity to take part five years ago to this Master program in Sciences of Acoustics. You gave me the taste of research, the scientific curiosity, the will for education and the sense of experiments. During this thesis, I had the most beautiful experimental times in your company, when, late in the days of manipulation, we used to spontaneously meet in order to provide an explanation for all the mechanics of biological cells and, sometimes, for the inexplicable. I will terribly miss those moments. You are a person of a rare kindness. I am very certain your heart is as big as your altruism and goodness. Thank you for your spontaneity, your unfailing enthusiasm, your sincerity, your warm welcome.

Claude, during these years, you have been a friend to me. Thank you very much for this true friendship. In you, I also found an eloquent and communicative teammate, an excellent didact, an unconditional beer-time companion, a symposium fellow whether in Milan or in Lille. Thank you for all that, I had amazing times with you. Again, I will extremely miss those moments. I will also miss very much "to guess the vibration sequences of our bubbles, while marveling noisily in front of so much beauty", as you said so well. You never count your time or energy to help whoever. Always resourceful, thoughtful, energetic, kind, sincere and patient, I truly believe your career as a teacher-researcher will be outstanding. I will also miss our morning coffee, your excellent humor and the contagiousness of your daily enthusiasm and desire for research. I will actually miss everything of you. Farewell my dear friend !

I would like to thank Michiel Postema and Bertrand Dubus for having accepted to be reviewers of this thesis, as well as Hélène Delanoë-Ayari and Valeria Garbin for having accepted to be part of this thesis' jury.

To all the LabTAU teammates, I thank you very much for your friendship, for all these very interesting and funny lunch times, these coffee breaks, these lab-days, those moments of laughter and discovery. In particular, I thank Jacqueline and Magali who taught me the little I know in biology, but also for the great discussions on plants and on everything and nothing, Catherine, Leila and Sandrine without who the Safir platform and other administrative stuffs would have been a nightmare, and Cyril Lafon for his welcome. Cyril, you are very lucky to be in charge of such an amazing, high-quality and friendly laboratory. Sometimes I wonder, how am I going to find another professional place so good afterwards. I will probably have to implore the gods of fortune.

To my family and friends, I immensely thank you. I thank you for your love, your kindness and the interest you have always demonstrated concerning my thesis topic. Your support meant a lot to me.

Mom and Dad, you are fabulous as always. Thank you very much for all your generosity, careful attention and love. Thank you for your support, your always wise advices, and, Dad, for having advised me to test my biological cells for mycoplasmas. Mamy, I will always remember the first time I explained you the story of my whole thesis. You are always enthusiastic, attentive and understanding. You are my confidant. What can I say else than, stay as you are. I love you all.

My dear Sonia, thank you very much. During these three doctoral years, and even more these last months, you have done everything you could to help me focusing on this thesis work. You have been my coach, my cook, my postwoman, my nurse, my courier, my waker. You have been my full-time everything. You are my love. Thank you for always believing in me.

Soon, a page will turn. Many thanks to everyone who took part in one way or another. A new one is about to be written. Let us hope it will be as great as this one was. I wish you all the best. See you around fellows, and as would say Albert Einstein, *“Learn from yesterday, live for today, hope for tomorrow. The important thing is not to stop questioning.”*

Extended summary

The following extended summary reveals the contents and results of each of the four chapters constituting this thesis entitled: "Acoustofluidics of nonspherical microbubbles: physics and mechanical interaction with biological cells." This part, which is not necessary to understand the core of the manuscript, can be entirely dismissed whether the reader wishes to discover the results as and when reading.

As a starter of this thesis manuscript, chapter 1 takes us on a journey into the scientific, medical and industrial worlds of bubbles. It establishes the context in which this thesis takes part by defining and discussing concepts of cavitation, nonspherical bubble, microstreaming and sonoporation. To be exact, section 1.1 defines the terms bubble and cavitation and discusses their adversities and fortunate applications in which they take place in the industrial and medical fields, the latter being our main interest in the framework of this thesis. Foremost, it was their large mismatch of acoustic impedance with a surrounding fluid that was taken advantage of, when bubbles began to be used as ultrasound contrast agents in medical imaging. Tuned with specific gases and coatings, they could serve a large spectrum of diagnostic purposes. It was not before much later that they were found to be also able to serve many therapeutic uses from their capacity in producing huge amount of acoustic, mechanical and thermal energy, whether they drift, oscillate or collapse under the action of ultrasounds or lasers. The different ways in which bubbles can be created, and how this might affect their nature and their response to ultrasounds, will also be presented, which will then lead us to the next section 1.2 that concerns the bubble's behavior when animated by an ultrasound field. While every theoretical and a large part of experimental works consider the bubble as free of any contact, this thesis work especially takes its interest in the study of a wall-attached bubble. Nevertheless, comparisons between our experimental wall-attached bubble and the theory of free bubble will be occasional throughout this manuscript, so that the wall effect may be highlighted. The stability of the bubble interface is also discussed here, which will then bring us to section 1.3 on the nonspherical dynamics of a bubble. These shape deformations arise from the parametric instability of the bubble interface, occurring above a critical threshold in pressure that especially depends on the bubble size and the driving frequency. We will see how these nonspherical shapes behave whether in the case of a free bubble or a constrained one and how they can be mathematically described with the spherical-coordinate harmonics. These harmonic functions are indexed according to two inherent integers, a degree n and an order m, and take the names of zonal, tesseral and sectoral depending on the relation between n and m and thus, as we shall see, on their geometrical features. Their impact on the surrounding fluid is then detailed, relying on the plentiful literature on bubble-induced microstreaming with section 1.4. This introducing chapter ends with a large overview on sonoporation in section 1.5. The possible involved mechanisms, the measuring techniques and the existing experimental and theoretical works are brought to light. The emphasis is done on the difference between investigations performed at the single-cell and multi-cells scales, thus highlighting the interest of our experimental study at the scale of one single bubble and one single cell.

With that background in mind, the experimental investigation on the dynamics of a single bubble attached to a wall, the triggering, the detection and the identification of its nonspherical modes, can be initiated with chapter 2. On the menu, the experimental setup allowing the bubble high frame rate visualization from a top-view perspective is first described in details as a starter, in section 2.1. A small parenthesis showing some bubbles from a double top- and side-view will be made in order to facilitate the comprehension of the system under study, yet limited afterwards to a single top-view, failing to be convenient at a later stage. It is followed by section 2.2 that reports the main results of this chapter. Our method for identifying and qualitatively measuring the nonspherical modes is there presented. It allows, along a modulated driving acoustic pressure, to look into the pressure instability thresholds of the bubble nonspherical modes. As a centerpiece, a spectral splitting, the so-called nondegeneracy, of nonspherical modes is demonstrated, which comes as a contradiction against the theory of free bubbles. Some interpretations based on the bubble nonspherical geometry allow to explain the preferential appearance of specific modes, as well as the coexistence of zonal and sectoral modes, conditioned by their respective degree of spherical harmonics. Besides, appendix A.1 gives a complementary analysis on the dynamics of a wall-attached bubble but visualized from a side-view, which comes reinforcing our interpretations and modal identifications asserted before.

After that the bubble dynamics has been a little unveiled, the manuscript pursues with the bubble-induced effects on the surrounding fluid in chapter 3. In a first step, the experimental setup and procedure are introduced in section 3.1, as well as some details on how the fluid flow is visualized and assessed in the bubble's neighborhood. The second and last part, section 3.2, gathers all our results. There, the formation of specific patterns of microstreaming is explained on the basis of the bubble modal content. With this aim, a quantified description of the bubble dynamics is actually required, while it was previously only investigated in a rather qualitative way. The correlation of these fluid flows with the bubble activity is explained for five different cases of modal configuration: a zonal mode only, a sectoral mode only, a tesseral mode only, combined zonal and sectoral modes, and lastly, combined tesseral and sectoral modes. In the particular and widely investigated case of combined zonal and sectoral modes, the preferential appearance of flower-shaped and star-shaped streaming patterns is explained on the basis of modal amplitudes, their relative phase shift and the strength of their interaction. From time to time, this extensive analysis is supported by illustrated examples of our calculation method, while the analytic expressions are given step by step throughout the different subsections. Similarly as before, some occasional visualizations from a side-view of the bubble and its associated streaming are presented apart, in appendix A.2. It allowed to demonstrate that sectoral modes generate an antifountain-like streaming with a significantly wider area of action than zonal modes and their fountain-like streaming.

Last but not least, chapter 4 gathers the knowledge now acquired on a wall-attached bubble undergoing nonspherical modes to evaluate its effects on a nearby biological cell. To address this issue, two cellular models described in section 4.1 are selected: a mouse oocyte and a human megakaryocyte. While they were both of them designated as good candidates for the purpose of our investigation, oocytes are quickly cast aside due to the unexpected sanitary crisis, and hence supplying difficulties. Accordingly, the study will be limited in the forthcoming to megakaryocytes. Nevertheless, some scarce results on oocytes are presented out of this chapter, in appendix B. After exposing the good practices concerning the preparation of megakaryocytes comes section 4.2 on the experimental methodology, in which our methods employed for manipulating the cells and for assessing their mechanical response are detailed. In addition, a little aside comes up with a characterization of the culture medium employed instead of water as experimenting medium. All this being now settled, section 4.3 can begin. Starting with a brief investigation of the pressure instability thresholds for our bubble now surrounded by culture medium, the results on the mechanical interaction between a biological cell and a bubble arrive then. First, their coupled dynamics is studied at the acoustic time scale through the bubble pushing-pulling action on the cell, the emphasis being on sectoral modes. With the aim to measure the cell elasticity, this periodic motion is then taken advantage of in order to promote the propagation of shear waves within the cell. On the other hand, at the fluidic time scale, the tumbling motion of suspended cells trapped on the stagnation points of the bubble-induced streaming is studied. Several attempts for internalizing fluorescent particles (propidium iodide) were undertaken, but without success. However, the pushing-pull action of the bubble on the cell could be clearly observed qualitatively, as well as the detection and identification of significant and stable nonspherical modes. As a conclusion, the cellular sonoporation of an adhering nearby cell induced by a nonspherically oscillating microbubble is not immediate. Impossible seems a bit impulsive as a conclusion, but certainly very compromised with the experimental configuration as it is.

Résumé étendu

Le résumé étendu qui suit révèle le contenu et les résultats de chacun des quatre chapitres constituant cette thèse intitulée: “Acoustofluidique de microbulles non-sphériques : physique et interaction mécanique avec des cellules biologiques.” Cette partie, qui n’est pas nécessaire pour comprendre le coeur du manuscrit, peut être entièrement laissée de côté si le lecteur souhaite découvrir les résultats au fur et à mesure de sa lecture.

Au commencement de ce manuscrit de thèse, le chapitre 1 nous emmène en voyage dans les mondes scientifique, médical et industriel des bulles. Il établit le contexte dans lequel s’inscrit cette thèse en définissant et en discutant les concepts de cavitation, bulle non-sphérique, microstreaming et sonoporation. Plus exactement, la section 1.1 définit les termes bulle et cavitation, et discute des circonstances défavorables et des applications bénéfiques dans lesquelles ces bulles prennent place, autant dans le domaine industriel que médical, ce dernier étant notre principal intérêt dans le cadre de cette thèse. En premier lieu, c’est grâce à la différence importante qui existe entre leur impédance acoustique et celle du fluide environnant que les bulles ont commencé à être utilisées comme agents de contraste ultrasonores à des fins d’imagerie médicale. Perfectionnées avec des gaz et des enveloppes spécifiques, elles peuvent être employées à des fins très variées de diagnostics. Ce n’est que bien plus tard que leur utilité dans de nombreuses utilisations thérapeutiques est révélée, de par leur capacité à produire d’énormes quantités d’énergie acoustique, mécanique et thermique, que ces bulles soient propulsées, oscillent ou implosent sous l’action d’ultrasons ou de lasers pulsés. Les différentes manières dont les bulles peuvent être créées, et en quoi cela peut affecter leur nature et leur réponse aux ultrasons, seront également présentées, ce qui nous mènera ensuite à la section 1.2 qui concerne le comportement de la bulle lorsqu’elle est animée par un champ ultrasonore. Alors que l’ensemble des travaux théoriques et une grande partie des travaux expérimentaux existants considèrent la bulle comme libre de tout contact, ce travail de thèse s’intéresse plus particulièrement à l’étude d’une bulle attachée à la paroi. Néanmoins, des comparaisons entre notre bulle expérimentale attachée et la théorie des bulles libres seront occasionnelles tout au long de ce manuscrit, afin que l’effet de la paroi puisse être mis en évidence. La stabilité de l'interface de la bulle est également discutée ici, ce qui nous amènera ensuite à la section 1.3 sur la dynamique non-sphérique d'une bulle. Ces déformations de surface résultent de l'instabilité paramétrique de l'interface de la bulle, se produisant au-dessus d'un seuil critique de pression qui dépend notamment de la taille de la bulle et de la fréquence d'excitation. Nous verrons comment ces formes non-sphériques se comportent que ce soit dans le cas d'une bulle libre ou contrainte et comment elles peuvent être décrites mathématiquement avec les harmoniques sphériques. Ces fonctions harmoniques sont indexées selon deux entiers inhérents, un degré n et un ordre m, et prennent les noms de zonal, tesséral et sectoral selon la relation entre n et m et ainsi, comme on le verra, selon leurs caractéristiques géométriques. Leur impact sur le fluide environnant est ensuite détaillé, en s'appuyant sur l'abondante littérature concernant le microstreaming induit par les bulles avec la section 1.4. Ce chapitre d'introduction se termine par un large aperçu de la sonoporation détaillé dans la section 1.5. Les mécanismes possiblement impliqués, les techniques de mesure et les travaux expérimentaux et théoriques existants sont présentés. L'accent est mis sur la différence entre les investigations réalisées à l'échelle unicellulaire et multicellulaire, mettant ainsi en évidence l'intérêt de notre étude expérimentale à l'échelle d'une seule bulle et d'une seule cellule.

Une fois ces concepts acquis, l'investigation expérimentale de la dynamique d'une bulle accrochée à une paroi, le déclenchement, la détection et l'identification de ses modes non-sphériques, peut être initiée avec le chapitre 2. Au menu, le dispositif expérimental permettant la visualisation à haute fréquence d'une bulle dans une perspective en vue de dessus est d'abord décrit en détail, dans la section 2.1. Une petite parenthèse montrant quelques bulles dans une vue double (dessus et côté) est faite afin de faciliter la compréhension du système à l'étude, mais limitée par la suite à une seule vue de dessus, à défaut de convenir à un stade ultérieur. Elle est suivie de la section 2.2 qui rapporte les principaux résultats de ce chapitre. Notre méthode d'identification et de mesure qualitative des modes non-sphériques y est présentée. Elle permet, le long d'une modulation de la pression acoustique d'excitation, d'étudier les seuils d'instabilité de pression des modes non-sphériques de la bulle. En tant que résultat principal, une division spectrale, la soi-disant non-dégénérescence, des modes non-sphériques est démontrée, ce qui est en contradiction avec la théorie des bulles libres. Certaines interprétations basées sur la géométrie non-sphérique de la bulle permettent d'expliquer l'apparition préférentielle de modes spécifiques, ainsi que la coexistence des modes zonaux et sectoraux, conditionnés par leur degré respectif d'harmoniques sphériques. Par ailleurs, l'appendice A.1 donne une analyse complémentaire sur la dynamique d'une bulle toujours accrochée à une paroi mais visualisée latéralement, ce qui vient renforcer nos interprétations et identifications modales affirmées précédemment.

Après que la dynamique des bulles ait été un peu dévoilée, le manuscrit poursuit avec les effets induits par les bulles sur le fluide environnant avec ce chapitre 3. Dans une première étape, le montage expérimental et la procédure sont présentés dans la section 3.1, ainsi que quelques détails sur la façon dont l'écoulement du fluide est visualisé et évalué dans le voisinage de la bulle. La deuxième et dernière partie, la section 3.2, rassemble tous nos résultats. Là, la formation de motifs spécifiques de microstreaming est expliquée sur la base du contenu modal de la bulle. Dans ce but, une description quantifiée de la dynamique de la bulle est actuellement requise, alors qu'elle n'était auparavant étudiée que de manière plutôt qualitative. La corrélation de ces écoulements fluides avec l'activité de la bulle est expliquée pour cinq cas différents de configuration modale : un mode zonal uniquement, un mode sectoral uniquement, un mode tesséral uniquement, des modes zonaux et sectoraux combinés, et enfin, des modes tesséraux et sectoraux combinés. Dans le cas particulier et plus largement étudié des modes zonaux et sectoraux combinés, l'apparition préférentielle de motifs de microstreaming en forme de fleur et d'étoile est expliquée sur la base des amplitudes modales, de leur déphasage relatif et de la force de leur interaction. De temps en temps, cette analyse approfondie est appuyée par des exemples illustrés de notre méthode de calcul, tandis que les expressions analytiques sont données étape par étape dans les différentes sous-sections. De la même manière que précédemment, certaines visualisations occasionnelles d'une vue latérale de la bulle et de son streaming associé sont présentées séparément, en annexe A.2. Cela a permis de démontrer que les modes sectoriels génèrent un écoulement de type antifontaine avec une zone d'action significativement plus large que les modes zonaux et leur écoulement de type fontaine.

Enfin, le chapitre 4 rassemble les connaissances maintenant acquises sur une bulle fixée à une paroi animée par des modes non-sphériques pour évaluer les effets mécaniques induits sur une cellule biologique voisine. Pour expérimenter cela, deux modèles cellulaires décrits dans la section 4.1 sont sélectionnés : un ovocyte de souris et un mégacaryocyte humain. Alors qu'ils étaient tous les deux désignés comme de bons candidats pour notre étude, les ovocytes sont rapidement mis de côté en raison de la crise sanitaire inattendue, et donc de difficultés d'approvisionnement. En conséquence, l'étude est limitée par la suite aux mégacaryocytes. Néanmoins, quelques rares résultats sur les ovocytes sont présentés hors de ce chapitre, en annexe B. Après avoir exposé les bonnes pratiques concernant la préparation des mégacaryocytes vient la section 4.2 sur la méthodologie expérimentale, dans laquelle sont détaillées nos méthodes employées pour manipuler les cellules et quantifier leur réponse mécanique. De plus, un petit aparté propose une caractérisation du milieu de culture employé à la place de l'eau comme milieu d'expérimentation. Tout ceci étant à présent établi, la section 4.3 peut débuter. Commençant par une brève analyse des seuils d'instabilité de pression pour notre bulle désormais entourée de milieu de culture, arrivent alors les résultats sur l'interaction mécanique entre une cellule biologique et une micro-bulle. Tout d'abord, leur dynamique couplée est étudiée à l'échelle de temps acoustique au travers de l'action de poussée-traction de la bulle sur la cellule adjacente, l'accent étant mis sur les modes sectoraux. Dans le but de mesurer l'élasticité de la cellule, ce mouvement périodique est ensuite mis à profit pour favoriser la propagation des ondes de cisaillement au sein de la cellule. D'autre part, à l'échelle de temps fluidique, le mouvement de rotation de cellules en suspension piégées sur les points de stagnation de l'écoulement fluide induit par une bulle est étudié. Enfin, plusieurs tentatives d'internalisation de particules fluorescentes (iodiure de propidium) ont été entreprises, mais sans succès. Cependant, le mouvement de poussée-traction de la bulle sur la cellule a pu être clairement observé de façon qualitative, ainsi que la détection et l'identification de modes non-sphériques significatifs et stables. Pour conclure, la sonoporation cellulaire d'une cellule voisine adhérente induite par une microbulle oscillant non-sphériquement n'est pas immédiate. Impossible semble un peu impulsif comme conclusion, mais certainement très compromis avec la configuration expérimentale telle qu'elle est.

Contents

Introduction

> *There is no angry way to say "Bubble".*
>
> Someone, someday.

Bubbles are everywhere. They are just like cats: They exist in a multitude of sorts and sizes. Some are wild, some are chosen for specific characteristics. Some are expensive, some are obtained for free. Some are massive, some are tiny. Some are exotic, some are regular. Some are beautiful, some are of subjective beauty. Some bring joy and happiness, some are not always in the right place at the right time. However, in the end, they are all the same, they are cats and bubbles.

The genesis of a microbubble never comes alone. It results from a triggering event and may be facilitated by the presence in the fluid of an heterogeneity. From the very first moments of its existence, the bubble adopts a spherical shape, as in a natural and intuitive way, anyone would picture it. At least, this is what happens when the bubble is not influenced by some external disturbance. When this is the case, bubbles can be subject to buoyancy like in a glass of champagne, burst like a chewing gum bubble or collapse and severely damage machinery. Uncontrolled bubbles can be the source of important troubles. Engineers in hydrodynamics had figured that out when they observed how cavitation bubbles, generated by a transient pressure drop below the liquid's vapor pressure, could have destructive effects on pumps and propellers. Cavitation is in most cases an unwanted occurrence, but in some others it turns out that well-controlled bubbles can be very beneficial. In fact, there is one sequel this thesis focuses on: the sonoporation of biological cells induced by oscillating microbubbles for purposes of drugs or genes internalization. This is allowed by the wonderful characteristic of microbubbles to be very selective acoustic resonators. This makes them perfect transducers for remotely inducing mechanical waves within any fluid environment. In addition to this oscillatory motion of the surrounding fluid, a steady flow emerges from the nonlinear response of the fluid. These two different motions operate at different time scales, and yet are both held responsible for the generation of stresses on a nearby surface. Prior to placing a biological cell in front of an oscillating bubble, the logic would like us to study first these two phenomena in an exclusive manner.

We believe that the study at the microscopic scale of one single bubble and one single cell could improve the understanding at the macroscopic scale of the erratic and complex phenomenon in which hundred of thousands of microbubbles interact with as many biological cells. To this end, this thesis manuscript presents an experimental work on the physics of one single microbubble and its induced effects on a nearby cell. It is organized in four chapters.

The chapter 1 takes us on a journey into the scientific, medical and industrial worlds of bubbles. It establishes the context in which this thesis takes part by defining and discussing the concepts and the physics of nonspherical bubbles, microstreaming and sonoporation. These three terms respectively summarize the next three chapters, devoted to an extensive experimental study of the mechanical behavior of cells and microbubbles immersed in an acoustic field.

The chapter 2 is dedicated to the dynamics of a wall-attached microbubble. Its visualization from a top-view allowed to evidence the nondegeneracy, or spectral splitting, of its nonspherical shape modes, triggered above certain critical thresholds of acoustic pressure. Also, the coexistence, facilitated or not, between modes is discussed on the basis of their dynamics and geometrical features.

The chapter 3 focuses on the formation of fluid flows, also called streaming, induced by these nonspherical modes. It goes further in the description of the time-resolved bubble dynamics with a quantitative analysis of the modal amplitudes, so that the modal interaction truly responsible for the formation of streaming could be assessed. A large spectrum of varied streaming patterns is unveiled, and compared in terms of shapes, flow direction and velocity magnitude.

The chapter 4 relies on the precedent results on bubble dynamics and induced streaming to explain their possible interaction with a biological cell located in the bubble vicinity. With the view to investigate the effects of both the bubble pushing-pulling action and the formation of streaming-induced stresses, the study is twofold, taking place at the acoustic and the fluidic time scale.

Chapter 1

About bubbles

This introducing chapter aims at laying down the groundwork of this thesis, and motivating its ins and outs. Concepts of bubble, cavitation and sonoporation are stated, in addition to a comprehensive overview of their physics and their applications and interests. It begins in section 1.1 with the global scientific and medical context in which gas bubbles are involved. Afterwards, we will wander the grounds of what characterizes a stable oscillatory regime of microbubbles first in a condition of low acoustic pressure and purely spherical motion with section 1.2 and then in a condition of high acoustic pressure and nonspherical deformations of the bubble interface with section 1.3. It is completed by an extended comment on how the presence of a wall can alter the bubble acoustic response in terms of its modal content and displacement amplitude. This chapter ends with the description of the effects induced by the bubble oscillations on the surrounding environment. This includes the formation of fluid flows around the oscillating bubble with section 1.4 and the usage made out of it for a particular purpose of therapeutic application that consists in the permeabilization of biological cells for facilitating their uptake of drugs and genes with section 1.5.

1.1 Context of microbubble and cavitation

A microbubble, which is nothing else but some gas trapped in a volume of fluid, requires necessarily any triggering event or some kind of heterogeneity to exist. From the very first moments of its existence, the bubble is exposed to mechanical stresses at its liquid-gas interface due to an attractive force pulling the water molecules towards each other. The resulting inward force is exactly balanced by the outward-pushing pressure of the enclosed gas. As a consequence, it is constrained to minimize its interface area, forcing it to adopt a spherical shape. At least, this is how bubbles behave when they are at rest. In contrast, when they are animated by any event, a fluid flow, a change in the local fluid pressure or the activation of an acoustic source, things take a different turn. It is under these circumstances a bubble can unveil its most favorable, but also its most unwanted and terrible effects.

In an engineering context, the term cavitation originally refers to a complex and erratic phenomenon triggered by an important and fast pressure drop below the vaporization pressure of the liquid, and by which bubbles get nucleated in a liquid, progress in an erratic motion and then collapse. When described with such words, this does not bode well. As a matter of fact, the collapse of millions of microbubbles is comparable to so many violent detonations at the center of which the temperature can locally rise up to thousands of Kelvin degrees and the pressure reach colossal magnitudes. The random generation and the destructive effects of such bubbles are very likely one of the main issues in the design of industrial fluidic devices today. Hopefully, bubbles are not only undesirable occurrences. If controlled, their immense amount of thermal and mechanical energy can be employed in many positive ways.

1.1.1 Medical and industrial applications

Industrial purposes

The applications of bubbles in industry are not lacking. Some of the best known and documented concern their use for cleaning, degreasing and sterilizing pharmaceutical, biotechnological and medical materials, as well as their use in the manufacturing process of polymer foams [Dollet et al., 2019]. In the former, it involves clouds of acoustically-driven bubbles and their influence on and with a wall of variable stiffness and elasticity. For understanding the involved mechanisms in such closed industrial devices, every configurations are explored: from the single bubble system, attached to a wall [Doinikov et al., 2011], in close proximity [Garbin et al., 2007] or confined between walls [Mekki-Berrada et al., 2016], to the arrangements of several bubbles and their altered behavior in presence of so many others; resonance frequency shift [Prosperetti, 1988] and anisotropy of the amplitude response [Maeda and Colonius, 2019]. However, because the surface cleaning with ultrasound also comes from the high stresses generation potential of jetting bubbles, further comprehension is also brought by studying the inertial dynamics of a single bubble, i.e. the unstable and non-periodic behavior, which can be mimicked by its laser pulse induced collapse [Reuter and Mettin, 2016]. Finally, special attention is also given through research aiming at reducing the environmental impact and the cost of such techniques [Miyamoto et al., 2007, Dollet et al., 2019].

Medical imaging

Thanks to their large acoustic impedance mismatch with the surrounding biological tissues, microbubbles are great scatterers of acoustic energy. For that reason, they were employed for purposes of medical imaging since the early stages of their taming for the seeking to new scientific interests and perspectives in the 1980's. Microbubbles could help to return more back-scattered energy from the venous network than in normal condition without their injection, and in this way highlight blood circulation dysfunctions, blood clots and stenosis, or even cardiac arrhythmias and myocardial ischemias. When created with a specific gas, microbubbles injected in the venous network are able to persist for a given time in order to reach a desired location of interest before their dissolution. For instance, for a same size of 2 µm, bubbles made of octafluoropropane and decafluorobutane can last 400 ms and 4 s, respectively, for only 25 ms for air bubbles [Chomas et al., 2001]. In addition, when the gas is enclosed in a specific coating consisting of proteins, lipids, sugars or polymers, their lifetime can stretch to several minutes. Arrived at destination, the microbubbles are finally activated by ultrasound in a non-invasive way. A second advantage of these manufactured bubbles is the possibility of adjusting their acoustic response by modifying the shell composition and thickness or by adapting the enclosed gas, its density and compressibility. Depending on the biological region to be explored, one may wish to improve their spectral response to lower frequencies that have a better dissipationless penetration through the tissues or on the contrary increase their response to higher frequencies for having the possibility of using them with a high frequency transducer characterized by a better spatial resolution. Moreover, some other techniques rely of their tunable nonlinear behavior to differentiate their back-scattered energy from what is emitted by the nearby tissues [Postema and Schmitz, 2006, Segers et al., 2015].

Medical therapies

As said so well by Postema and Bouakaz [2018] three years ago in the editorial of the conference on acoustic bubbles in therapy held in Tours, *"although the use of microbubbles has become common in ultrasound diagnostics, microbubbles are not that often seen in therapeutic applications."* This assertion stems from the particularly complex and difficult-to-predict nature of acoustically excited bubbles. Yet, the mechanical and thermal energy potential of such bubbles make it a highly coveted technique, especially since their use is minimally invasive, inexpensive and non-irradiating for organic tissues. Nowadays, microbubbles are at the central focus of many still preclinical studies, while the effective clinical applications of bubble-based therapeutic techniques are restricted to the breaking of kidney stones by associated shock-waves and cavitation, and to the treatment of cataract on the same principle of destruction of the opacified crystalline lens. Nevertheless, preclinical studies show promising advancements in the use of acoustic microbubbles for the treatment of varicose veins and for the elimination of blood clots. Very recently, the remote action of acoustically driven drug-loaded microbubbles was showing successful results of drug release *in-vivo* through the blood-brain barrier (BBB) without compromising its safety [Ozdas et al., 2020]. This latter application consists in applying mechanical stresses on biological cells, sufficiently to temporarily alter the permeability of the cells wall, but without excess to avoid their permanent lysis. The mechanical stimulation of cells can be locally and remotely done in various ways by means of microbubbles, while the real challenge in that situation is the effective control and mediation of the involved technique for enhancing the therapeutic effects (drug or gene uptake) and minimizing the adverse and unwanted fallout (cell lysis).

1.1.2 Methods for bubble nucleation

Thermal vaporization

Literature about bubbles makes a distinction between bubbles made of a permanent gas and bubbles nucleated from a heating process through the formation of vapor. Besides major differences in terms of their oscillatory stability [Feng and Leal, 1997], because the diffusivity of gases is about hundred times smaller than the thermal diffusivity, a vapor bubble differentiates from a gas bubble by its extreme sensitiveness to changes in pressure and temperature in its near environment, which could for instance generate its rapid condensation and extinction [Prosperetti, 2017]. In the range of experimental methods for nucleating bubbles that are soliciting a thermal increase with the generation in the liquid of a laser pulse or an electrical spark discharge, the maintenance of a bubble only consisting of vapor could only be achieved by maintaining a local high temperature. In the absence of such a means of bubble maintenance, the bubble would rapidly collapse. This fast motion is widely investigated with laser- and spark-induced transient bubbles through the formation on a nearby wall of micro-jets [Tagawa and Peters, 2018, Rapet et al., 2019, Fong et al., 2009] and shock waves [Tagawa et al., 2016].

In studies investigating stable oscillations of bubbles nucleated by a local thermal increase, bubbles consist of vapor exclusively at the very first moments of their existence. Immediately afterwards, their persistence and growth result from the transfer of gas dissolved in the surrounding liquid by the phenomenon of rectified diffusion under the action of an oscillating pressure field, hence commonly referred as vapor-gas bubbles. Due to the rapid drop in temperature, the vapor has very likely condensated and only the gas remains. Laser pulse and spark discharge based methods for bubble nucleation present great advantages, respectively, the absence of induced flow disturbance, and the simplicity and low cost of the setup [Fong et al., 2009]. In addition, the bubble nucleation can be provoked in a closed or hard-to-reach space. Once the mechanism is set up, these methods have good repeatability in terms of localization of the bubble formation.

Prefabricated bubbles

Even if already mentioned previously in section 1.1.1, it is worth providing further explanation about the pros and cons of the use of prefabricated bubbles, also referred as ultrasound contrast agents (UCA). They are suitable in both *in-vivo* and *in-vitro* environments. The reason for that comes from the possibility for prefabricated bubbles to be designed with specific inner gases and coatings that allow to tune and increase their persistence. This makes them very convenient in medical applications where the choice of the frequency and the distance of the path to be covered by the bubbles depend on the area to be investigated, but also in experimental research with their possibility, once created, to be easily transported or stored for further use. Their manufacturing performed in microfluidic devices allows a very accurate control of their size at a production rate of up to one million bubbles per second [van Elburg et al., 2021]. According to the needs, it is possible to obtain bubble populations with an accurately regulated polydispersion or monodispersion, which can enhance their remote acoustic control. However, when there is no home-made facility for their production, their acquisition can be relatively expensive.

Acoustics

Nucleating bubbles with acoustics results from a pressure decrease below the vapor pressure threshold. The erratic and possibly violent behavior of this process was already mentioned in section 1.1. More exactly, the random and unpredictable behavior in terms of localization of cavitation nuclei and bubble size dispersion makes this method for bubble nucleation not really suitable whether it is wanted to create one single bubble with the view of studying its dynamics. The same reasons make the use of cavitation within *in-vivo* environments an unsafe and still too little understood tool, today.

It is worth noting that in literature, the term acoustic cavitation bubbles is also often attributed to ultrasound-driven bubbles, no matter how they were created, whether they were prefabricated, nucleated from a thermal process or a pressure drop, for instance.

Electrolysis

The electrolysis is defined as the breakdown or decomposition of something by use of electricity. In an industrial context, it is employed for the extraction of metals from ores, or in the production of chemicals from ionic compound. It consists in immersing two electrodes in a solution and applying a direct electric current. When performed in pure water with added $NaCl$ as an electrolyte, it occurs the overall reaction

$$\underbrace{2NaCl + 2H_2O}_{\text{reactants}} \longrightarrow \underbrace{Cl_2 + H_2 + 2NaOH}_{\text{products}} \tag{1.1}$$

Chlorine (Cl_2), that quickly dissolves in water, is generated at the positively charged anode where it results an oxidation reaction. Dihydrogen gas (H_2) is generated at the negatively charged cathode where it results a reduction reaction. The circuit is completed when the ions Na^+ and OH^- react to constitute sodium hydroxide ($NaOH$) in the form of a new electrolyte. Unlike the bubble nucleation by laser pulse or spark discharge, the bubble nucleation by electrolysis requires an access to the interior of the tank for the wires to be immersed and manipulated. On the other hand, this is a lot less expensive method, given that only a signal generator, a metal wire and table salt are needed. With some skills in handling the cathode, the tethering of a nucleated dihydrogen bubble to a substrate can be easily performed to arrange it in an experimental configuration attached to a wall, for instance. All things considered, this nucleation method by electrolysis will be preferred for the experimental purpose of this thesis work.

1.2 Spherical bubble dynamics

Provided its size is small enough related to the acoustic wavelength ($R_0 << \lambda$), a bubble immersed in an acoustic field experiences an homogeneous pressure all along its interface. Under the action of this pressure fluctuation, the bubble oscillates with a spherical shape, while the pressure within the bubble varies inversely with its size variations.

Extended Rayleigh-Plesset model

The dynamics of an acoustically forced bubble was mathematically described for the first time by considering an incompressible inviscid liquid under adiabatic conditions with the following second-order differential equation known as Rayleigh-Plesset equation

$$\rho \left[R\ddot{R} + \frac{3}{2}\dot{R}^2 \right] = p_i - p_e(t), \tag{1.2}$$

where R, $\dot{R}$ and $\ddot{R}$ are respectively the instant radius of the spherical bubble and its first and second order derivatives with respect to time. The constant ρ is the liquid density, p_i the bubble's supposed homogeneous internal pressure, $p_e(t) = p_\infty + p_{ac}(t)$ the external pressure that includes the static pressure or far-field pressure p_∞ and the driving acoustic pressure $p_{ac}(t)$. Equation (1.2) does not consider the bubble surface tension and the viscosity of the liquid. When assuming a bubble with very small radius, these last quantities that are inversely proportional with the bubble radius are no longer negligible and must be considered. As a consequence, additional terms complete the expressions of internal and external pressures $p_i(t)$ and $p_e(t)$ of equation (1.2), so that it takes the form

$$\underbrace{\rho\left[R\ddot{R}+\frac{3}{2}\dot{R}^2\right]}_{\text{inertial terms}} = \underbrace{p_v(T)+p_{g0}\left(\frac{R_0}{R}\right)^{3\gamma}}_{\text{internal pressure } p_i(t)} - \underbrace{\left[p_\infty + p_{ac}(t) + \frac{2\sigma}{R} + 4\mu\frac{\dot{R}}{R}\right]}_{\text{external pressure } p_e(t)}, \tag{1.3}$$

where σ is a surface tension coefficient expressed in $\mathrm{N}\cdot\mathrm{m}^{-1}$ and $\mu = \nu\rho$ is the liquid dynamic viscosity expressed in $\mathrm{Pa}\cdot\mathrm{s}$, with ν the kinematic viscosity. The quantity $p_v(T)$ refers to the vaporization pressure, which is a function of the temperature T. It translates the thermal agitation of liquid and thus the tendency for liquid particles to change from a liquid to a gaseous state. As the temperature rises, so does the vaporization pressure and the internal pressure of the bubble. $p_{g0} = 2\frac{\sigma}{R_0} + p_\infty - p_v(T)$ is the instantaneous partial pressure p_g of the gas inside the bubble but here assumed to be constant with time, the additional subscript 0 referring to an initial condition. Finally, $\gamma = 1.4$ is the ratio of the gas heat capacities, as no thermal or mass transfer between the inside and the outside of the bubble are assumed. Equation (1.3) is also referred as RPNNP equation in commemoration to its contributors, Rayleigh [1917], Plesset [1949], Noltingk and Neppiras [1950], and Poritsky [1951]. Even though a qualitative approach of equation (1.3) was obtained by Ma and Wang [1962] who analytically investigated the bubble radial velocity $\dot{R}$ as a function of the interface displacement R, a numerical solver is preferred whether the objective is to obtain a quantitative solution for this differential equation.

Linearization of Rayleigh-Plesset equation

By considering a small displacement $r(t)$ of the bubble interface $R(t) = R_0 + r(t)$ with regards to the bubble radius at rest R_0, also named bubble equilibrium radius, such as $r(t) \ll R_0$, equation (1.3) can be linearized. By doing so, it brings up the equation of a forced and damped harmonic oscillator

$$\ddot{r}(t) + \delta\dot{r}(t) + \omega_b^2 r(t) = \frac{-p_{ac}(t)}{\rho R_0}, \tag{1.4}$$

that is characterized by a resonant pulsation $\omega_b^2 = \frac{3\gamma p_\infty}{\rho R_0^2} + \frac{6\sigma\gamma}{\rho R_0^3} - \frac{2\sigma}{\rho R_0^3}$ and a damping term $\delta = \frac{4\mu}{\rho R_0^2}$. When neglecting the second and third terms in R_0^{-3}, the expression of the resonant pulsation simplifies. The numerical application in water with $\gamma = 1.4$, $p_\infty = 10^5$pascal and $\rho = 10^3\mathrm{kg}\cdot\mathrm{m}^{-3}$ leads to the expression

$$R_0 f_b \simeq 3.26\ \mathrm{m}\cdot\mathrm{s}^{-1}\ . \tag{1.5}$$

This qualitative estimation of the natural frequency of a bubble f_b associated to its radius at rest R_0 through the linear expression of equation (1.5) is called Minnaert's frequency, in tribute to its initiator [Minnaert, 1933].

Determination of the acoustic pressure from the bubble radial displacement

When the acoustic pressure close to an oscillating bubble cannot be measured with an hydrophone at the risk of altering the bubble behavior and when the bubble location in the acoustic field is not controlled, an other way for obtaining the acoustic pressure applied on the bubble has to be found. From the observation of the bubble interface small fluctuations, the acoustic pressure can be deduced thanks to equation (1.4). By assumption of a constant acoustic pressure and a spherical oscillation of the form $r(t) = A_r \cos(\omega_0 t + \psi) \ll R_0$, where $\omega_0 = 2\pi f_0$ is the driving angular frequency and ψ the phase shift, the acoustic pressure P_a writes

$$P_a = \beta \rho R_0^2 \sqrt{(\omega_b^2 - \omega_0^2)^2 + \delta^2 \omega_0^2}, \tag{1.6}$$

with

$$\beta = \sqrt{C_1^2 + C_2^2}, \quad C_1 = \frac{2}{T} \int_0^T \frac{r(t)}{R_0} \cos(\omega_0 t) dt, \quad C_2 = \frac{2}{T} \int_0^T \frac{r(t)}{R_0} \sin(\omega_0 t) dt,$$

and $T = 1/f_0$ is the acoustic period. The experimental knowledge of the bubble instantaneous radius $r(t)$ allows to numerically determine C_1 and C_2. In chapter 2, we will see that the experimental method consists in applying an acoustic field modulated in amplitude. Besides the interest of studying the dynamics and stability of a bubble at different acoustic pressure, the modulation of the acoustic field allows to calculate the acoustic pressure at low values and then to extrapolate it linearly along the whole modulation ramp.

Bubble spherical stability

The question of the stability of a bubble interface is a major concern in hydrodynamics where the collapse of bubbles can generate micro-jets and shock waves with highly destructive potentials. Interface instabilities of an acoustically forced bubble arise from its radial interface motion and can result from two different mechanisms: the Rayleigh-Taylor instability and the Faraday instability [Feng and Leal, 1997]. They especially differentiate by their temporal scale of setting up. A Rayleigh-Taylor instability is the consequence of a rapid radial acceleration of the bubble interface. Its growth time can be estimated from $\Delta\tau = \left(\frac{\sigma}{\rho a_s^3}\right)^{(1/4)}$, where σ and ρ are the liquid surface tension and density, and a_s is the acceleration of the radial motion [Avila and Ohl, 2016]. For a bubble driven at 30.5 kHz animated by a 5 µm radial amplitude displacement, a Rayleigh-Taylor instability would develop in a time delay of about 10 µs, provided the interface acceleration a_s is maximal and constant during this time delay. However, because an important acceleration only happens for a small portion of a bubble oscillatory cycle, Rayleigh-Taylor instabilities do not apply to oscillating bubbles in weakly viscous fluids [Feng and Leal, 1997]. On the other hand, the Faraday instability results from the accumulation of interface instabilities over several bubbles oscillations above a critical radial amplitude. It is therefore a relatively much slower mechanism described as parametric because it is forced by the amplitude of the periodic radial motion. This type of instability is at the origin of the break of spherical bubble stability as we experienced it in the present work and which resulted in nonspherical deformations of the bubble interface [Guédra et al., 2017].

The wall effect

In the absence of any particular triggering event, bubbles naturally nucleate where they meet surface irregularities or heterogeneities in a fluid. The study of the mechanical behavior of a bubble attached to a substrate is thus of great interest to answer its physics in closed environments, as in pumps and industrial cleaning devices, or even in biological tissues. The parametric instability discussed in previous section arises from the nonlinear spherical behavior of the bubble interface, accumulated over several oscillations beyond a critical magnitude of acoustic pressure [Guédra et al., 2017, Feng and Leal, 1997]. Because there exists no theory predicting the spherical instability of an oscillating wall-attached bubble, a comparative example is given in figure 1.1, in order to unveil some evidence of dissimilarity between the nonlinear behavior (and hence the stability) of the spherical oscillation of free bubbles and attached bubbles.

Under the action of a 30.5 kHz low-pressure periodic forcing (about 2 kPa), a microbubble undergoes a low amplitude sinusoidal displacement (about 0.5 µm) of its spherical interface around its value at rest $R_0 = 64.6\,\mu\text{m}$, as depicted in figure 1.1a. The experimental data correspond to the case of a bubble attached to a wall, while the joined numerical simulation corresponds to a bubble of same equilibrium radius, but free of any constraints. Their comparison shows that the tethering of the bubble does not seem to alter the spherical dynamics at low acoustic pressure.

Under the action of a high-pressure periodic forcing (about 30 kPa), the same microbubble attached to the wall undergoes a high amplitude displacement (about 6 µm) of its constant spherical interface, as depicted in figure 1.1b. This spherical oscillation diverges barely from linearity as it does not exhibit a monochromatic aspect anymore. In contrast, the numerical simulation of a free bubble of same radius undergoes a strong nonlinear behavior. The theoretical model for free bubble does not match anymore the dynamics of the experimental wall-attached bubble.

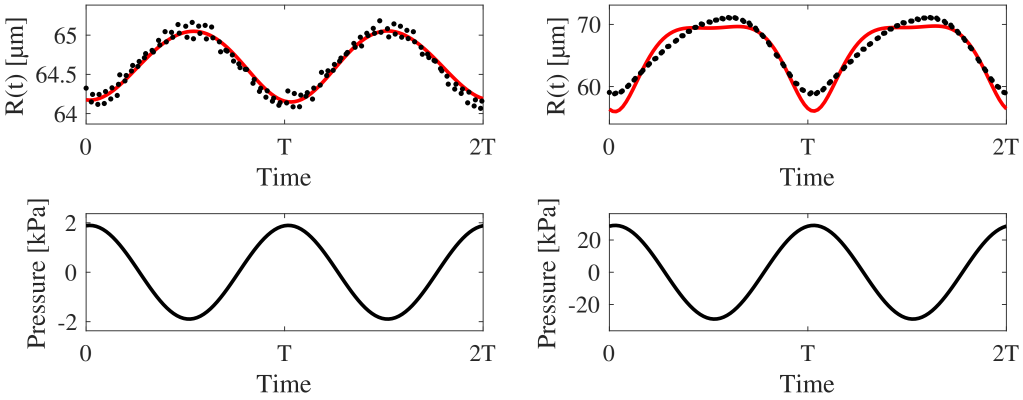

Figure 1.1: Example of radial oscillations of a microbubble of equilibrium radius $R_0 = 64.6\,\mu\text{m}$ driven at 30.5 kHz with an acoustic pressure of about 2 kPa (left) and 30 kPa (right). The comparison between the cases of an experimental wall-attached bubble (black dots) and a theoretical free bubble (red curves) highlights the different nonlinear behavior at high acoustic pressure. The information is structured as follows. Top: time-resolved dynamics of the experimental bubble radius (black dots) and the numerical bubble radius implemented with an extended Rayleigh-Plesset model (red solid line). Bottom: acoustic pressure signal obtained from the experimental bubble and the method described in section 1.2, and then introduced as an input parameter in the numerical simulation.

It is expected that the truncation of the bubble spherical shape due to the tethering and thus the break of the bubble symmetry could facilitate the triggering of bubble interface instabilities. In other words, the tethered bubble does not necessitate to undergo a strong nonlinear spherical oscillation before interface instabilities arise, unlike the free (not-truncated) bubble, for which the nonlinear behavior of the spherical oscillation can reach stronger magnitudes before any instabilities get triggered. This might explain the difference displayed in figure 1.1b between the spherical oscillations of the theoretical free bubble and the experimental tethered bubble at an acoustic pressure close to the threshold of parametric instability.

Theoretically, the presence of a nearby wall is usually modeled as a two-bubbles system by considering an additional virtual bubble as a mirror image [Doinikov et al., 2009, Vos et al., 2011]. In this configuration, an arbitrary elasticity for the wall can be simulated by introducing a phase shift in the dynamics of the bubble mirror image with respect to the original one. In a condition of attached bubble, an increased difficulty arises in the mathematical description of the contact line dynamics and its reciprocal effects on the bubble dynamics. For this reason, theoretical works on wall-attached bubbles are scarce. We can still mention a study of Maksimov [2005] who demonstrates a significant modification of the radial (breathing) mode pulsation due to the volume truncation of a tethered bubble, as a function of the equilibrium contact angle. For a vertically vibrating plate, the contact line dynamics can also be estimated through the condition of Hocking [1987] who suggests a solution accounting for the contact angle hysteresis and the energy dissipation due to the moving contact line. Experimentally, an upward shift in resonance frequency and a decrease in the radial oscillation have also been shown for adherent bubbles. This emanates from the stiffening of the system [Lum et al., 2020].

1.3 Nonspherical bubble dynamics

1.3.1 Nonspherical modes

Spherical-coordinate harmonics

When excited at sufficiently high acoustic pressure, a bubble may exhibit nonspherical modes. These nonspherical deformations of its interface are traditionally described using the spherical harmonics. Mathematically, a spherical harmonic is a harmonic function, namely a function, let us call it h, that is the solution to the Laplace's equation in the spherical system of coordinates (r,θ,ϕ).

$$\frac{1}{r^2}\frac{\partial}{\partial r}\left(r^2\frac{\partial h}{\partial r}\right)+\frac{1}{r^2\sin\theta}\frac{\partial}{\partial\theta}\left(\sin\theta\frac{\partial h}{\partial\theta}\right)+\frac{1}{r^2\sin^2\theta}\frac{\partial^2 h}{\partial\phi^2}=0. \tag{1.7}$$

The spherical harmonics are the equivalent of the Fourier series which allow the description of any harmonic function in a single sum of cosines and sines, but here applied to the case of functions defined on a sphere of unit radius. Because they are normalized to one, these functions form an orthonormal basis and are traditionally introduced as

$$Y_n^m(\theta,\phi)=(-1)^m f_{nm}P_{nm}(\cos\theta)e^{im\phi}, \tag{1.8}$$

where n and m are two integers closely connected by $-n \leq m \leq n$ and respectively named the degree and the order of the spherical harmonic. P_{nm} is the associated Legendre polynomial of degree n and order m, and $f_{nm}=\left(\frac{2n+1}{4\pi}\frac{(n-|m|)!}{(n+|m|)!}\right)^{1/2}$ is the normalization coefficient. The orthonormality relation between two spherical harmonics Y_n^m and $Y_{n'}^{m'}$ writes

$$\int_{\theta=0}^{\pi}\int_{\phi=0}^{2\pi} Y_n^m\, Y_{n'}^{m'*}\, d\Omega=\delta_{nn'}\,\delta_{mm'}, \tag{1.9}$$

where $Y_n^{m*}(\theta,\phi)=(-1)^m Y_n^{-m}(\theta,\phi)$ is the complex conjugate of $Y_n^m(\theta,\phi)$ and $d\Omega=\sin\theta\; d\theta\; d\phi$ is the solid angle. Spherical harmonics are functions commonly employed in physics, especially in quantum mechanics, for describing the motion and the wave-like behavior of gravitating electrons of atoms and in geophysics for representing the surface of the terrestrial globe or its magnetic field. The phase factor $(-1)^m$ in equation (1.8) is usually employed in quantum mechanics for simplifying some operations. In what concerns us, in acoustics and vibration systems this phase factor is not included in the definition of spherical harmonics, just as the index m will be considered as having always a positive value. This simplification is allowed when considering the harmonics Y_n^m and Y_n^{-m} equivalent, up to one rotation in azimuth (following the variable ϕ). Its relation with n is thus simplified as $0 \leq m \leq n$ in the following. Spherical harmonics cancel on m nodal meridians ($2m$ if a meridian is defined as joining the two poles, instead of going all around the sphere) and $n - m$ nodal parallels, for a total of n nodal lines, as illustrated in figure 1.2. Following the relation between the order m and the degree n, and thus the number of nodal meridians and parallels, spherical harmonics take different names: zonal when $m = 0 < n$, tesseral when $n > m > 0$ and sectoral when $n = m > 0$. It seems important to clarify at this stage that the zonal modes are ϕ-independent as they are functions axisymmetric around the axis z ($\theta = 0$). $Y_n^m(\theta, \phi)$ and $Y_{nm}(\theta, \phi)$ are two different notations employed in literature that refer to the same spherical harmonic of degree n and order m. The notation $Y_{nm}(\theta, \phi)$ is the one that will be preferred throughout this manuscript.

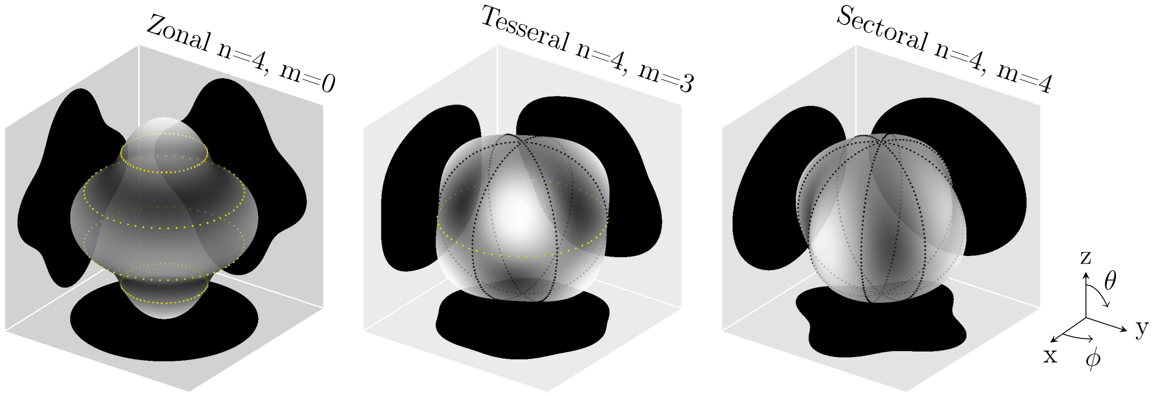

Figure 1.2: Exemplary cases of implemented spherical harmonics and their projections in the (x,y), (x,z) and (y,z) planes for a degree $n = 4$: a zonal harmonic ($m = 0 < n$), a tesseral harmonic ($0 < m = 3 < n$) and a sectoral harmonic ($m = 4 = n$). Their respective $n - m$ nodal parallels (in yellow) and m nodal meridians (in black) are drawn on each spherical harmonic. The system of coordinates is given in the lower right corner of the figure.

Bubble shape modes

The most common approach for investigating the shape perturbation of an initially spherical bubble is to describe its interface with the equation

$$S(\theta, \phi, t) = r(\theta, \phi, t) - R_0 - \sum_{n,m} a_{nm}(t) Y_{nm}(\theta, \phi) = 0, \tag{1.10}$$

where $a_{nm}(t)$ are the time-varying amplitudes of the bubble modes (including the purely radial one for $n = m = 0$). The set of spherical harmonics Y_{nm} applied to a numerical bubble of equilibrium radius $R_0 = 90\,\mu\mathrm{m}$ can be visualized from a top-view perspective in figure 1.3. The $\cos(m\phi)$ azimuthal shape of sectoral modes and the circular azimuthal shape of zonal modes are obvious, while tesseral modes exhibit more complex shapes with nodal lines in both elevation and azimuth, barely discernible from this top-view.

Considering an incompressible, inviscid, unbounded fluid, Lamb [1916] derived the spectrum of natural angular frequencies for these nonspherical shape modes

$$\omega_n^2 = (n-1)(n+1)(n+2)\sigma/\rho R_0^3, \tag{1.11}$$

where σ is the surface tension and ρ is the density of the liquid. A further analysis of the nonspherical oscillations has been performed by Plesset [1954] who derived the equa-

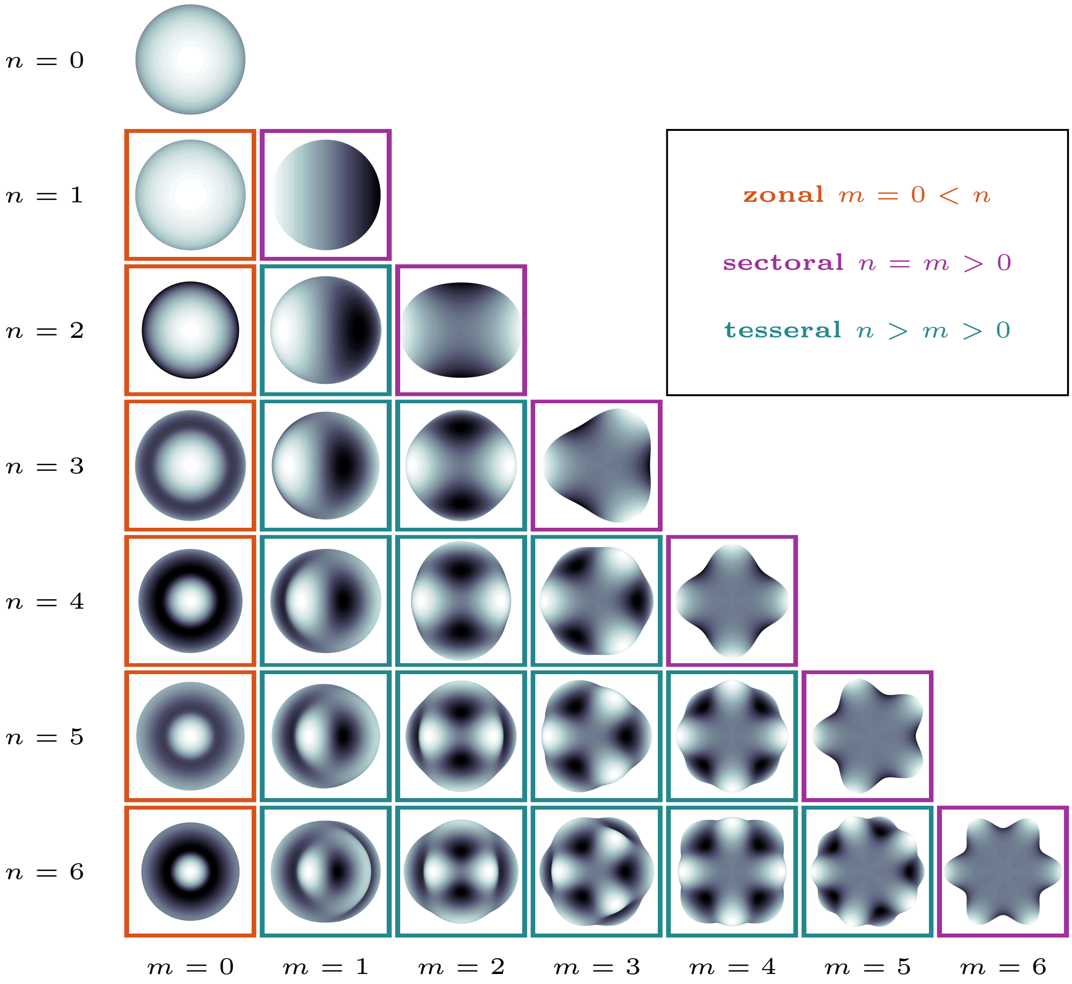

Figure 1.3: Overview of the bubble nonspherical modes ($R_0 = 90\,\mu\mathrm{m}$ and $a_{nm} = 30\,\mu\mathrm{m}$) for degrees up to $n = 6$, visualized from a top-view perspective.

tions of shape oscillations for small amplitudes of deformations $|a_{nm}(t)/R_0| \ll 1, n \neq 0$. In this approximation the equations for both spherical and nonspherical oscillations are uncoupled. The former is the Rayleigh-Plesset equation ruling the evolution of the radial oscillation, while the latter can be reduced to the Mathieu equation describing the parametric excitation of shape modes [Benjamin, 1958]. An important feature of the equations ruling the nonspherical oscillations is that they do not contain the index m. This means that, for a given spherical harmonic of degree n, all associated order-m functions are described by the same expression given by equation (1.11) and would have thus the same resonance frequency, which is referred in literature as degeneracy of spherical harmonics. This feature will be further discussed in the next section.

1.3.2 Parametric instability thresholds

Parametric instability thresholds of a free bubble

As introduced in section 1.2, these shape modes are generated through the process of parametric instability when the bubble radial oscillation is driven above some pressure threshold [Brenner et al., 1995, Feng and Leal, 1997, Shaw, 2017]. From a mathematical point of view, instabilities of bubble surface are commonly approached by assuming small amplitudes of nonspherical deformations. By conducting a perturbation analysis, Francescutto and Nabergoj [1978] obtained the pressure thresholds for the nonspherical oscillations, that are also independent of the index m of the spherical harmonics. From this analysis, for a given value n, the set of degree-n spherical harmonic modes for different orders m appears as degenerate modes. The mathematical analysis of an initially spherical bubble in an unbounded fluid is therefore commonly reduced to axisymmetric deformations invariant to the coordinate ϕ, for which spherical harmonics are described by Legendre polynomials (called zonal harmonics). The axisymmetry property is commonly retained in theoretical works as simplifying mathematical derivations. It is worth specifying at this stage that some experiments based on axisymmetric external forcing [Versluis et al., 2010], stereoscopic optical set-up [Guédra et al., 2017] or coalescence-induced shape mode triggering [Cleve et al., 2018] attest the validity of this assumption.

The threshold of this parametric instability depends on many factors, on the equilibrium bubble radius, the driving frequency and the degree of an arbitrary shape mode. The degree-n free bubble instability threshold P_{th}^n can be obtained from asymptotic approximation of the set of equations ruling the oscillations of axisymmetric deformations [Francescutto and Nabergoj, 1978, Nabergoj and Francescutto, 1979], and is expressed as:

$$P_{th}^n = \rho R_0^2 \, C_n \sqrt{(\omega_B^2 - \omega_0^2)^2 + \omega_0^2 \delta^2}, \tag{1.12}$$

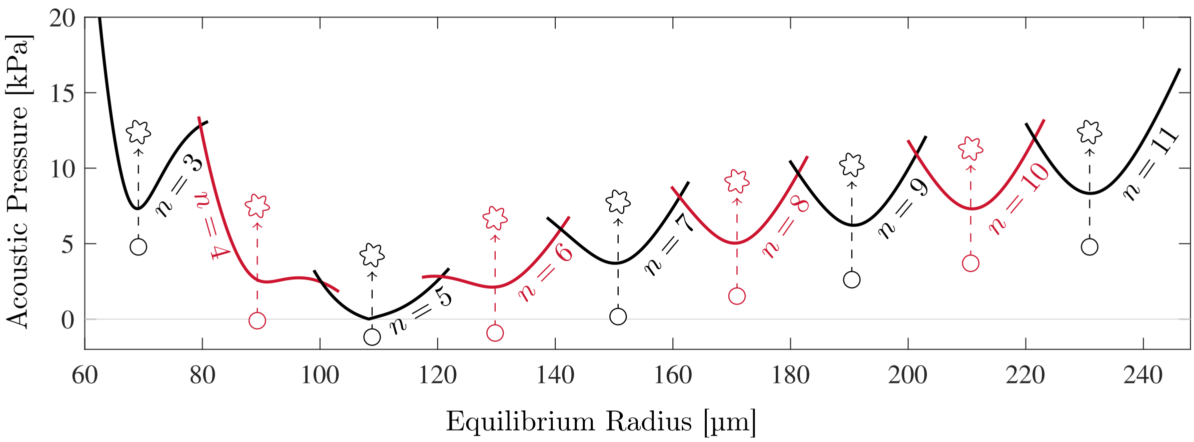

Figure 1.4: Theoretical pressure instability curves derived by Francescutto and Nabergoj [1978] for the case of a free bubble subject to axisymmetric shape modes Y_{n0}. The instability curves are drawn for modal degrees going from $n = 3$ to $n = 11$.

where

$$C_n = \sqrt{\frac{(a-1)^2 + 4p}{\left[-\frac{3}{2}a + 2p + 2\left(n + \frac{1}{2}\right)\right]^2 + q^2}},$$

$$a = \frac{4(n-1)(n+1)(n+2)\sigma}{\rho\omega_0^2 R_0^3}, \quad p = \left[\frac{2(n+2)(2n+1)\mu}{\rho\omega_0 R_0^2}\right]^2, \quad q = \frac{6(n+2)\mu}{\rho\omega_0 R_0^2},$$

and μ is the viscosity of the medium, ω_0 is the driving pulsation, ω_B is the resonance frequency of the bubble radial mode, $\delta = \frac{4\mu}{\rho R_0^2}$ is the damping constant applied by the medium on the bubble and n is the modal degree. These bubble instability thresholds have been calculated for degrees $n = 3$ to $n = 11$ for a bubble sizing in the range [60 250] µm. The result is shown in figure 1.4, where only the first parametric resonances are drawn. In practice, other secondary resonances can appear among these areas of instability. Lastly, it should be noted that the triggering thresholds are minimal when the bubble equilibrium radius R_0 is close to the resonance of the volumetric mode (Minnaert's resonance). With our experimental parameters, it is the instability curve of the first parametric resonance of the modal degree $n = 5$ that is concerned by this situation.

More information on the thresholds of these parametric instabilities investigated from a different perspective, as a function of the bubble radial amplitude displacement, can be found in the exhaustive review of Feng and Leal [1997] about the nonlinear dynamics of a gas bubble.

Parametric instability thresholds of a constrained bubble

Before discussing about how bubble shape modes are altered in presence of a wall, it should be noted that besides the study of the nonspherical dynamics of a bubble, another field of fluid mechanics studies in a similar way the dynamics of liquid drops. Indeed, they are governed by the same physics of surface tension which especially explain their tethering to a surface and their response to a high amplitude forcing with similar nonspherical shape deformations. Therefore, throughout this thesis manuscript, recurring analogies are made with the behavior of an attached drop, also referred as sessile drop or droplet, in order to support our analysis of an attached bubble. For the sake of simplicity and coherence, it has been preferred to directly integrate these comparisons into the discussions on the bubble dynamics rather than devote an exclusive section to these drop analogies. When this will happen, it will be explicitly stipulated in the text.

While microbubbles are commonly theoretically investigated as being immersed in an infinite liquid, constraints on bubble dynamics usually appear experimentally through the poking to neighboring cells [van Wamel et al., 2006], when being attached to a substrate in microfluidic applications [Vos et al., 2011, Prabowo and Ohl, 2011, Marmottant et al., 2006, Abramova et al., 2018], confined between walls [Mekki-Berrada et al., 2016] or restrained nearby a wall [Garbin et al., 2007, Dollet et al., 2008, Xi et al., 2014]. These experimental works teach us that the temporal dynamics of a constrained bubble significantly differ from the theory of free bubbles. In the case of a wall-attached bubble, if the dynamic feature of the contact line motion is taken into account [Shklyaev and Straube, 2008], linear coupling between shape and volume oscillations has been evidenced for hemispherical bubbles. In this particular case, it is theoretically demonstrated that the only shape modes that may interact with the breathing oscillation are the axisymmetric ones (arbitrary n, $m = 0$).

As explained in previous section 1.3.1, when deriving the equation of motion of bubble surface oscillation at the first order of the ratio between the modal displacement amplitudes and the bubble radius at rest $\epsilon_n = a_n/R_0$, it appears that asymmetric modes m of a same degree n are degenerate. The associated Lamb spectrum describing the instability regions of any surface mode is therefore limited to the spectrum of the zonal, axisymmetric modes. This degenerate behavior of the set of spherical harmonics comes from an assumption commonly operated in theoretical works. This simplification has been refuted by recent works where the splitting of the natural frequencies of the whole set of asymmetric oscillations has been evidenced, experimentally for a substrate-attached bubble [Fauconnier et al., 2020] and for a sessile drop [Chang et al., 2013], and theoretically for a bubble oscillating near a wall [Maksimov, 2020].

Still for wall-attached bubbles, the shape mode characterization is either performed through a Fourier mode decomposition of the bubble interface [Prabowo and Ohl, 2011] (and hence restricted to axisymmetric deformations) or only qualitatively described [Birkin et al., 2001, Abramova et al., 2018]. In the case of vibrating sessile drops, image post-processing of profiles from a top-view allows determining the modal decomposition on the basis of spherical harmonics [Courty et al., 2006, Chang et al., 2013]. In the above-mentioned studies, the investigations are restricted to the shape mode classification, the temporal dynamics of the non-axisymmetric oscillations being usually disregarded. The mechanism underlying which shape mode is chosen to grow to a steady-state, and selected out, is not revealed so far. Such mode selection, and the establishment of a final bubble shape, may be deduced from the symmetry of the studied geometry [Dollet et al., 2008] or preferential directions of the ultrasound wave [Versluis et al., 2010]. Theoretically, a three-wave resonant interaction between the Faraday ripples on the bubble surface has been proposed to describe the selection of an established standing-wave pattern [Maksimov and Leighton, 2012]. Experimentally, the preferential manifestation of sectoral modes has recently been described [Abramova et al., 2018].

1.4 An overview on microstreaming

When an ultrasound-driven microbubble oscillates nonspherically in a volume of fluid, it occurs, at the acoustic time scale, an oscillation of the fluid particles that synchronize with the bubble interface displacement. In addition, since the fluid is not inviscid, the bubble, which acts as a mechanical transducer, generates a tangential motion of the fluid at its interface, finally resulting, thanks to the absorption capacity of the medium, in a steady fluid motion called acoustic streaming. We must go back in 1831 in order to find the early beginnings of experimental work on acoustic streaming when Faraday [1831] observed and reported for the first time air streaming that resulted from a vibrating plate, and then, wait 50 years for the first theoretical work accomplished by Rayleigh [1884] with his study on steady air flows between parallel walls. He explained their existence in resonant pipes as a time-independent second order flow driven by the viscous stresses of the fluid, and justified their specific patterns by the presence of the parallel solid boundaries. The association of this phenomenon to a gas bubble amounts first to Kolb and Nyborg [1956] who discovered the generation of microstreaming when the bubble is tethered to a vibrating metal cone, and to Elder [1959] who observed the acoustic streaming of a bubble visualized from a side view, as a function of the fluid viscosity and the acoustic pressure. At that time, Elder stated for the first time that the direction of the flow in a low viscosity medium *"is such as to move the liquid away from the nodes and towards the anti-nodes"*. In these works, nonspherical instabilities of a tethered bubble were reported above certain pressure values, as well as changes in the microstreaming behavior associated to changes in the

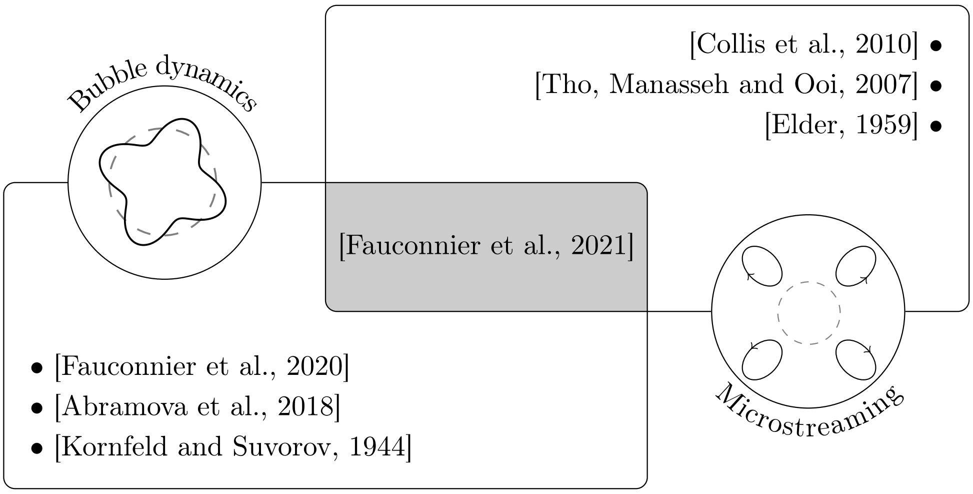

Figure 1.5: Overview of the experimental works on dynamics and/or microstreaming associated to a wall-attached bubble undergoing asymmetric modes.

bubble modal deformations.

Since then, microstreaming induced by a single bubble is investigated through several scenarios, either when undergoing a rigid-body translation motion only [Davidson and Riley, 1971, Longuet-Higgins, 1998, Collis et al., 2010] or when accompanied with a radial oscillation [Gormley and Wu, 1998, Longuet-Higgins, 1998, Marmottant et al., 2006, Bolaños-Jimenez et al., 2017], either when animated by asymmetric modes [Tho et al., 2007], or axisymmetric ones [Spelman and Lauga, 2017, Cleve et al., 2019]. This latter case of triggered axisymmetric modes occurs when bubbles are free of any constraints, acoustically trapped in a standing-wave levitation system [Cleve et al., 2019] or stabilized close to the vortex core of a propagating beam [Baresch and Garbin, 2020]. The investigation of bubble interface motion and induced streaming in an unbounded fluid presents the advantage of allowing the comparison to mathematical models that are based on the assumption of axisymmetric bubble oscillation. Bubble-induced microstreaming generated by the combination of radial, translation or any arbitrary axisymmetric oscillation is now well documented [Longuet-Higgins, 1998, Spelman and Lauga, 2017, Doinikov et al., 2019a,b, Inserra et al., 2020a,b].

Sectoral and tesseral harmonics correspond to asymmetric deformations whose triggering is facilitated when a bubble is close or in contact with a wall. The mathematical description of bubble asymmetric oscillation is complex and brings a bunch of new difficulties when resolving the bubble interface dynamics. As a result, experimental works about fluid flows induced by the asymmetric shape modes of a bubble are very scarce [Collis et al., 2010, Tho et al., 2007, Marmottant and Hilgenfeldt, 2003, Elder, 1959]. In these investigations of microstreaming resumed in figure 1.5, the time-resolved dynamics of the bubble is always left to the side, while it can actually play an important role. One of the reason for this discharge is the complex behavior and interpretation of the bubble silhouette. In this regard, the chapter 3 of this manuscript takes its interest in the revelation of simultaneous measurements of asymmetric bubble dynamics and induced fluid flow in order to correlate the bubble modal content to the experienced microstreaming patterns.

1.5 An overview on sonoporation

Because some in-vivo environments can be difficult to access, a very promising alternative is suggested and consists in carrying out a remote mechanical action on biological cells and tissues by taking advantage of the resonant behavior of acoustically-excited microbubbles working as acousto-mechanical transducers. This allows a non-invasive and localized action on the biological tissues. Also referred as cellular sonication, the sonoporation is the process by which ultrasounds are employed to alter the membrane permeability of biological cells. Intended to have a transient and reversible action, it aims at facilitating the internalization of particles, drugs or genes into the cytoplasm without affecting the cells viability. The real challenge with sonoporation is the control of the irregular bubbles activity that can quickly become chaotic. Too little acoustic energy deposit would result in no cell permeabilization, but too much could irreversibly porate the cell until its complete lysis. To answer this purpose, the use of prefabricated bubbles can be more attractive because it allows a better monitoring and control of the bubbles behavior, facilitated with their tunable and selective frequency response.

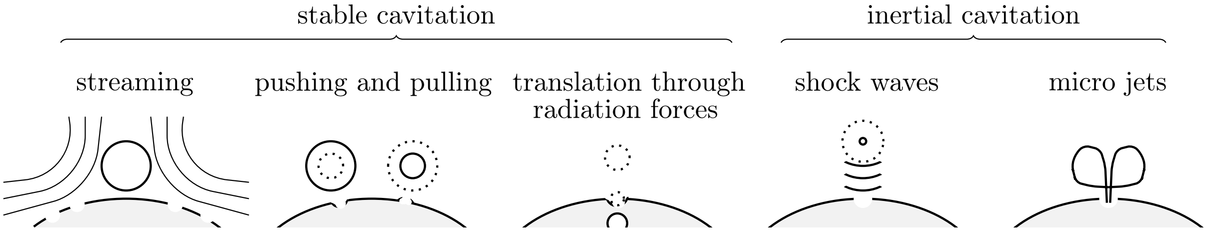

Figure 1.6: Sketches of the different mechanisms possibly leading to cellular sonoporation, which can be induced either by a stable oscillatory regime of ultrasound-driven microbubbles either by an inertial collapsing regime of microbubbles (reprinted with permission from Cleve [2019]).

As it will be discussed in this section, the manifold mechanisms of these ultrasound-driven (or laser-induced) microbubbles, resumed in figure 1.6, are as much possible means to mechanically stimulate and eventually permeabilize nearby biological cells. Among others, this includes the generation of streaming-induced shear stresses, the bubble pushing-pulling action, i.e. the first order acoustic time scale bubble-induced cell deformation, or even the bubble jetting towards the cell membrane. Before going into the detail of this, the methods for measuring the sonoporation will be first described.

1.5.1 Techniques for measuring the rate of sonoporation

There exists several ways for measuring the rate of sonoporation of biological cells. Some rely on the real-time monitoring of the cell activity, while others interpret the effect of bubbles from a post-ultrasound exposure analysis. The former is usually limited to the analysis of cells located in the field of view, but allows a time-resolved understanding of the involved mechanisms. The latter not only covers fast measurements and statistical results of large cells populations, but also consists of the high-definition imaging of sonoporated cells.

Post-US exposure measurement

A biological cell is a dynamic living entity endowed with an ability of resilience and regeneration. The sonoporation aims at the transient and reversible poration of cells membrane. Literature reporting recovery time of sonoporated cells on the order of milliseconds to seconds [Mehier-Humbert et al., 2005, Hu et al., 2013], it could be concluded from these two sentences that measuring the success rate of such a transient phenomenon with an after-the-fact procedure makes no sense. Hopefully, it is possible. The sonoporation can be quantified in an after-the-fact procedure by using a fixative solution added just after insonication or by using fluorescent markers before or during insonication. The possibility of evaluating the rate of intact, successfully permeabilized and dead cells among a large population of sonicated cells is of great interest for investigating the influence of acoustic parameters, the cell-to-bubble distance and different types of microbubbles on sonoporation in a statistical way [Forbes et al., 2008, Yu and Chen, 2014]. The opening times of pores is usually evaluated by adding fluorescent markers at different post-US exposure time delays along repeated experiments, and regarding at the rate of stained cells for each scenario [Mehier-Humbert et al., 2005]. It is worth precising that the counting of cells is performed by flow cytometry, i.e. the optical computer-assisted sorting of a sample of cells labeled with fluorescent markers flowing through a laser beam.

Otherwise, when it is aimed at looking into the outcomes of sonoporation at the single-cell scale and not at a population scale, scanning electron microscopy is employed. This measures the response to an electron beam of a surface to be imaged in order to capture and reproduce its three-dimensional structure at the nanoscale level. Because the poration of the cellular membrane is transient and may recover after a short duration, the state of the cells right after ultrasound exposure can only be visualized by freezing its state with a fixative (e.g. glutaraldehyde). Its application to the examination of the membrane surface of sonoporated biological cells revealed that the sizes of pores is closely related with the size of internalized particles but also with the cellular lethality [Mehier-Humbert et al., 2005], and the bubble-cell distance before ultrasound activation [Zhou et al., 2012].

Real time measurement

Along its living time, an eukaryotic cell continuously interacts with the outside in order to provide itself with nutriments and information. Its so-called calcium pumps are ion channels disposed on its membrane that allow it to communicate with its environment and share information with other cells. The constant concentration of calcium ions (Ca^{2+}) within the cytoplasm is crucial for ensuring these functions and its monitoring allows the detection of abnormal changes in the cellular membrane permeability. It is widely used in research as a means for evaluating the cell viability or the rate of sonoporation caused by oscillating microbubbles [Bose et al., 2011, Deng et al., 2004, Tran et al., 2008, Kudo et al., 2009]. Similar works investigate in a more general way the transmembrane current regulated by these ions channels [Zhou et al., 2009, 2012], which they achieve to relate to an estimation of the bubble-induced pores size. The difficulty in these monitoring techniques remains in the very delicate patch-clamp method that consists in introducing a communicating wire within the cell for measuring these ion quantities. If badly handled, the risk of damaging the cellular membrane with the wire can be high, leading the measurements to be irrelevant with the action of ultrasounds and the bubbles activity. Another way for monitoring the cellular membrane opening and the internalization of particles into the cytoplasm goes through the use of blue trypan [Le Gac et al., 2007] or fluorescent DNA-intercalating dyes. Among others, propidium iodide (PI) [Okada et al., 2005, van Wamel et al., 2006, Kooiman et al., 2011], calcein [Guzman et al., 2003] and TOTO-1 [Escoffre et al., 2010] are perfect candidates to answer this purpose of cell staining.

1.5.2 Multi-cells scale investigation

The effect of ultrasound-driven bubbles on a cell population is usually experimentally investigated as a black box system. Acoustic parameters, types of microbubbles and cells are first described and introduced as experimental conditions. Ultrasounds are then activated and the outcome of the bubbles activity on cells is acknowledged afterwards. At the end, the cells are identified as intact, sonoporated or dead by the internalization of fluorescent markers. The result is the subject of a statistical analysis, but the time-resolved description of the bubbles activity remains unknown. In this configuration, the mechanisms generated by the bubbles activity and involved in the cell sonoporation are difficult, if not impossible, to identify. Nevertheless, the after-the-fact analysis of cells reveals that not only the particles uptake, but also the cell lysis, are correlated with insonication time and acoustic power [van Wamel et al., 2002]. Forbes et al. [2008] reported an optimal rate of sonoporated chinese hamster ovary (CHO) cells with Optison$^{\text{TM}}$ bubbles (GE Healthcare Inc.) at an acoustic pressure of 1.74 MPa and a decrease of sonoporated cells at acoustic pressure above 2.4 MPa, for which 95 % of bubbles were seen collapsing, suggesting that bubbles stable regime was more likely to be responsible for the effective sonoporation than bubbles inertial regime. The 150 kPa insonication of SonoVue® bubbles (Bracco Diagnostics, Inc.) in presence of mouse fibroblasts at a concentration of 8 x 10^6 cells mL^{-1} resulted in 58.3 ± 4.1 % of cells that were sonoporated and still alive [Yu and Chen, 2014]. Most experimental studies of the multi-cells scale sonoporation agree that the cell permeabilization is possible and often more efficient at low-acoustic pressure where a stable regime of microbubbles dominates. An interesting recent work involving an oscillating vapor bubble and its associated streaming within which cells are flowing should also be mentioned [Xie et al., 2016]. The deformation of cells is explained through a numerical simulation of the asymmetric shear stress field and experimentally measured through their change in shape eccentricity (aspect ratio between long and short axis) for different types of cells. The deformations reaching maximal values up to a value of 2.3 for the aspect ratio finally result in sonoporation of cells, evidenced with fluorescent markers.

Lastly, it is worth mentioning a promising variant method of cell membrane permeabilization. The electrosonoporation takes advantage of two modalities of cell poration through the use of electric pulses joined with sonoporation in order to promote the entrance of drug or genetic material into cells. It should be recalled that electroporation historically arrived before sonoporation among the techniques for cellular permeabilization. Escoffre et al. [2010] explore this dual modality technique with the use of plasmid DNA and operate in a two-stages procedure. First the electroporation induces the formation of DNA aggregates on the cell membrane. Then the sonoporation precipitates the aggregates deep into the cell towards the nucleus. This twofold technique showed an increase in the rate of transfected cells and in the transfection intensity per cell in comparison with each technique employed alone.

1.5.3 Single-cell scale investigation

The isolated study of a specific mechanism induced by an ultrasound-driven microbubble is usually done at the single-cell scale through the time-resolved bubble-cell dynamics ensured by a high-frame-rate camera.

Stable regime of an acoustically-driven microbubble

The study of a stable oscillating bubble in the vicinity of a wall takes its interest in the capacity for microstreaming to generate shear stresses on a close boundary, which is widely reported in literature whether it focuses on medical applications [Doinikov and Bouakaz, 2010, Yu and Chen, 2014, Pommella et al., 2015] or for purposes of industrial cleaning [Reuter and Mettin, 2016, Chahine et al., 2016]. In the run for studying the bubble-cell interaction, lipid vesicles have often been used as cellular models. The major advantage comes from their controlled manufacture and therefore from the knowledge of their mechanical and elastic properties that facilitate the comparison with theory.

Among the earliest experimental works are positioned two of the major pioneers in the field, Marmottant and Hilgenfeldt [2003] who pave the way for the manipulation, deformation and rupture of biological cells with a purpose of therapeutic application. They have correlated the path followed by a lipid vesicle caught in the fluid flow generated by a tethered bubble undergoing both radial and vertical translation motion with the streaming model of Longuet-Higgins [1998]. The meeting of the moving and gradually deforming cell with the fixed bubble ends up with its disintegration. One year later, van Wamel et al. [2004] were showing for the first time the acoustic time scale periodic interaction between a biological cell and a radially oscillating microbubble (Sonovue®, Bracco Diagnostics, Inc.). The endothelial cell deformation was quantified with the cellular cross-section close to the microbubble and has demonstrated a 5 µm peak-to-peak amplitude displacement (15.5 µm at rest) induced by the so-called pushing-pulling action of a 8 µm-sized bubble, which reached twice its size at maximal expansion (bubble-cell distance = 3 µm). In a second work, van Wamel et al. [2006] further evidenced the cell permeabilization, assessed by the internalization of PI, due to a similar bubble pushing-pulling action. The reiterated experiment on several cells revealed that most permeabilized cells show no more fluorescent stain after a three minute time recovery, meaning that no permanent lysis occurred. The sonoporation of endothelial cells has also been experienced by Kooiman et al. [2011] with the difference than bubbles were adhering to the cell membrane. Even if the rate of PI uptake seems unrelated with the bubble localization on the cell membrane, it was clear that sonoporation could already occur at low acoustic pressure (80 kPa). In the meanwhile, Marmottant et al. [2008] reiterated their experiment on the deformation of a lipid vesicle caught in a bubble-induced streaming. The observation of the vesicle during one period of the flow looping motion exhibits a prolate shape when coming towards the bubble in the focal plane and an oblate shape when moving away from the bubble outwards the focal plane. This behavior has been theoretically confirmed with the resolved strain rate along the streamline taken by the vesicle. In theory, they determined that a 4 % vesicle excess area was supposed to result in the vesicle breakup, but they never experimentally attained this strain in water due to a too low-viscosity. A similar work investigated the influence of the size and membrane stretching elasticity of vesicles flowing in a bubble-induced streaming on their ability to support important excess area before their breakup [Pommella et al., 2015]. For a same stretching ability, the rupture occurred easier for larger vesicles. Besides these studies, Zhou et al. [2012] studied the cell permeation in a very original way, through the so-called bubble compression. A 10 µm bubble is propulsed by the acoustic radiation force of a 7 MHz pulse towards the membrane of a xenopus oocyte with a $25\,\mathrm{mm \cdot s^{-1}}$ velocity recorded before impact. The monitoring of the transmembrane current unveiled the effective sonoporation, while knowing the magnitude of the radiation force allowed them to estimate the membrane rupture tension to be $1.23 \times 10^{-5}\,\mathrm{N \cdot cm^{-1}}$. Lastly, Moosavi Nejad et al. [2016] presented images of cell membrane deformation caused by a radially oscillating microbubble flowing near the cell. The local expansion estimated at 2.5 µm for a 16.7 µm cell area at rest led to a harmless cellular sonoporation, confirmed by the internalization of fluorescent markers.

This ends the very short list of published works on the mechanical interaction between a stably oscillating microbubble and a cellular model, at the single-cell scale. To our knowledge, no experimental study investigates the pushing-pulling action of a microbubble undergoing nonspherical shape modes at that single-cell scale.

Inertial regime of an acoustically-driven microbubble

As mentioned in section 1.1.2, the formation and immediate collapse of a microbubble can be generated by nucleation methods making use of a laser pulse or an electrical spark discharge. In this way, the fast expansion and collapsing bubble behavior has demonstrated its responsibility in the production of important damages on nearby cells, whether reversible or not. The cell elasticity has shown to be crucial in its ability to resist to the bubble motion, especially during its collapsing phase [Tandiono et al., 2013]. Too elastic cells ended after the bubble disappearance with a very elongated shape, unlike more rigid cells which remained intact. Le Gac et al. [2007] found a bubble-cell critical distance of 0.75 R_{max}, where R_{max} is the maximal expanding bubble radius, below which human promyelocytic leukemia cells had more than 75 % chance to be porated. Qin et al. [2015] also shown that sonoporation induced by a collapsing bubble occurred at short bubble-cell distance and never for a bubble-cell distance larger than the bubble diameter. According to their findings, the sonoporation is mostly a matter of bubble-cell parameters (distance, bubble radius, number of collapsing bubbles) than acoustic parameters, the recurrent irreversible cell disruption taking place exclusively when there is bubble-cell contact or for repetitive collapse of several (>3) bubbles. A condition of bubble-cell contact before ultrasound exposure has also been reported to be responsible for important damage in endothelial cells, which demonstrated a significant rate (70 %) of cell repair within 3 minutes after insonication [Okada et al., 2005].

Theoretical studies

The bubble-cell interaction is also the subject of some theoretical studies, whether investigated through the bubble pushing-pulling action [Gracewski et al., 2005, Zinin and Allen, 2009, Guo et al., 2017, Wang et al., 2018] or through the generation of flow-induced shear stresses [Doinikov and Bouakaz, 2010, Yu and Chen, 2014]. First, it is worth mentioning that to our knowledge no theory unifies these two mechanisms (streaming and first-order strain) in a single model of cell sonoporation. Concerning the shear stresses induced by bubble streaming on a nearby wall, most of actual models propose extensions of the earliest work accomplished by Nyborg [1958] concerning the radial oscillation of a super-hemispherical bubble resting on a infinite rigid boundary in a context of industrial cleaning. For a not-adhering spherically oscillating bubble, the maximal shear stress applying on a boundary occurs at a distance $x \simeq 1.13\ d$ from the bubble center, where d is the distance of the boundary to the bubble center [Doinikov and Bouakaz, 2010]. The Nyborg's model was found to be in accordance with experiments when Yu and Chen [2014] approximated in a probability way the theoretical percentage of sonoporated cells (mouse fibroblasts) to be 64.8 % while their experimental results were approached by the model with a percentage of about 58.3 ± 4.1 % of sonoporated and viable cells. It is worth remembering that these two studies did not account for the cell strain induced by the bubble action at the acoustic time scale, while it can have a huge influence in the process of sonoporation. If we look at the studies carried out on this bubble pushing-pulling action too often set aside in theoretical models, they all consider bubble radial motion only. The cell deformation under the action of a nonspherically oscillating bubble is never considered. Gracewski et al. [2005] report a cell strain and stress decreasing with the cubic radial distance to the bubble. Zinin and Allen [2009] propose a decomposition of a bacteria strain on quadrupole and dipole shapes and report maximal deformations occurring at the acoustic frequency $f_K \sim \frac{1}{2\pi}\sqrt{K_A/(\rho_c a^3)}$ where K_A, ρ_c and a are respectively the surface area modulus, the density and the radius of the cell. Recently, the cell strain was approached with the displacement of the close-to-bubble point (CP) on the cell membrane, as first defined by van Wamel et al. [2004], and was numerically studied through a parametric study of the initial bubble-cell distance, the acoustic pressure and the maximal CP displacement [Guo et al., 2017]. Strengthened with experimental results [Wang et al., 2018], it came out that the analysis of the CP displacement could explain the internalization of particles, which seem to be facilitated with the use of larger bubbles.

1.5.4 Sonoporation induced by bubble nonspherical shape modes

Literature widely reports experimental cases of effective permeabilization of biological cells induced by ultrasound-driven microbubbles animated either by a stable oscillatory regime or by an inertial collapsing regime. Particular emphasis is placed on stable microbubbles whose dynamics are less destructive, but intense enough to sufficiently stimulate nearby cells and facilitate the internalization of particles within them. In this scenario, the most documented bubble-induced mechanism responsible for this generation of stresses is the microstreaming induced by bubble nonspherical shape modes. The pushing-pulling action of a bubble is also exploited but far less documented than microstreaming and actually restricted to bubbles exclusively animated by a radial oscillation, while the presence of nonspherical modes might play an important role, as sketched and conjectured in figure 1.7. To answer this, we suggest through this thesis work to study the mechanical

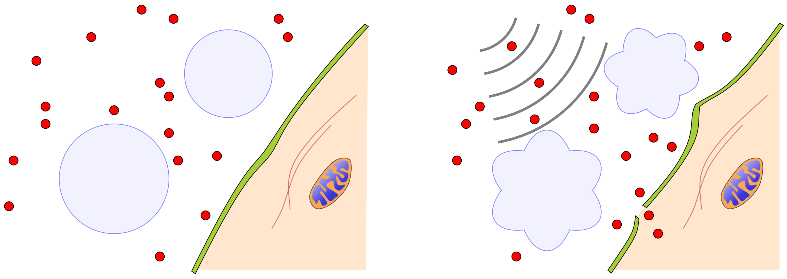

Figure 1.7: Sketches of the permeabilization of a biological cell membrane facilitated by the pushing-pulling action of nonspherical microbubbles under the action of an ultrasound field.

interaction that may exist between an ultrasound-driven wall-attached microbubble undergoing nonspherical oscillations and a nearby biological cell, at a micro-scale level of a couple of one single bubble and one single cell. More exactly, the scheme of investigation is the following:

- Our work is initiated in chapter 2 with the analysis of one single bubble driven by an acoustic pressure field modulated in amplitude. This allows to track the emergence of bubble nonspherical modes and to examine their dynamics under a wide variety of modal configurations.
- Once a better control of the bubble nonspherical oscillations is achieved, the understanding of their induced streaming is the next task in line. The chapter 3 goes around the whole spectrum of fluid patterns generated by each of the main classes of nonspherical modes. Each of these two parts is a step closer to ultimately enable the observation and comprehension of its interaction with a neighboring cell.
- The chapter 4 conjugates these bubble phenomena previously revealed with the addition near the bubble of a biological cell. The cellular response is investigated through several bubble-involved mechanisms and sorts of motion and deformation, for which we will finally attempt to validate the effects by the internalization of fluorescent markers within the cell.

Chapter 2

Nonspherical bubble dynamics

Nonspherically stable oscillating bubbles are responsible for important fluid flows and large amplitude displacements which can possibly lead to considerable shear stresses on nearby cells. For this reason, the knowledge of the conditions of their interface instability and the control of their nonspherical dynamics are key elements to improve their action, while avoiding irreversible damages on biological cells, with an intention of sonoporation. This second chapter, aiming to this end, is devoted to the experimental exploration of the temporal dynamics and selection of the nonspherical oscillations of a microbubble. Before delving into the meat of the issue, section 2.1.1 gives the detail of the experimental method that allows capturing the high-resolved temporal dynamics of an ultrasound-driven wall-attached bubble, in a top-view configuration. This also includes a quick description of the applied methods for the characterization of the acoustic field. Section 2.1.2 proposes an alternative and occasional setup in which the bubble is observed from a double (top and side) perspective. Quickly abandoned due to the difficulty in such a setup to lay an adhering biological cell near a bubble, it mostly helps to illustrate the issue in visualizing the bubble nonspherical modes in a single-view. Also, it makes possible to estimate the contact angle of the bubble at rest. Section 2.2 studies the nonspherical behavior through several steps. With a preliminary introduction on the problematic and involved challenges in the modal identification explained in section 2.2.1, the seeking for the emergence of nonspherical modes under the action of an increasing acoustic driving is presented in section 2.2.2 for sectoral modes and in section 2.2.3 for all nonspherical modes in general. Integrated into this section are the numerical and experimental validations of our modal analysis tool, enabling the identification and detection of the set of zonal ($m = 0 < n$), tesseral ($0 < m < n$) and sectoral ($m = n > 0$) spherical harmonics that develop at the bubble interface. Therefrom, section 2.2.4 points out the modal nondegeneracy of spherical harmonics of a wall-attached bubble. The selection of specific modes is interpreted by the inhibiting action of the contact on the nonspherical deformations, and compared to the well documented case of a sessile drop in section 2.2.5. Lastly, section 2.2.6 draws particular attention to the interaction between zonal and sectoral modes and deepens the possible conditions for their coexistence.

2.1 Methodology

2.1.1 Top-view experimental setup

A schematic of the experimental setup is given in figure 2.1a. Observations of ultrasound-driven microbubbles are performed in a polymethyl methacrylate (PMMA) tank of inner size $L_x \times L_y \times L_z = 44 \times 260 \times 50$ mm. Experiments are conducted in pure (Milli-Q® IQ 7000) water supplemented with saline solution ($NaCl$ concentration of $24 \pm 1\,\mathrm{mg \cdot L^{-1}}$). A dihydrogen microbubble is created, resulting from a reduction reaction and occurring at the cathode of an electrolysis actuator. The electrolysis is actuated by a signal generator (Agilent 33210A, squared signal, peak-to-peak amplitude $4\,\mathrm{V_{pp}}$, offset $2\,\mathrm{V_{pp}}$, 50 % duty cycle). The cathode connector is tied up to a three-axis hydraulic micromanipulator (Narishige MMO-203), which allows the positioning and tethering of the bubble at the tank's bottom. Once that is accomplished, the electrolysis wire is moved away so that it does not interfere with the oscillation of the attached bubble. In this way, single bubbles of equilibrium radius ranging from 60 to 230 µm may be nucleated.

The driving acoustic field is induced by a Langevin transducer (Sinaptec®, 30 kHz nominal frequency, high-voltage gain amplifier Trek50/750) located at one edge of the water tank and described in details in section 2.1.1. Acoustic coupling between the transducer and the water tank is ensured with ultrasound transmission gel (Aquasonic,

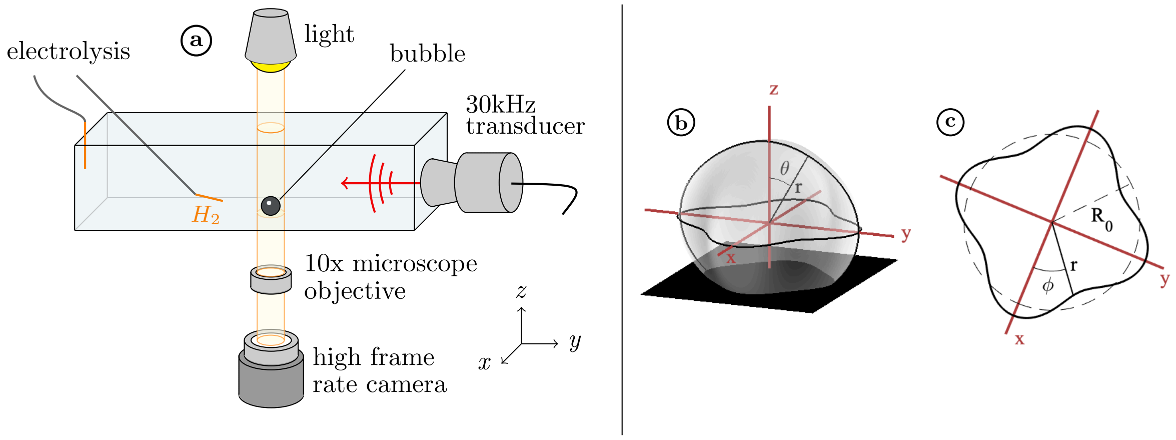

Figure 2.1: Schematic representation (not to scale) of the experimental setup (a) and geometry of the system under study: Three-dimensional (b) and top-view (c) representations of a numerical bubble animated with a spherical harmonics of degree $n = 4$ and order $m = 4$, called sectoral when $n = m$. The bubble interface is characterized using spherical coordinates (r, θ, ϕ).

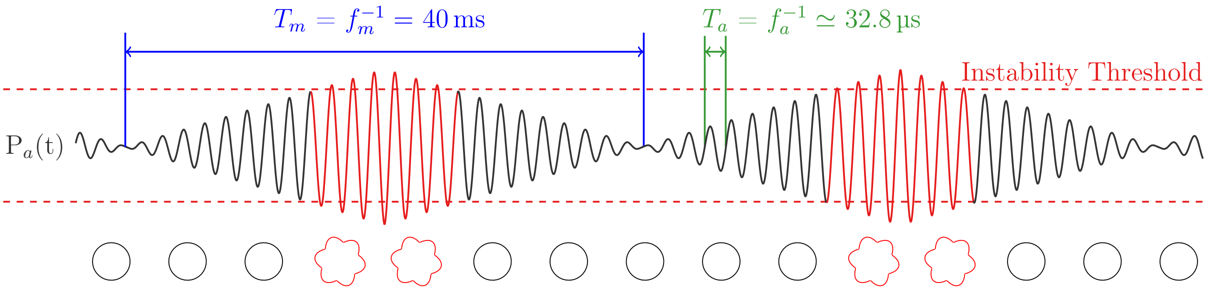

Figure 2.2: Schematic representation of the driving signal: a sine wave of frequency $f_a = 30.5\,\text{kHz}$ modulated by a triangle shape envelope of frequency $f_m = 25\,\text{Hz}$.

Fisher ThermoScientific). Similarly to previous works investigating bubble shape deformations [Guédra et al., 2016], bubbles are insonified by a sinusoidal signal modulated by a slowly-varying envelope in order to periodically trigger bubble interface instabilities, and hence the shape modes, as illustrated in figure 2.2: a triangle shape envelope of modulation frequency $f_m = 25\,\text{Hz}$ is superimposed to a sine wave of frequency $f_a = 30.5\,\text{kHz}$. The visualization of the bubble's activity is performed using an inverted Nikon Eclipse-Ti microscope equipped with a 10× magnification optical lens. The bubble dynamics is captured by means of an high-speed CCD camera (Vision Research, Phantom V12.1). The geometry of the studied bubble is schematized in figures 2.1b and 2.1c, for the case of a sectoral ($n = m$) mode of degree $n = 4$. The image scale has been measured to be $2\,\mu\text{m}$/pixel, thence a numerical inaccuracy of $2\,\mu\text{m}$. Movies are performed with acquisition parameters (frame size, sampling frequency and exposure time) that are bubble size dependent, as described in table 2.1. Such adjustment is necessary to optimize the field of view for a broad range of bubble radii.

Bubble radius	**Frame size**	**Sampling frequency**	**Exp. time**
$R_0 < 124\,\mu\text{m}$	128 × 128 pixels	180 064 Hz	4 µs
$R_0 > 124\,\mu\text{m}$	256 × 256 pixels	67 065 Hz	7 µs

Table 2.1: Acquisition parameters (frame size, frame rate and exposure time) as set in the software Phantom Camera Control (PCC).

Transducer acoustic characterization

The acoustic transducer employed is a Langevin sensor Sinaptec® with nominal frequency 30 kHz. Following Minnaert's expression of equation (1.5), the corresponding resonant radius of a bubble driven in water equals $108.7\,\mu\text{m}$. For the purpose of studying the dynamics of a single bubble, this functioning frequency is suitable for working with relatively

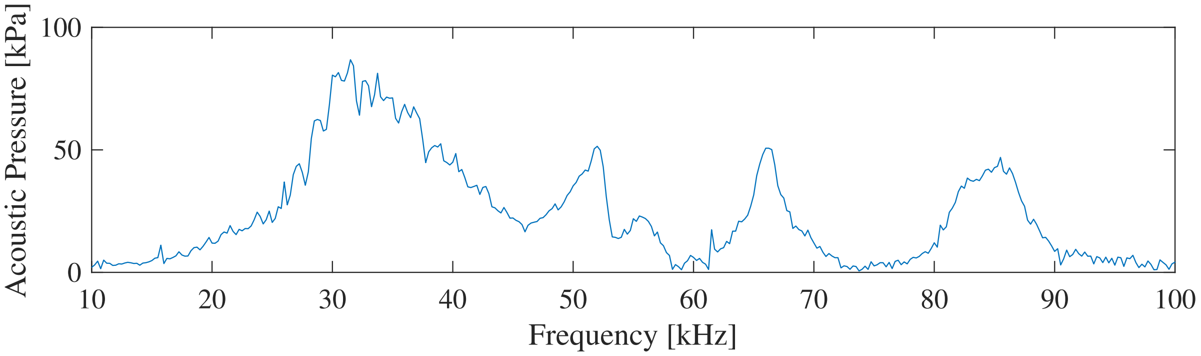

Figure 2.3: Frequency response of the electroacoustic chain consisting of a Langevin transducer of nominal frequency 30 kHz and a high-voltage gain amplifier Trek50/750. It is obtained by Fourier transform of its response to a 3 V amplitude Dirac signal.

large bubbles with radius sizing in the range 60 to 230 µm, whose resonance frequency varies in the range 14 to 54 kHz.

The frequency response of this transducer and its associated high-voltage gain amplifier Trek50/750 has been obtained from their response to a Dirac signal, recorded by an hydrophone (Sinaptec® TC-4034 ± 2 dB in the range 10-100kHz) positioned at a 1 mm distance from the Langevin surface active area. Drawn in figure 2.3, it unveils that the transducer possesses three harmonics at 52 kHz, 66.5 kHz and 85 kHz, which could be useful for working with smaller bubbles. As we shall see later on, in chapter 4, in order to study the coupling between a biological cell and a bubble, we are seeking to work with smaller bubbles in order to have a size correspondence with the cells. The transducer's 85 kHz third harmonic will then be very useful to insonify bubbles with radii in the range 20 to 45 µm.

Acoustic field characterization

The procedure to assess the acoustic pressure driving the bubble is the following. Before all else, the recording time τ_{rec} is set so that it is just longer than two modulation periods: $\tau_{rec} > 2T_m$. This ensures to have at least one complete modulation period in the captured sequence. Considering that the modulation envelope is slowly varying, i.e. $f_m \ll f_a$, the ultrasound field may be assumed to be a constant-amplitude sinusoidal signal during a few acoustic periods. At the beginning of the triangle modulation waveform, the acoustic pressure is low enough to induce relatively weak radial oscillations of the bubble. By capturing this radial dynamics and rearranging it on a single acoustic period, the obtained waveform can be numerically compared to the linearized Rayleigh-Plesset expression of equation (1.4) ruling the bubble spherical oscillations at low pressure, as detailed in section 1.2. As all other parameters are known or can be directly measured (fluid viscosity and density, bubble equilibrium radius), the acoustic pressure can then be deduced from this modeling. This technique is reproduced for increasing driving voltage as far as the bubble interface remains spherical. Then, acoustic pressures associated to bubble nonspherical oscillations are extrapolated linearly along the whole experimental data set. The applied pressures go up to 60 kPa.

2.1.2 Some occasional bubble side-views

Prismatic bubble

Before going further in the investigation of bubble nonspherical shape modes, we would like to propose first a typical example of bubble vibration sequence as we experienced it along an increasing pressure ramp. To illustrate the bubble shape modes possibly involved and the difficulty to visualize them from a single-view, an alternative configuration for the bubble visualization is proposed. It is very important to note that this alternative setup that will be described here is exclusively limited to this section 2.1.2, and in some other rare occasions, for which it will be explicitly specified. This configuration differs from the one previously described in section 2.1.1 by the positioning of the camera on the side of the tank. Thanks to the tethering of the bubble on a suspended glass slide located in front of a reflecting straight prism, the simultaneous observation of the bubble from a direct side-view and from a reflected top-view is possible, at a frame rate of 120 171 Hz.

One might think then, why not having used this setup throughout this whole thesis work. The reason comes from the difficulty in such a configuration to place one of our biological cells on the glass slide, rather than in the bottom of the PMMA tank. We will see in chapter 4 how the manipulation of our cells can be quite complicated. It must be remembered that, ultimately, the positioning of the cell in front of the bubble is above all one of the objective of this thesis, in order to allow the study of the mechanical interaction between a nonspherical microbubble and a biological cell.

Accordingly, an example of observed bubble dynamics is shown in figure 2.4 for which the progressively increasing acoustic pressure reveals a vibration sequence successively marked by four different modal configurations: a radial mode only, a zonal mode Y_{50} only, the combination of the same zonal mode Y_{50} and a sectoral mode Y_{55}, and finally a tesseral mode Y_{53} only, respectively shown in figures 2.4a, 2.4b, 2.4c and 2.4d.

This so-called prismatic bubble, failing not to exhibit a clear sight of its contact line, had the merit of allowing its double (side and top) view. This helped us to understand how the top-view visualization of a zonal mode can be misleading (see figure 2.4b), or how much the visualization of a tesseral mode (in this case, a mode Y_{53} in figure 2.4d), from a single side-view can be confusing as soon as the bubble orientation is not controlled or known. These elements gave us information that seemed important to us in establishing our modal bubble analysis strategy that will be further described in this chapter and the

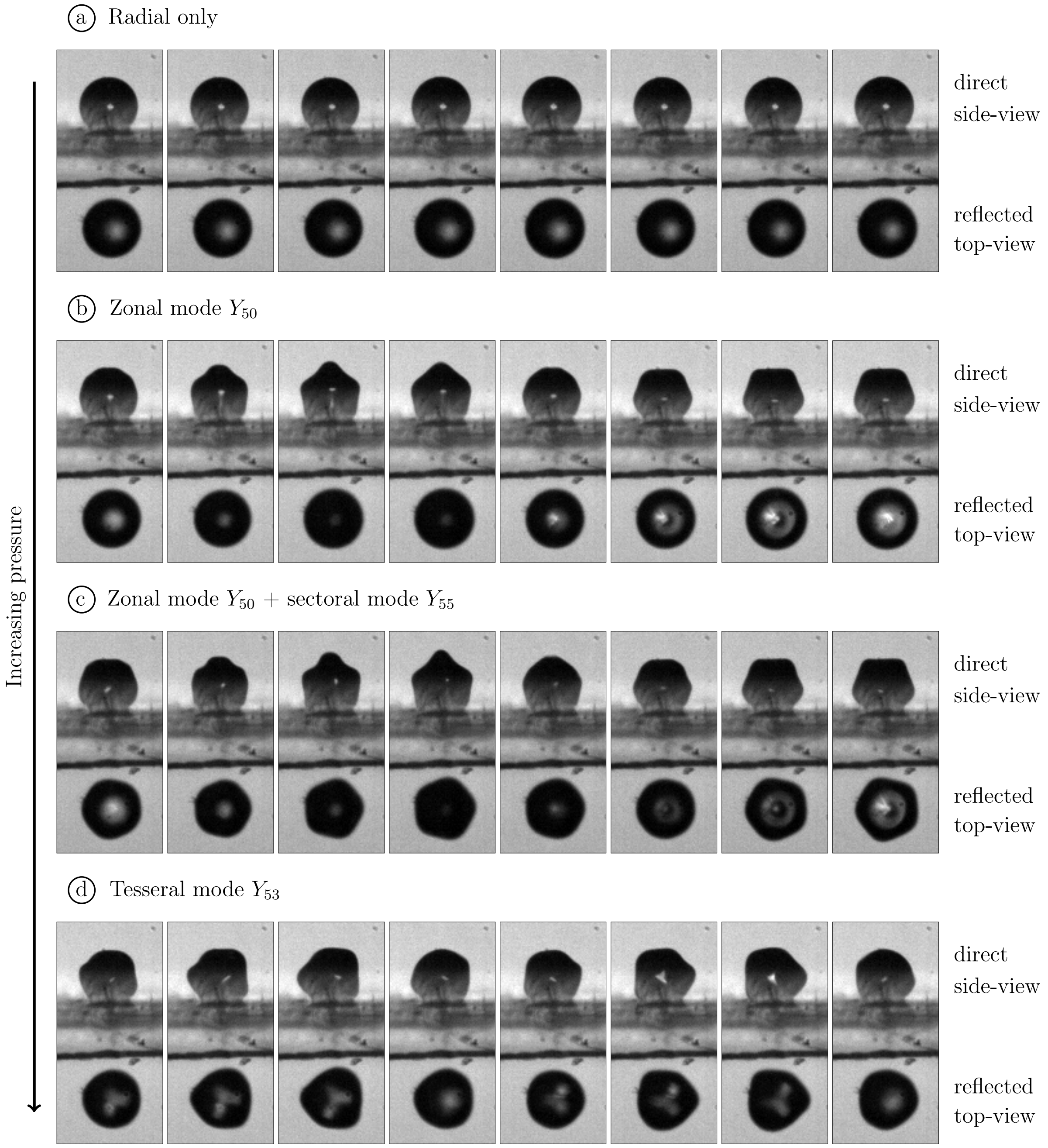

Figure 2.4: Experimental observation of an oscillating microbubble positioned on a glass slide, in front of a reflecting straight prism. The video frame contains both its direct side-view and its reflected top-view, while animated by a radial mode only (a), a zonal mode Y_{50} only (b), a combination of a same zonal mode Y_{50} and a sectoral mode Y_{55} (c) and a tesseral mode Y_{53} only (d).

next one. More specifically, it reinforced our belief that, as long as a choice had to be made between one view or another, the top-view seemed the most appropriate in order to study the sometimes very complex modal behavior of the bubble. To this is added the obvious fact that the top-view visualization performed under microscope allows in definitive a better imaging resolution.

Equilibrium bubble shape

In order to have clearer sight on the contact and to evaluate the conditions at the bubble contact in the main configuration, the straight prism and the glass slide were abandoned and the bubble was tethered at the PMMA tank's bottom. Figure 2.5c shows an experimental image of a side-view of the attached bubble. The way this bubble is standing on the surface and the value of the angle α it forms at the contact result from the wetting properties of water, i.e. the capacity of the liquid to wet the substrate. It is especially ruled by the interface tensions that exist between the different media (gas, liquid and solid) and is, at a first glance, independent of the bubble radius at rest. In a condition of hydrophobic substrate, the wetting of water is weak and the bubble has a sub-hemispherical shape ($\alpha > 90°$). In a condition of hydrophilic substrate, the wetting of water is high and the bubble has a super-hemispherical shape ($\alpha < 90°$), as it is the case with our experimental tank made of PMMA. Geometrically, this contact angle α is defined by the angle formed by the tangent to the bubble surface at the contact point and the substrate plane. Measurements have been performed before ultrasound activation for a large number of single attached bubbles, in a side-view configuration. The angle $\alpha = \mathrm{asin}(L/2R_0)$ is obtained from the optical measurement (see figure 2.5c) of the bubble radius R_0 and the diameter of the bubble base L via the ImageJ software [Schneider et al., 2012]. It came out that it has indeed no dependency with the bubble radius (see figure 2.5a) and it equals 51 ± 7° (see figure 2.5b). The large dispersion in the measured contact angles comes from the fact that it is highly dependent on the way the bubble has been deposited on the surface [Noblin et al., 2009]. Because of an hysteretical behavior, the contact angle of sessile bubbles and drops can take values in a large range. It is worth also noting that the contact angle at rest appears to be larger with PMMA, than it was in the case of the glass contact, in

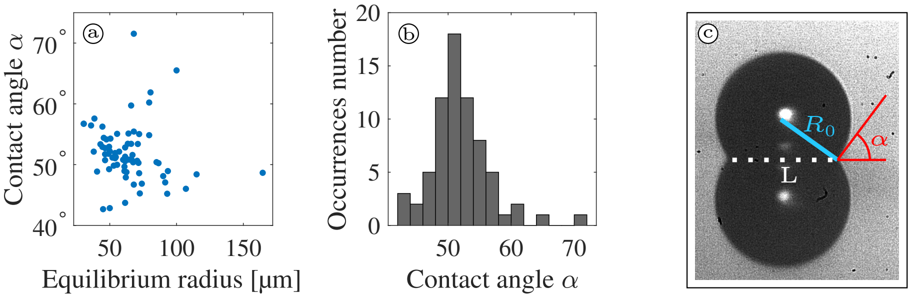

Figure 2.5: Investigation of the bubble contact angle $\alpha = asin(L/2R_0)$, as a function of the bubble equilibrium radius (a) and as a frequency distribution (b), allowed by the optical measurement from a side-view of the bubble radius at rest R_0 and the contact diameter L (c).

figure 2.4a where the bubble was gently radially oscillating. We have also noticed that after ultrasound activation, as long as the bubble does not shift from its original location, the contact angle at rest does not significantly change for a same bubble.

For our experimental bubbles of radius in the range 60 to 230 µm defined in water by the liquid-gas interface tension ($\gamma_{gl} = 72.8\,\mathrm{mN}\cdot\mathrm{m}^{-1}$ at 20 °C in contact with air), we are confident in the absence of a significant influence of the bubble size on the contact angle since the adhesion force $F_r = \pi L \gamma_{gl} \sin\alpha$ (ranging between 12 µN and 47 µN) that applies at the bubble base of diameter $L = 2R_0 \sin\alpha$ on the substrate is much greater than the Archimedes' buoyancy force F_a (ranging between 8.2 nN and 0.46 µN) that applies on the same bubble of truncated volume $V = \pi R_0^3(2/3 + \cos\alpha - 1/3\cos^2\alpha)$.

2.2 Experimental investigation of nonspherical modes

2.2.1 Shape modes observation

In this experimental configuration of a bubble visualized under a microscope, the only accessible information concerning the bubble shape is its top-view contour. Throughout this manuscript, the bubble contour will also be equivalently designated as bubble's silhouette. It is obtained after normalization, thresholding and binarization of the experimental image. Once obtained, the difficulty to analyze the bubble modal content lies in the interpretation of the silhouette of the bubble for which each point can possibly be located at different longitudes. This problem does not arise for radial and sectoral modes but well for the more complex shapes of tesseral and zonal modes, for which the longitudinal angle responsible for the apparent contour is constantly changing.

Applying an amplitude-modulated ultrasonic field results in a beating behavior of the spherical oscillations of the bubble, with a period $f_m^{-1} = 40$ ms, and variations of the radial mode $a_{00}(t)$ alternating between low-amplitude and high-amplitude phases. During one modulation period, if the applied pressure exceeds the threshold of nonspherical oscillations, then the bubble interface deviates from sphericity. Typical examples of the recorded series of pictures are shown in figure 2.6 where the onset of nonspherical oscillations on spherical harmonics of degree $n = 6$ has been reached. The snapshot series is plotted on four acoustic periods, revealing the subharmonic behavior of the nonspherical oscillation resulting from the parametric excitation by the radial mode. For each experimental snapshot series, the observed nonspherical mode is compared with top- and side-views of the corresponding theoretical spherical harmonic. We recall that, at first glance, no axisymmetry hypothesis can be made on the obtained bubble interface, and the bubble contour should consequently be decomposed over the set of spherical harmonics.

In figure 2.6a, a bubble of equilibrium radius $R_0 = 133.7$ µm exhibits an easily recognizable contour with a 6-lobe shape. This case illustrates the shape deformation along a

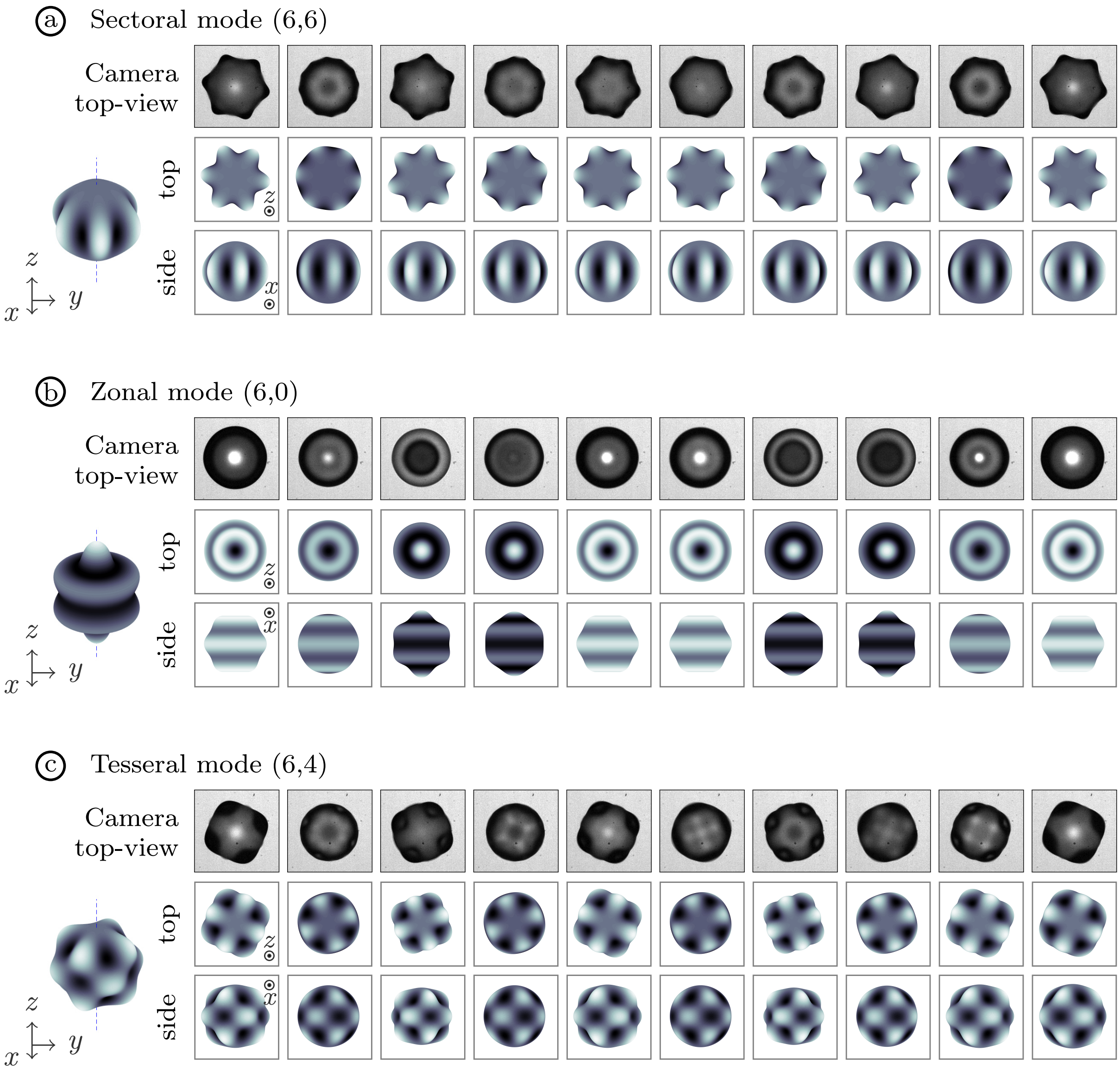

Figure 2.6: Snapshot series of an experimental (camera top-view) bubble, with its associated theoretical spherical harmonics (top- and side-views), oscillating on a sectoral mode Y_{66} (a), on a zonal mode Y_{60} (b) and on a tesseral mode Y_{64} (c). The elapsed time between two consecutive snapshots is 14.9 µs. Oscillations over two acoustic periods are displayed.

sectoral harmonic Y_{66} for which the top-view corresponds to a n-lobe deformation. From the side-view, a sectoral harmonic is close to a spherical shape as the associated Legendre polynomial can be reduced to $P_{nn}(cos\theta) \sim sin^{n}(\theta)$, that is a bell-shape function with zero values at the poles. In figure 2.6b a bubble of equilibrium radius $R_0 = 131.5\,\mu\mathrm{m}$ exhibits spherical oscillations from the top-view, with some additional interface motion along the elevation visible due to optical effects. This case illustrates the shape deformation along a zonal harmonic Y_{60}. As a reminder, zonal harmonics are axisymmetric functions: their contour looks spherical from a top-view and their shape deformation from the side-view is a Legendre polynomial ($m = 0$). At first, identifying this axisymmetric shape uniquely from its top-view is not straightforward. Finally, figure 2.6c illustrates the shape deformation along a tesseral spherical harmonic Y_{64}, for a bubble with equilibrium radius $R_0 = 131.3\,\mu\text{m}$. In this case, the shape deformation becomes more complex with angular deviations from the sphere along both the elevation and azimuthal directions. It is worth reminding that a Y_{nm} spherical harmonic possesses $n - m$ nodal lines along the elevation. Due to the phase interplay of the associated Legendre polynomial between two successive nodal parallels, the azimuthal shape governed by a $cos(m\phi)$ function is out-of-phase with the previous one. The top-view integration of a Y_{nm} tesseral harmonic provides a seemingly $2m$-lobe bubble contour. In the case illustrated in figure 2.6c, the nonspherical mode Y_{64} shows indeed an 8-lobe top-view contour. Among the possible nonspherical oscillations decomposed over the zonal, tesseral or sectoral harmonics, bubbles oscillating along a sectoral harmonic ($m = n$) are the ones easily recognizable in a top-view configuration. By decomposing the bubble contour on a $cos(n\phi)$ function, the onset of a sectoral harmonic may be deduced during the amplitude-modulated pressure driving, leading to the instability threshold for this particular asymmetric oscillation.

Lastly, it is worth saying that the shades of light that constitute the bubble interface, induced by the optical path, can also bring some information about its modal content. Yet they are difficult to be used in an image post-processing algorithm due to some variability in the light patterns for a same bubble modal content.

2.2.2 Degree n differentiation

The detection of the emergence of sectoral harmonics has been performed for approximately two hundred bubbles of radius in the range [60 230] µm. Note that because our experiments are conducted at a fixed driving frequency, the excited shape mode mainly depends on the bubble size and driving pressure amplitude. All results are presented in a radius-pressure map in figure 2.7. Bubbles showed nonspherical oscillations on sectoral harmonics with degree ranging from $n = 3$ to $n = 11$. The analysis of their temporal evolution revealed that they oscillate at half the driving frequency, and consequently, are all triggered on their first parametric resonance. Figure 2.7 highlights the fact that each degree-n sectoral oscillation is exclusively associated to a specific range of bubble size. This non-overlapping feature is similar to the partitioning of axisymmetric modes related to the bubble radius [Cleve et al., 2018]. We therefore compare the experimental instability threshold for sectoral harmonics to the theoretical ones obtained in case of axisymmetric shape oscillations of free bubbles, implemented following equation (1.12). At high degree, an important modal density did not allow us to observe and report bubbles exclusively oscillating on a sectoral mode. This is the case for degrees $n = 8$, $n = 9$ and $n = 11$, where particular shades of light on the bubble interface, visible in figure 2.7,

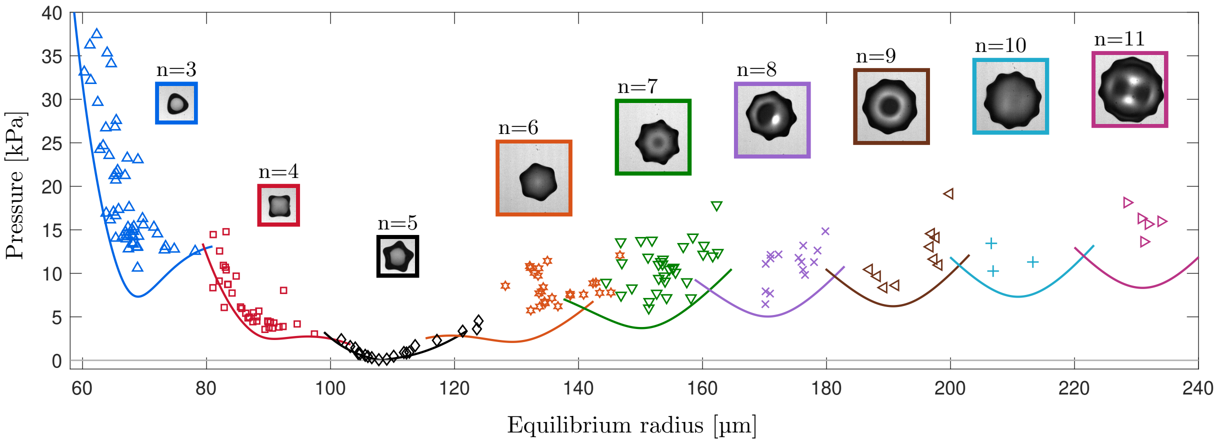

Figure 2.7: Instability thresholds of sectoral harmonics ($m = n$) as a function of the bubble equilibrium radius. Experimental wall-attached bubbles (geometric markers) are compared with free bubble theory (solid lines), according to Francescutto and Nabergoj [1978]. Depending on the bubble size, the frame dimension varies following table 2.1.

betray the presence of nonspherical modes other than sectoral.

2.2.3 Order m differentiation

Due to the partitioning of the degree-n spherical harmonics with the bubble equilibrium radius, we may now postulate that the index n is known once the bubble radius is measured. Appendix A.1 reinforces this postulate with the visualization of bubble shape modes from an alternative side-view. Therefore, specific strategies can be designed to extract the value m of a given spherical harmonic, paving the way to the differentiation of the set of zonal, sectoral and tesseral harmonics. We recall that, from a top-view, the appearance of zonal harmonics Y_{n0} results in a circular contour. The differentiation of this nonspherical oscillation from a purely radial one is performed through the analysis of its subharmonic behavior. It is worth noting that this feature differs from the very similar case of a vertically-vibrated sessile drop, for which the zonal mode must synchronize with the driving base and oscillate at the fundamental [Chang et al., 2013]. In the same way, the appearance of a sectoral harmonic Y_{nn} results in a n-lobe contour in top-view. This shape oscillates at half the driving frequency due to parametric excitation. The combination of the spatial (contour) and temporal (subharmonic) information on a $\cos(n\phi)$ projection confirms the existence of a sectoral mode. The main difficulty lies in the identification of a tesseral ($0 < m < n$) mode. As discussed in section 1.3.1 and figure 2.6, a spherical harmonic possesses $n-m$ azimuthal nodal lines due to the property of the associated Legendre polynomial P_{nm}. When $n-m \neq 0$, the phase interplay between successive nodal lines induces the top-view contour to have a seemingly $2m$-lobe shape. More exactly it consists of two sets of m-lobe disposed in a staggered arrangement, whose

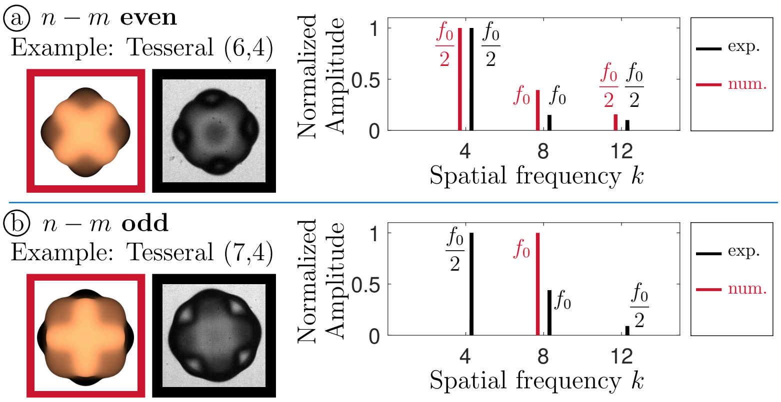

Figure 2.8: Change in spectral signature due to nodal lines parity. Spatiotemporal Fourier decomposition of the bubble contour $r(\phi, t)$ (normalized amplitude), processed for numerical (in red) and experimental (in black) cases of spherical harmonics Y_{64} (a) and Y_{74} (b). The discrepancy between numerical and experimental cases comes from the ombroscopic-induced artefact that affects the optical image but not the numerical projection. This is amplified in the $n - m$ odd situation due to the existence of a nodal line along the equatorial plane.

amplitude displacement may differ according to the parity of $n - m$. This property is illustrated in figure 2.8 and discussed here with two exemplary cases.

When $n - m$ is even, the bubble interface is symmetric with respect to the equatorial plane $\theta = \pi/2$. The top-view contour exhibits a $2m$-lobe shape, consisting of two sets of m-lobe shape with different amplitudes. This behavior results in two spatial harmonic components (referred as ϕ-components in what follows) of the azimuthal contour $r(\phi, t)$ at the frequencies m and $2m$. This is highlighted in figure 2.8a for a Y_{64} tesseral harmonic. In addition it can be shown that the ϕ-component m oscillates temporally at the subharmonic frequency $f_0/2$, while its spatial harmonic $2m$ oscillates at the driving frequency. This temporal characteristic allows especially the differentiation of an order-m tesseral harmonic from a sectoral harmonic in the special case $n = 2m$, for which the spatial ϕ-component n oscillates at $f_0/2$.

When $n-m$ is odd, the bubble interface exhibits a nodal line along the equatorial plane. The top-view contour exhibits then a $2m$-lobe shape, consisting of two sets of m-lobe with equal amplitudes. The spatial projection of the azimuthal contour $r(\phi, t)$ mainly contains the ϕ-component $2m$, oscillating at the driving frequency. This is shown in figure 2.8b for a Y_{74} tesseral harmonic. In this case the numerical projection of the bubble interface is reduced to the ϕ-component $2m = 8$. The identification of the order $m = 4$ is thus not straightforward. Fortunately, experimental conditions always contain the ϕ-component m due to the ombroscopic image sharpness, that naturally induces some difference in lobe amplitudes depending on their position in elevation, as shown in figure 2.8.

A lack that one could find in this preceding explanation of the difference in spatial content based on the parity of the modal numbers is that it does not take into account the spacing between each nodal parallel. For instance, the modes Y_{72} and Y_{52} have a same parity of nodal parallels, but the difference of spacing between each of them may result in a more important focal difference between two successive m-lobe azimuthal shapes and thus in a more pronounced harmonic content in the case of the mode Y_{52} for which the 3 nodal parallels must cover π radians, while there are 5 of them, less spaced, in the case of the mode Y_{72}. Due to this ombroscopic image, a greater sharpness of the bubble contour and thus a more accurate modal analysis must be expected for bubbles with higher number of nodal parallels.

An additional explanation for the difference between theory and experiment displayed in figure 2.8 results from a very constructive epistolary exchange we had with Professor A. Maksimov. The subject matter of the bubble contact and its induced effects on the nonspherical shape modes was addressed. More exactly, the question concerned the geometry of spherical harmonics in the case of a free bubble and how the tethering induced a possible shift in the positioning of the nodal parallels in elevation on the bubble interface. Following this theory, this would also induce a shift of the equatorial line and thus the appearance of spatial harmonics and subharmonics in the top-view bubble contour while there was none in the theoretical description of the Y_{74} bubble mode in figure 2.8b. In these conditions, the use of spherical harmonics for describing the interface of a wall-attached nonspherical bubble is compromised. This issue will be further discussed apart, in appendix A.1.

In definitive, the combined spectral analysis along both space and time can reasonably allow the differentiation of the order m of any spherical harmonics and is particularly convenient for the detection of tesseral harmonics, for which the geometric identification is not straightforward. This process is implemented through a spatial Fourier transform of the top-view bubble contour $r(\phi, t)$ along the angular coordinate ϕ:

$$c_{nk}(t) = \int_0^{2\pi} r(\phi, t)\ e^{-ik\phi} d\phi, \text{ with } 0 \leq k \leq 2n, \tag{2.1}$$

where $c_{nk}(t)$ is the modal coefficient associated to the ϕ-component k of degree n. According to the above-mentioned identification process of the order-m tesseral harmonics, each $c_{nk}(t)$ coefficient is further filtered around the driving frequency $f_0 = 30.5\,\text{kHz}$ and the subharmonic frequency $f_0/2 = 15.25\,\text{kHz}$. For each mode Y_{nm}, the spatial harmonic $k = 2m$ is used for the identification of its order m, while the $k = m$ coefficient $c_{nm}(t)$, oscillating at $f_0/2$, is presented in the following as its modal amplitude. It is worth noting that this modal coefficient differs from the theoretical one a_{nm}, as defined in equation (1.10), due to a bias in the projection's decomposition.

Method validation: numerical case

A validating example of the proposed identification process is performed through the numerical analysis of the bubble nonspherical dynamics and its top-view contour. A virtual bubble of arbitrary equilibrium radius R_0 is submitted to a sine wave modulated by a ramp envelope. The bubble interface is implemented as follows

$$r(\theta, \phi, t) = R_0 + \frac{t}{\tau} a_{00}(t) Y_{00} + \sum_{n \neq 0, m} a_{nm}(t) Y_{nm} H_T(t - t_m), \tag{2.2}$$

where $a_{nm}(t) = a_{nm} \cos(\pi f_0 t)$ and $a_{00}(t) = a_{00} \cos(2\pi f_0 t)$ are the time-varying amplitudes of, respectively, the subharmonic nonspherical modes and the radial mode, $\tau = 20\,\mathrm{ms}$ is the signal duration and H_T is the Hanning operator of duration $T = 6\,\mathrm{ms}$ centered at time $t_m + T/2$. Figures 2.9a and 2.9b present two modal decomposition of a bubble interface exhibiting a breathing mode a_{00}, as well as zonal Y_{60}, sectoral Y_{66} and tesseral Y_{64} harmonics. The case in figure 2.9a (respectively figure 2.9b) corresponds to the onset times $(t_0, t_4, t_6) = (4, 8, 10)$ ms (respectively $(8, 10, 4)$ ms). Numerical top-view snapshots of the bubble contour help illustrate the shape deformation induced by these nonspherical oscillations. The result of the spatiotemporal analysis of the bubble contour is provided by the envelopes $c_{nm}(t)^*$ of the modal coefficients $c_{nm}(t)$ oscillating at the subharmonic of the driving frequency. For both cases, the onset times of the implemented nonspherical modes appear correctly tracked and defined. The maximal amplitudes of the oscillations

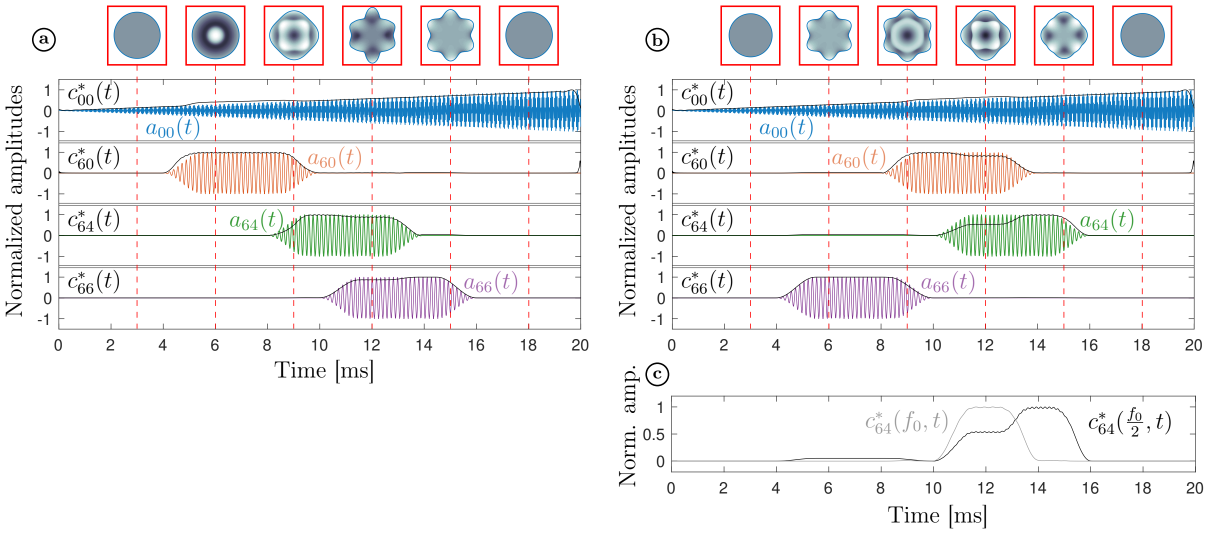

Figure 2.9: Modal decomposition of a top-view bubble contour including the Y_{60}, Y_{64} and Y_{66} modes triggered at time (t_0, t_4, t_6) superimposed to a breathing mode Y_{00}. Comparison of the coefficients $c^*_{nm}(t)$ with the theoretical ones $a_{nm}(t)$ in case of (a) $(t_0, t_4, t_6) = (4, 8, 10)$ ms and (b) $(t_0, t_4, t_6) = (8, 10, 4)$ ms. (c) Evidence of amplitude transfer between the subharmonic $c^*_{64}(\frac{f_0}{2}, t)$ and fundamental $c^*_{64}(f_0, t)$ coefficients of the Y_{64} tesseral mode.

is in good agreement with the theoretical ones, except in two circumstances. The first one concerns the quantification of the radial oscillation when a zonal harmonic appears, leading to a slight overestimation of the breathing mode amplitude. The second one concerns the amplitude of the tesseral harmonic Y_{64} when combined to another nonspherical mode (figures 2.9a and 2.9b). In this case, a part of the modal amplitude is contained into the $2m$ frequency component oscillating at the driving frequency, in accordance to the proposed spatiotemporal analysis and filtering. This amplitude transfer between $c_{64}(f_0, t)^*$ and $c_{64}(\frac{f_0}{2}, t)^*$ for the second exemplary case is illustrated in figure 2.9c.

Method validation: experimental case

The spatiotemporal analysis is applied to an experimental case. This allows characterizing the bubble vibration sequence consisting of the set of successively-triggered nonspherical modes. Figure 2.10 presents two experimental wall-attached bubbles of equilibrium radii 133 µm and 83 µm that deviate from spherical shape in the set of $n = 6$ and $n = 4$ spherical harmonics, respectively. In addition to snapshot series of the top-view contour, the envelopes $c^*_{nm}(t)$ of the modal coefficients that are dominantly excited are shown. The bubble interface presented in figure 2.10a follows the successive vibration sequence $Y_{60} - Y_{64} - Y_{66}$ once nonspherical oscillations appear. The existence of these modes is clearly visible on the top-view snapshots, giving confidence into the proposed analysis. When the zonal mode emerges, the amplitude of the radial oscillation decreases. This phenomenon can be associated to a possible energy transfer between modes [Guédra et al., 2016], but also to a bias in the determination of the amplitude of the modal coefficient $c_{nm}(t)$. Therefore the analysis of mode coupling is not straightforward at this stage. It is worth noting that the existence of the Y_{64} tesseral harmonic is short and precedes the onset of the sectoral oscillation.

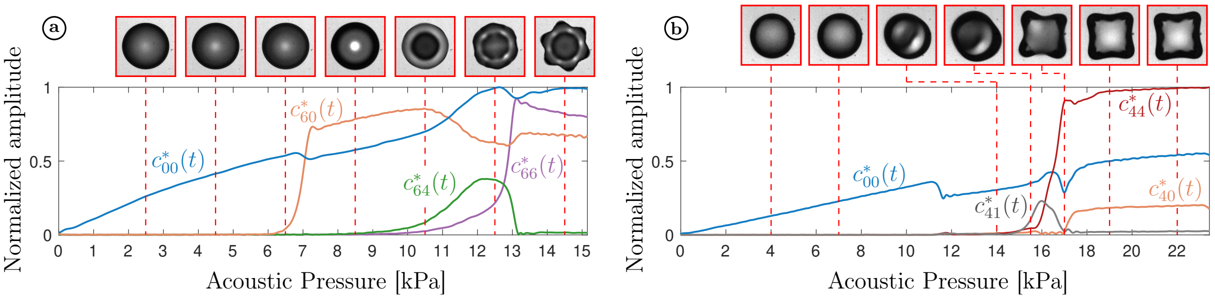

Figure 2.10: Evolution of the modal coefficients $c^*_{nm}(t)$ resulting from a top-view contour in the case of a bubble (a) with equilibrium radius $R_0 = 133$ µm oscillating on the set of $n = 6$ spherical harmonics and (b) with equilibrium radius $R_0 = 83$ µm oscillating on the set of $n = 4$ spherical harmonics. Only the predominant nonspherical modes are displayed. Snapshot series illustrate significant changes in bubble shape.

The bubble interface presented in figure 2.10b follows the successive vibration sequence $Y_{41} - Y_{44} - Y_{40}$ once nonspherical oscillations appear. The fact that the Y_{41} tesseral harmonic is the first mode to be triggered is clearly visible on the snapshot series. Once more, the existence of the tesseral harmonic is short and precedes the onset of both sectoral and zonal modes. By the way, figure 2.10b shows that both sectoral and zonal modes follow similar trends and reach a plateau value of oscillation amplitude.

Besides, pursuing the same line of experimental validation of the observed modes, appendix A.1 offers some visualizations and analysis of occasional side-view microbubbles. It comes supporting our interpretations and modal identifications asserted throughout this chapter.

2.2.4 Modal nondegeneracy

The analysis of the bubble vibration sequence has been performed over the whole data set of experimental wall-attached bubbles, leading to the determination of the onset of the first triggered nonspherical oscillation. These pressure thresholds are displayed in a pressure-radius map, for sub-resonant radii (degree $n = 3$ and $n = 4$) in figures 2.11a and 2.11b, for resonant radii (degree $n = 5$) in figure 2.11c and for over-resonant radii (degree $n = 7$) in figure 2.11d. Each geometrical marker is associated to a particular vibration sequence and indicates the pressure value at which the bubble interface diverges from the purely radial mode. In addition, the color range points out which nonspherical mode is firstly triggered.

In order to help in the figure readability, parabolic-like graphical fits have been drawn for each order-m mode, for $m = 0$ to $m = n$, and allow identifying their respective radius-related areas of bubble shape instability, the so-called resonance bands. For low degrees ($n = 3$ or 4), these resonance bands only slightly overlap. For higher degree ($n = 7$), despite a strong overlap, some orders m appear completely distinct. For resonant degree ($n = 5$), some resonance bands are completely overlapping ($m = 3$ and $m = 5$) and some others only partially ($m = 1$). Globally, for each investigated degree n, three distinct modal regions are found. In the vicinity of the nonspherical resonant radius of the equivalent free bubble (given on top of each sub-figure and corresponding to the radius at which a de gree n is parametrically-excited, see equation (1.11)), zonal and sectoral modes emerge preferentially. Far from this resonant radius, tesseral modes are most likely to show up firstly. We therefore distinguish the degree-n modal regions as a three-band zone, the tesseral-mode bands surrounding the zonal/sectoral ones. We can be confident in this result, since the frequency of the sectoral mode, compared to other nonspherical mode of a same modal subset of spherical harmonics, is the less likely to differ as a function of the equilibrium contact angle [Bostwick and Steen, 2014]. Contrariwise to the Lamb spectrum where every modes m of a same degree n have the same resonance frequency,

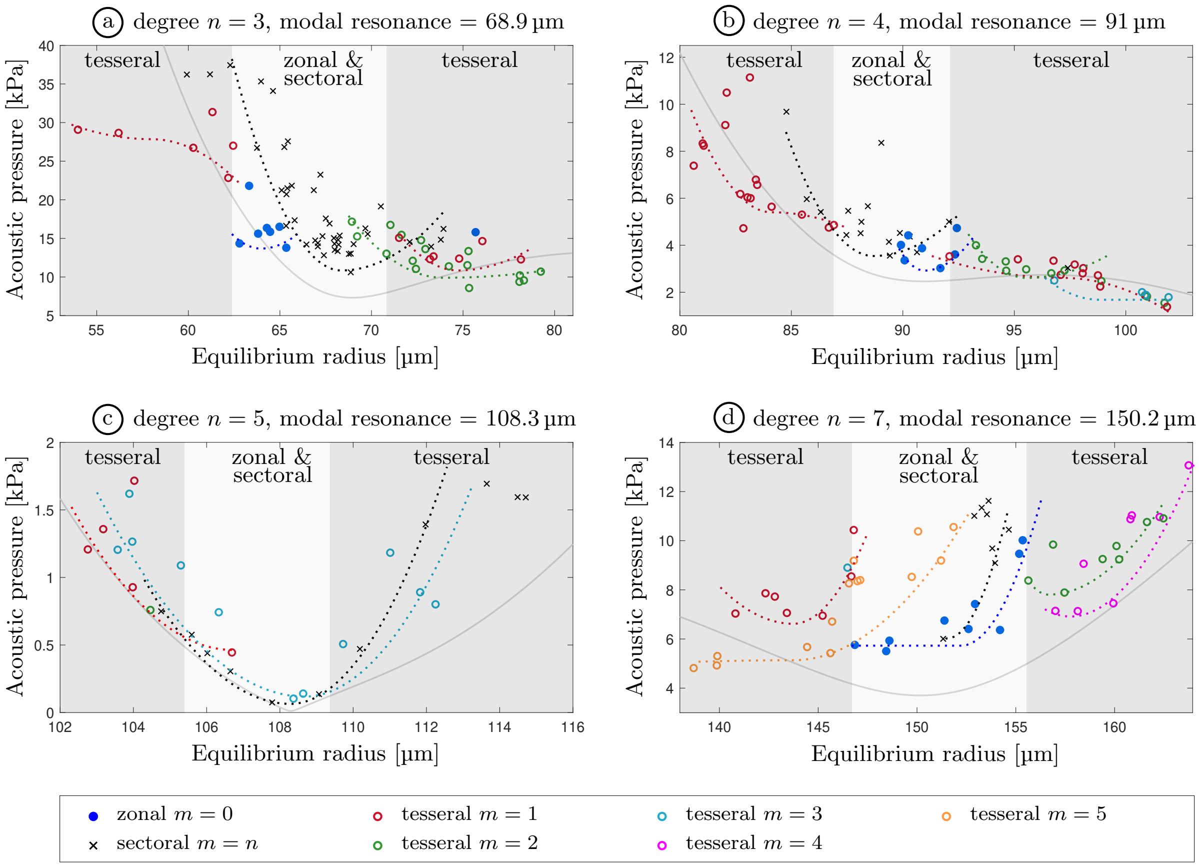

Figure 2.11: Instability pressure thresholds of the first triggered nonspherical shape modes of degree $n = 3$ (a), $n = 4$ (b), $n = 5$ (c) and $n = 7$ (d). Parabolic-like graphical fits (dashed lines) give an overview of the nondegenerate instability threshold curves. The solid gray lines are the theoretical instability curves of free axisymmetric bubbles [Francescutto and Nabergoj, 1978], centered on the respective modal resonances.

the experimental instability curves of figure 2.11 unveil resonant radius that are order-dependent. This evidences a modal nondegeneracy over the set of zonal, tesseral and sectoral modes. Such modal nondegeneracy has already been observed experimentally for vibrating sessile drops [Chang et al., 2013] and demonstrated theoretically for levitating drops with the appearance of $n+1$ modal regions for a given degree n of the parametrically-excited nonspherical mode [Suryanarayana and Bayazitoglu, 1991]. To our knowledge the modal nondegeneracy of bubble asymmetrical oscillations had not been demonstrated so far.

2.2.5 Occurrence of specific orders m

It is worth mentioning that asymmetric bubble shapes only arise from a break into the problem symmetry, usually caused by a geometrical singularity [Dollet et al., 2008] or by asymmetry in the external forcing [Versluis et al., 2010]. Moreover, which nonspherical mode is selected under external forcing for a given bubble radius has not been explained theoretically. In the present investigation, because of the pinning of the bubble on a substrate, specific nonspherical oscillations may encounter difficulties to be triggered, while other modes would experience the pinning as less inhibiting. At first glance, it is reasonable to suppose that a zonal mode, with a circular contact line shape and a possible nodal line matching the contact, is more inclined to emerge at low acoustic pressure. Concerning sectoral modes, the conditions of their emergence are less obvious as the contact line or angle are necessarily changing, if conform with the free bubble modal shapes. Nevertheless, the sectoral shape of a super-hemispherical wall-attached bubble would always encounter *weak* variations of contact line and angle with respect to the equilibrium state, as illustrated in figure 2.12. For the measured contact angle of $51° \pm 7°$, the associated Legendre polynomial $\mathrm{P}_{nm}[\cos\,\theta]$ responsible for the longitudinal shape of nonspherical modes present a slight deviation from the shape at rest, regardless the modal degree. On the contrary, tesseral modes could encounter much greater variations of contact line and angle. In view of figure 2.12, close to a contact angle of 51°, some of them have a nodal line matching the contact (Y_{41} or Y_{52}), while others should experience an extreme deformation from the situation at rest (Y_{43} or Y_{54}) in order to exist. This feature would strongly condition their respective emergence. This might explain why certain tesseral modes have never been observed in the present experimental setup, while others never miss to show up. By resuming to figure 2.11, we indeed note the recurring onset of tesseral modes Y_{41}, but in contrast to this theoretical hypothesis, not as often the tesseral mode Y_{52}. In fact, theoretically predicting the conditioning of the tethering on the appearance of the set of nonspherical modes of a wall-attached bubble would require more than an investigation of the truncated spherical harmonics, given that the contact line mobility, the variability of the contact angle at rest, the possible existence of vertical translation oscillation (hard to capture in a top-view configuration) or the kinetic energy required for the bubble interface to bend and adopt nonspherical deformations may all play a crucial role. Some of these lines of thought were taken to answer the question, but the analysis being multi-parametric and very hypothetical, we did not succeed in concluding properly on this point.

Substantial literature exists for the modal analysis of sessile drops [Bostwick and Steen, 2014, Chang et al., 2015, 2013, Courty et al., 2006, Shklyaev and Straube, 2008]. It has been demonstrated that the modal content of the nonspherical drop shape relies on the equilibrium contact angle and the contact line mobility [Bostwick and Steen, 2014]. At very high mobility, the contact line motion is facilitated while the instantaneous contact angle barely varies. The substrate-induced stress is less constraining. The dynamics of the system approaches the one of a free drop, displaying degenerate Lamb natural frequencies, as defined by equation (1.11). At low mobility, the contact line moves hardly and its dynamics is ensured by more extreme contact angles. Therefore this mobility

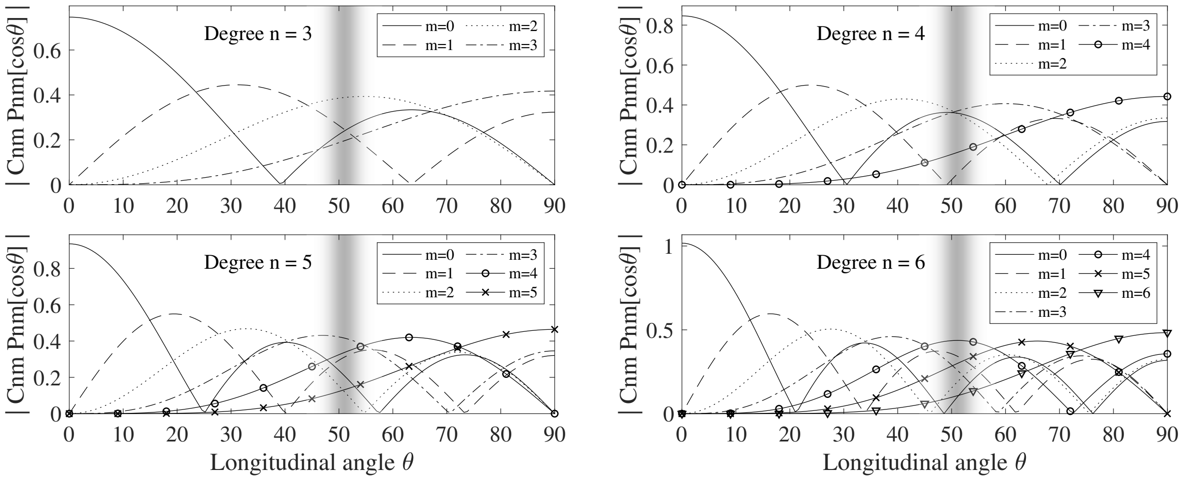

Figure 2.12: Normalized associated Legendre polynomials as a function of the longitudinal angle θ, for degrees $n = 3$ to $n = 6$. This corresponds to the maximal deformation of a free bubble interface with respect to its situation at rest. In other words, it illustrates the theoretical matching of nodal parallels of modal deformation with a no-mobility contact line of a bubble attached to a wall, as a function of the contact angle at rest α, that actually geometrically replicates the longitudinal angle θ.

limitation leads to stronger interface deformations, facilitating the onset of nonspherical shapes [Prosperetti, 2012]. As a consequence, a modal splitting is expected and has been experimentally observed [Bostwick and Steen, 2014]. Modal nondegeneracy is shown to occur when the equilibrium contact angle α differs significantly from 90°, in other words when the undisturbed drop shape is no longer hemispherical [Chang et al., 2015]. The degeneracy break yields to frequency reordering and modal crossing, responsible for coexistence between modes [Bostwick and Steen, 2014], and eventually for coupling between resonant modes. When regarding the investigated bubble with measured contact angle about $51° \pm 7°$, the undisturbed shape is far from being hemispherical. Similarly to the case of sessile drops, it favours the mode coupling (section 2.2.3), modal nondegeneracy (section 2.2.4 and figure 2.11) and coexistence (section 2.2.6 and figure 2.13).

In addition, it is shown that the resonance frequency of sectoral modes does not differ significantly from the one of zonal modes. Accordingly sectoral modes have been often reported because of their ease to emerge at low pressure amplitude. Recently, the contact line dynamics and mobility, and their impact on the onset of nonspherical modes have been modelled numerically for the case of a tethered bubble submitted to increasing acoustic pressure [Abramova et al., 2018]. Preferential triggering of the sectoral mode over the other nonspherical oscillations have been shown, but only in a qualitative way. From a theoretical point of view, Maksimov and Leighton [2012] derived the conditions of the emergence of specific shape mode patterns in order to clarify experimental observations of nonspherical bubble interface [Birkin et al., 2011]. The theoretical model relies on the Faraday wave analysis over the bubble interface, based on a triad resonant interaction between the radial mode and two shape modes. The preferential triggering of peculiar patterns called rolls (sectoral shape) and squares (combination of sectoral and zonal modes) is highlighted, but is limited to the case of high modal degree ($n > 9$).

2.2.6 Coexistence of zonal and sectoral modes

It is worth noting that the theoretical derivations of Maksimov and Leighton [2012] concern the emergence of specific patterns that are either the combination of zonal and sectoral harmonics, either a lone sectoral harmonic. In the present study, for bubble radii near the nonspherical resonant radius of a given degree n, we take advantage of the previously described spatiotemporal image processing method for mode differentiation in the aim of analysing the dynamics of zonal and sectoral modes.

Literature about a vibrating sessile drop reports two kinds of modal interaction: “mode mixing” and “mode competition” [Chang et al., 2015]. It is demonstrated that two modes are more inclined to hysteretically compete when their resonance bands intersect or when they are oscillating at the same harmonic frequency. Otherwise, they both display an unconstrained linear superposition of their respective dynamics. Contrarily to the present experiment, it should be pointed out that sessile drops are usually excited by a substrate-normal driving. This leads to the triggering of zonal modes oscillating at the fundamental frequency and to non-zonal modes exhibiting a subharmonic response. On the contrary, in the scope of our experimental wall-attached bubbles, every nonspherical modes developing on the interface are excited on their first parametric resonance, hence oscillating at half the driving frequency. In addition to the recurrent overlapping of the resonance frequency bands of zonal and sectoral modes (cf. figure 2.11), this suggests that “mode competition” would be more likely to occur if we refer to Chang et al. [2015].

However, figure 2.13 unveils dissimilarities in the modal interaction depending on the degree n, as described in the next two paragraphs through an original approach highlighting their modal dynamics, amplitude interplay and phase relation, and their geometric compatibility. The modal amplitudes and nonspherical deformations of the radial, zonal and sectoral modes are exposed for odd degree modes in figures 2.13a and 2.13b and for even degree modes in figures 2.13c and 2.13d. The normalized modal coefficients $c^*_{nm}(t)$ and $c_{nm}(t)$ are depicted respectively during a complete modulation period and during two acoustic periods. In addition, schematics of the bubble interface for each considered shape mode is provided.

In figures 2.13c and 2.13d where even degrees $n = 4$ and $n = 6$ are detailed, sectoral and zonal modes exhibit stable coexistence: Their modal oscillation amplitudes reach a plateau value without inhibiting each other. This corresponds to “mode mixing”, as their modal envelopes $c^*_{nk}(t)$ display an unconstrained linear superposition. This aspect is illustrated

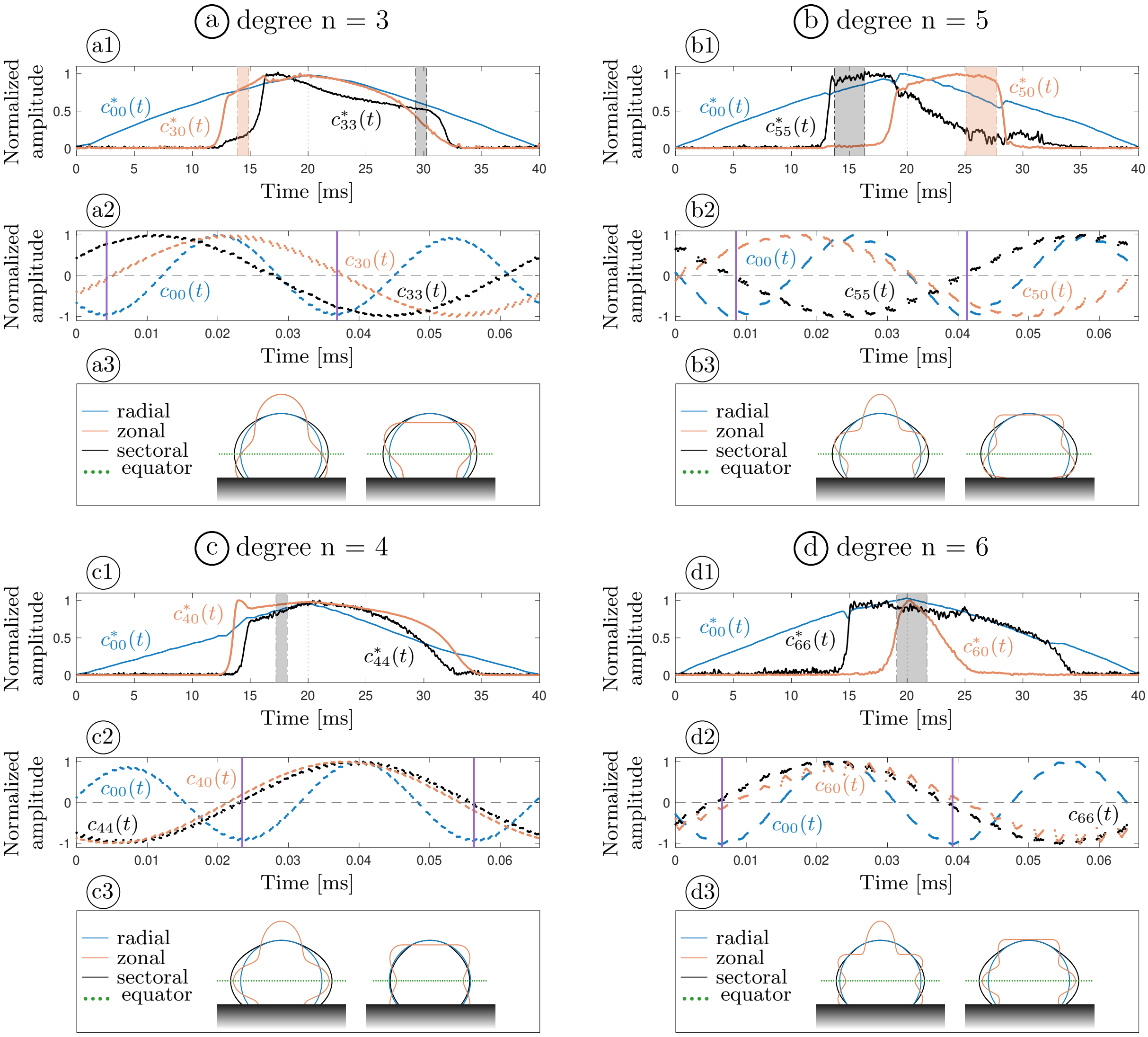

Figure 2.13: Coexistence of sectoral and zonal modes is exposed relying on their modal interplay, phase relation and symmetry compatibility for the cases of modes of odd degree $n = 3$ (a) and $n = 5$ (b) and even degree $n = 4$ (c) and $n = 6$ (d). For each case (x), the information is structured as follows. (x1) Evolution of the coefficients $c^*_{nm}(t)$ for the radial, zonal and sectoral modes along a complete modulation period; (x2) Evolution of the oscillatory behavior of the coefficients $c_{nm}(t)$ for the same modes, taken at particular times corresponding to colored areas in (x1) and refolded over two acoustic periods. vertical purple lines correspond to the instants where occur the minima of radial oscillation; (x3) Side-view schematics of the extrema of bubble deformations for the selected shape modes.

in figures 2.13c1 and 2.13d1. In addition, the observation of their dynamics reinforces this interpretation. Indeed, very interestingly, figures 2.13c2 and 2.13d2 reveal the obvious synchronization of the zero crossing of their respective nonspherical deformations with the minimum of the radial oscillation (graphically marked with vertical purple lines).

This probably happens as a way to minimize the magnitude of bending energy. As a consequence, it is also worth noting that zonal and sectoral modes oscillate then in-phase. As a matter of fact, both zonal and sectoral modes seem to synchronize independently with the radial mode, given that this occurs similarly when one of them is lonely triggered. Lastly, figures 2.13c3 and 2.13d3 depict side-view schematics of the corresponding bubble deformations. From a geometrical point of view, both zonal and sectoral deformations of even degree possess a vibration anti-node at the equatorial plane of the bubble, which could explain their propensity to coexist.

In contrast, in figures 2.13a1 and 2.13b1, it appears that zonal and sectoral modes of odd degree $n = 3$ and $n = 5$ go up against each other. The onset of the secondly-triggered mode seems to coincide with the fading of the first one, as it is clearly visible in the case $n = 5$. This corresponds to “mode competition”, as their modal interaction is characterized by the domination of some mode and by a challenging coexistence. The first triggered nonspherical shape modes, zonal of degree $n = 3$ coded in orange in figure 2.13a and sectoral of degree $n = 5$ coded in black in figure 2.13b, are spontaneously privileged and show similar behavior, namely the synchronization of the zero crossing of their nonspherical deformations with the minimum of the radial oscillation (graphically marked with vertical purple lines). The secondly triggered nonspherical shape modes, sectoral of degree $n = 3$ coded in black in figure 2.13a and zonal of degree $n = 5$ coded in orange in figure 2.13b, arrive later. They never encounter a possibility to oscillate in-phase with the first triggered modes and favour a synchronization of their zero crossing of nonspherical deformations with a zero crossing of the radial oscillation. Still from a geometrical point of view, as schematized in figures 2.13a3 and 2.13b3 for this odd degree case, the equatorial plane corresponds to a vibration anti-node of the sectoral mode but to a vibration node of the zonal shape. Hence both sectoral and zonal modes undergo conflicting shapes. This could explain why modal competition occurs and why they never exhibit an in-phase behavior.

However this does not explain their specific and recurrent phase-locking relation, or determine how coupling operates, or even justify the legitimacy for one mode to dominate another. Explaining the modal coexistence would most likely involve a multi-parameter study, and not just an investigation of the shape compatibility, the contact line or the phase relation. In definitive, it would be worth investigating whether the phase relation is rather governed by a minimization of the energy cost occurring at the contact. Such an analysis would require access to the contact line dynamics and mobility, as well as to both the macroscopic and the microscopic behaviors near the contact of a wall-attached bubble excited upon nonspherical shape modes. So far, these remain experimentally very difficult to obtain. Nevertheless, we are confident in saying that the phase relation between zonal and sectoral modes is essential for their coexistence as a means of minimizing in some way their energy cost.

2.3 Conclusion

In the absence of any consistent theoretical model for the dynamics of an ultrasound-excited wall-attached bubble and the triggering of its surface instability, we proposed an experimental study with the aim of investigating the modal behavior of such a bubble under an acoustic excitation of increasing pressure. The vibration sequence of a bubble oscillating upon nonspherical shape deformations is obtained from a spatiotemporal analysis of its top-view contour. The differentiation of any nonspherical shape modes led to the mapping of their pressure instability threshold as a function of the bubble size. This revealed for the first time that the frequencies of asymmetric modes differ from the standard Lamb spectrum. This feature referred as nondegeneracy of the set of nonspherical shape modes of a wall-attached bubble is evidenced by non-completely overlapping resonance bands. More exactly, a three-band zone of modal resonances stand out, with a preferential triggering of sectoral and zonal modes around the free bubble resonant radius and a triggering of tesseral modes further than this resonant radius. In addition, an original investigation of the coexistence between zonal and sectoral modes explores their modal interaction in terms of their amplitude interplay, phase relation, degree parity and geometric compatibility. Similarly to sessile drops but, in the present study, observed for the case of a wall-attached bubble, two kinds of modal interaction behavior are reported: Sectoral and zonal modes of even degree $n = 4$ and $n = 6$ show ease of coexistence and preferential “mode mixing”, while sectoral and zonal modes of odd degree $n = 3$ and $n = 5$ present greater difficulties to exist simultaneously, given that important “mode competition” occurs.

Now that the dynamics of nonspherical bubbles is better controlled and understood, our experimental investigation continues in chapter 3 with its induced effects on the surrounding fluid and the formation of microstreaming patterns. The correlation of these fluid flows with the bubble activity will require a better knowledge of its modal content, while it was only investigated in this chapter 2 in a rather qualitative way. To this end, an extension of our modal analysis tool will be hence described, allowing discussing the influence of modal amplitudes and phase shift on the induced streaming, the fluid’s patterns and velocity.

Chapter 3

Acoustic microstreaming

Now strengthened with the ability to detect and identify the asymmetric modes of a wall-attached bubble, this third chapter focuses on the characterization and the differentiation of its induced microstreaming. Our experimental method described in section 3.1 allows the capture and the exploration of particular flow signatures for the main classes of spherical harmonics. Because the streaming formation can be explained by the bubble modal content, a more accurate and quantified knowledge of the involved modes, their amplitude and phase shift, is crucial. The detail of our modal calculation is progressively given throughout the five main experimental cases investigated in section 3.2: the "zonal mode only" case (3.2.1), the "sectoral mode only" case (3.2.2), the "tesseral mode only" case (3.2.3), the "sectoral and zonal modes combo" case (3.2.4) and the "sectoral and tesseral modes combo" case (3.2.5). A deeper analysis by particle tracking velocimetry (PTV) method of the specific case of zonal and sectoral modes allowed to discuss and explain the preferential appearance of specific streaming signatures.

In literature, the bubble-induced microstreaming is usually explored for the case of axisymmetric modes. When asymmetric modes are encountered, the bubble dynamics is clearly neglected, while it may actually play an important role. As a consequence, this chapter draws the main lines of what could be the first depictions and evidences of the experimental microstreaming produced by asymmetric modes of a tethered bubble, reinforced and interpreted by their quantified time-resolved dynamics.

3.1 Methodology

3.1.1 Experimental setup

Figure 3.1 depicts a schematic of the experimental setup, which barely differs from the setup employed for the visualization of the dynamics of nonspherical shape modes. Pure

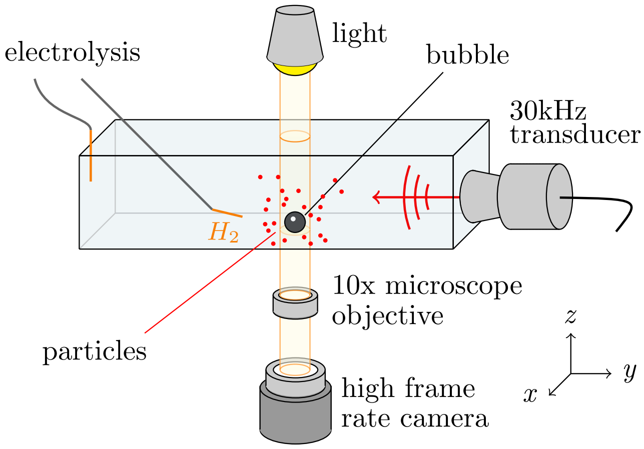

Figure 3.1: Schematic representation of the experimental setup.

water still fills the tank with the difference that tracking particles are appended to the solution, with the aim of monitoring the fluid motion generated by the bubble oscillation. First unsuccessful attempts were done using polyamid micro-spheres (Dantec Dynamics A/S, Polyamid Seeding Particles 5 µm ⌀), but their constant inclination for sticking to the bubble interface made their replacement inexorable. The bubble was then so constrained that a stable oscillation and the triggering of nonspherical shape modes were particularly difficult to reach. At relatively high acoustic pressure, where we should have already observed the emergence of nonspherical modes, the bubble was barely oscillating radially and the particles came to stick the bubble. Then, after rising considerably the acoustic pressure, the particles suddenly detached from the interface and began to swirl all around a very unstable bubble until its collapse or an adjustment of the pressure and the return to the first situation. Quickly, we moved to different particles, fluorescent red beads made of polystyrene (Fisher ThermoScientific, Fluoro-max red beads 3 µm ⌀). Fluorescent and thus originally built to be lighted by a laser source, we were here visualizing them in a simple optical manner under the microscope white light. This configuration turned out to be functional. In addition, we are confident in the ability of these tracking particles to follow with closeness and fidelity the global fluid motion, since their Stokes number [Tropea et al., 2007] St is much smaller than 0.1,

$$\mathrm{St} \propto \frac{d_p|\rho_p - \rho_f|v_{\max}}{\mu} \simeq 6.2 \times 10^{-3} \ll 1, \tag{3.1}$$

where $\rho_f \simeq 0.998 \times 10^3\,\mathrm{kg \cdot m^{-3}}$ is the density of Milli-Q water (at 20 °C), $\rho_p \simeq 1.05 \times 10^3\,\mathrm{kg \cdot m^{-3}}$ is the density of particles, $d_p \simeq 3\,\mu\mathrm{m}$ their equivalent mean diameter, $\mu \simeq 1\,\mathrm{mPa \cdot s}$ the dynamic viscosity of water and $v_{\max} \simeq 40\,\mathrm{mm \cdot s^{-1}}$ the approximated maximal velocity of streaming. Because a bubble stable oscillation is required for the observation of microstreaming, a continuous sine wave of frequency 30.5 kHz without modulation in amplitude is employed for driving the bubble. Provided that the bubble dynamics is then stable at constant acoustic pressure, video of steady fluid motion could be recorded for a few seconds, which is a sufficient duration to get the full trajectory of particles.

3.1.2 Experimental procedure

Since the bubble interface displacement and the fluid motion happen at different time scales, the camera records alternatively two video sequences with different acquisition parameters (frame size, frame rate and exposure time), summarized in table 3.1. More precisely, the experiments are conducted through five steps :

1. The bubble is nucleated by electrolysis and positioned in the optical path.
2. The triggering of nonspherical shape modes is achieved by rising gradually the output voltage of the signal generator.
3. The streaming around the bubble is captured.
4. Instantly after, the bubble dynamics is captured at a higher frame rate.
5. Finally, a snapshot of the bubble is taken at rest in order to obtain its equilibrium radius R_0.

	Frame size	**Frame rate**	**Exposure time**
Microstreaming	512 x 512 pixels	2k images/s	2 µs
Bubble dynamics	256 x 256 pixels	67k images/s	2 µs

Table 3.1: Acquisition parameters (frame size, frame rate and exposure time) as set in the software Phantom Camera Control (PCC).

3.1.3 Data post-processing

Streamlines overlay

In order to obtain a global overview of the fluid motion, all images of a video sequence are overlaid. More exactly, the resulting image is obtained by retaining for each pixel of the 512 by 512 pixels frame the minimal value among all images contained in the whole video sequence. This evidences the trajectories taken by particles. Although this method of representing fluid motion is limited to the recognition of streaming patterns, a quantitative approach is necessary whether the objective is to distinguish variations within a same sort of pattern. Throughout this chapter, velocity measurements will be especially employed in section 3.2.4, which concerns the modal interaction between zonal and sectoral modes, in order to explain the preferential formation of specific patterns. To this end, the post-processing method is explained hereafter.

Particle Tracking Velocimetry

For knowing the field of particles velocity, we performed a particle tracking velocimetry (PTV) analysis on the streamlines thanks to the Fiji software [Schindelin et al., 2012] and the plugin Trackmate [Tinevez et al., 2017]. An example is given in figure 3.2 for the case of a bubble undergoing simultaneously a sectoral mode and a zonal mode of degree $n = 3$. The result is obtained through the followings steps and parameters. The analysis is performed on 2000 images (1 s duration video) inverted so that the background is black and the bubble contour and particles are white. For the particles detection, the `Laplacian of Gaussian` filter is selected, with an `estimated blob diameter` of 5 µm and a `threshold` at 180. This quality threshold may need some adjustments, depending on the ability of particles to distinguish themselves from the possibly noisy background. After that, a filter of light `total intensity` on the detected spots is set so that the misleading bright spots detected on the bubble interface are discarded. Finally, the `linear motion tracker` (with parameters `initial search radius` = 40 µm and `search radius` = 10 µm) is employed to follow the particles trajectory and to estimate their velocity.

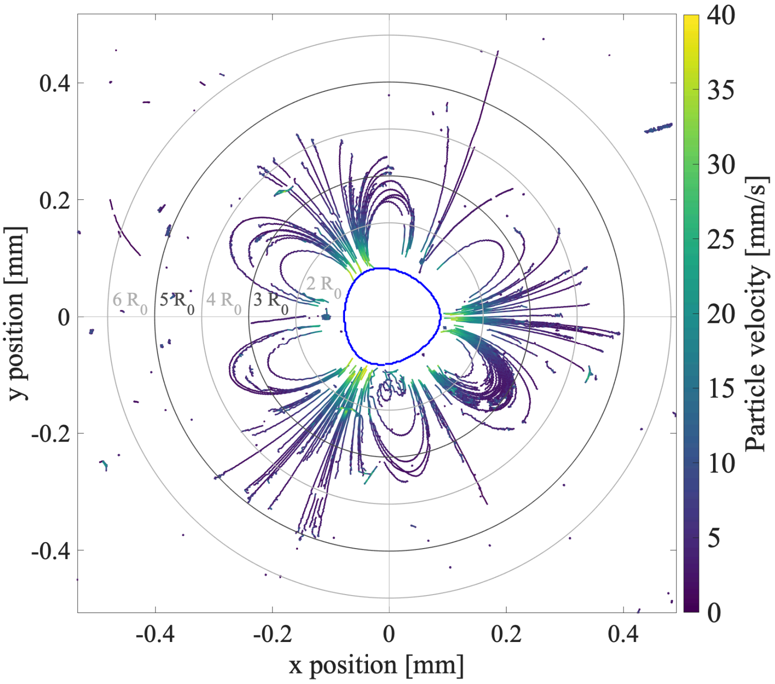

Figure 3.2: Typical result of the particle tracking velocimetry (PTV) analysis of the streaming induced by a bubble undergoing a sectoral and a zonal mode of degree $n = 3$.

The exportation of data into Matlab allows their detailed inspection with respect to a polar coordinates system referred to the center of the bubble, as well as the comparison of their maximal radial (outward) streaming velocities at an arbitrarily chosen distance of twice the equilibrium radius. For a modal degree n, n profiles of velocity are extracted from the n areas of propelled particles. For instance, in figure 3.2, there a 3 areas of propelled particles around the azimuthal angle $\phi = 0$, $\phi = 2\pi/3$ and $\phi = 4\pi/3$, where ϕ is defined from the positive x-axis. Lastly, a mean velocity profile is calculated, and the median value in the approximate distance range $[1.9R_0\ 2.1R_0]$ is retained.

3.2 Microstreaming induced by the main classes of spherical harmonics

This section gathers the scenarios of microstreaming we experienced for our tethered bubbles. Every streaming patterns are resulting from bubbles parametrically excited on their first resonance and exhibiting therefore nonspherical subharmonic behavior. As a consequence, no streaming can result from the interaction between a nonspherical shape mode and the radial oscillation, which occurs at the driving frequency [Cleve et al., 2019]. For the bubbles investigated here with equilibrium radius in the range [60 140] µm and acoustically driven at 30.5 kHz, modes of degree $n = 3$ to 6 are observable, as expected by the theoretical predictions on free bubbles [Francescutto and Nabergoj, 1978] and the results obtained in chapter 2 and figure 2.7. Since the formation of streaming can be explained from the bubble modal content, the phase shift between interacting modes and their respective amplitude [Longuet-Higgins, 1998, Marmottant and Hilgenfeldt, 2003], a quantitative modal description is necessary. Generally speaking, a nonspherical mode of degree n and order m has $n - m$ parallel nodal lines and $2m$ meridian nodal lines. With a single experimental top-view, the characterization of nonspherical modes can therefore struggle as soon as the bubble interface contains any mode such as $n \neq m$ and that nodal parallels appear. Since there exists no analytic solution for the projection in the (x,y) plane, the quantification of the amplitudes of any arbitrary asymmetric oscillation from a single top-view becomes challenging. We suggest here alternative methods for approaching the time-resolved amplitudes of nonspherical modes, associated to each of these experimental cases: zonal mode only, sectoral mode only, tesseral mode only, sectoral-zonal modes combo and sectoral-tesseral modes combo. These five cases represent the majority of cases encountered experimentally.

3.2.1 The “zonal mode only” case

Zonal modes are widely studied in literature because of their ease to be triggered experimentally for the case of free bubbles, and because of their comfortable axisymmetric shape that facilitates their mathematical study [Spelman and Lauga, 2017, Doinikov et al., 2019a,b, Inserra et al., 2020a,b]. The experimental visualization of their axisymmetric dynamics and associated streaming is usually performed from a side-view in a plane containing the bubble symmetry axis z. The orientation of a free bubble axisymmetric deformation is strongly influenced by the geometry of the system under study, the presence or not of a boundary, or even the existence of an asymmetric forcing on the bubble interface. In the absence of a wall, the assurance of the positioning of the symmetry axis within the imaging focal plane can be ensured experimentally by controlling the direction of impact of two coalescing bubbles [Cleve et al., 2019]. In that configuration of free axisymmetric bubble, the theoretical predictions of streaming are solved [Inserra et al., 2020a] and an example for the case of a self-interacting zonal mode of degree $n = 4$ is given in figure 3.3d. This microstreaming pattern is characterized by $2n$ vortices that develop in (r,θ) and show no dependency in azimuth.

When the bubble is attached to a wall, the orientation of the nonspherical bubble is also governed by the system geometry and gives a preference for the zonal mode deformation to develop following the symmetry axis z directed along the normal to the wall surface.

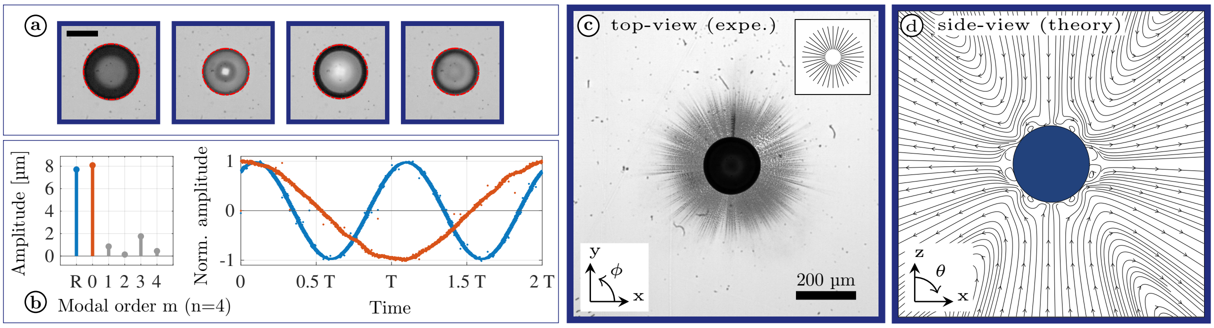

Figure 3.3: Modal analysis and associated microstreaming pattern of a microbubble of equilibrium radius 84.3 µm oscillating on a zonal mode of degree $n = 4$. The information is structured as follows. (a) Snapshot series of the top-view contour display the microbubble at different instants along a complete subharmonic period of duration $2/f_0$. The scale bar equals 100 µm. The red contour is a numerical reconstruction issued from the processed modal amplitudes displayed in (b). (b) Left: spectrum of the excited modes $n = 4$, ’R’ standing for the radial oscillation ($m = n = 0$), and right: temporal evolution of the normalized amplitudes of the predominant radial and zonal oscillations. (c) The associated microstreaming pattern. (d) Theoretical prediction of the side-view microstreaming induced by the self-interaction of a zonal axisymmetric mode of degree $n = 4$, issued by Inserra et al. [2020a].

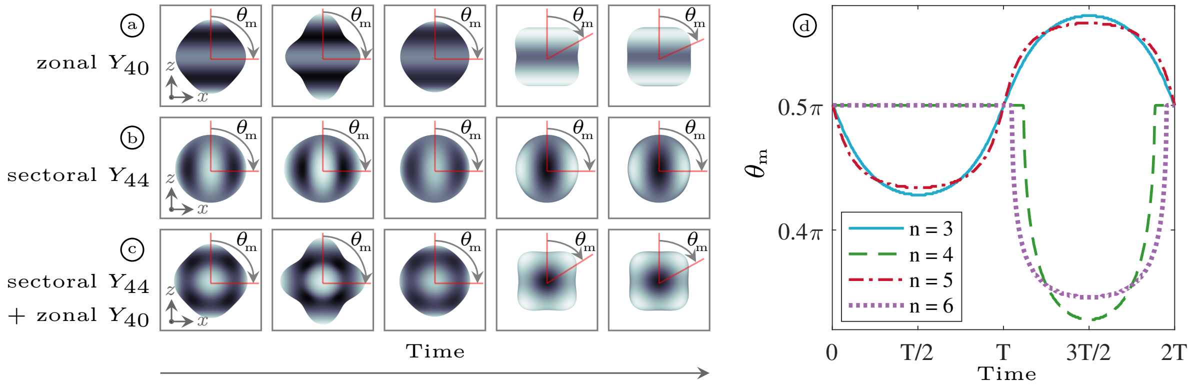

Figure 3.4: Side-views of a numerical bubble of equilibrium radius $R_0 = 90\,\mu\text{m}$ oscillating on a zonal mode Y_{40} of amplitude $a_{40} = 30\,\mu\text{m}$ (a), a sectoral mode Y_{44} of amplitude $a_{44} = 30\,\mu\text{m}$ (b) and the combination of both modes (c). The represented angle θ_m is the longitudinal angle for which the bubble contour projection in the (x,y) plane is maximal. (d) The temporal evolution of θ_m is observed along a complete subharmonic period for a zonal mode of degrees $n = 3$ to $n = 6$, with a zonal amplitude $a_{n0} = 0.3R_0$.

As a consequence, from a top-view perspective, the bubble oscillates with a misleading spherical appearance and the microstreaming looks exclusively radial, since there exists no azimuthal dependence and that the axisymmetric vortices are imperceptible, as illustrated in figure 3.3a and 3.3c. In a general way, differentiating several microstreaming scenarios and characterizing their motion strength require a good approach of the bubble modal content, especially when more than one nonspherical mode exist. In the framework of our microstreaming investigation, the amplitude of zonal modes is determined as follows. As a reminder, a bubble animated by a zonal mode only $(m = 0 < n)$ presents an oscillating shape devoid of nodal meridian. As a result, the top-view bubble's silhouette is circular at anytime, and measuring its amplitude is not straightforward. In addition, the longitudinal angle θ responsible for the top-view bubble's silhouette $s(\phi, t) = r(\theta_m, \phi, t)$ is not constant along a subharmonic period, as illustrated in figure 3.4a. This longitudinal angle, referred as θ_m in this study, varies with time as shown in figure 3.4d for cases of zonal modes of degree $n = 3$ to $n = 6$. It oscillates around the equilibrium value $\frac{\pi}{2}$ with a signature that is specific to the modal degree n and especially its parity. In other words, this angle $\theta_m(t)$ corresponds to the global maximum $r(\theta, \phi, t) \cdot \sin\theta$. Given that, the amplitude $a_{n0}(t)$ of the zonal mode can be approximated by decomposing the top-view bubble's silhouette $s(\phi, t)$ on the spherical harmonic Y_{n0},

$$a_{n0}(t) = \frac{\gamma_{n0}}{2\pi} \int_0^{2\pi} s(\phi, t)\; d\phi, \tag{3.2}$$

where $\gamma_{n0} = \left(f_{n0} P_{n0}^* \sin\theta_m^* \, \frac{s^*(\phi,t)}{R_0 + \tilde{a}_{n0} f_{n0} P_{n0}^*} \right)^{-1}$, with $\theta_m^* = \max(\theta_m)$, P_{n0}^* is the local maximum of the associated Legendre Polynomial $P_{n0}(\cos\theta)$ that is the nearest to θ_m,

$\tilde{a}_{n0} = \frac{1}{2T}\int_0^{2T}\frac{1}{2\pi}\int_0^{2\pi} s(\phi,t)\ \ e^{-i\pi f_0 t}\ d\phi\ dt$ and $s^*(\phi,t)$ is the maximal value reached by the bubble silhouette $s(\phi,t)$. This allows to approach the amplitude of the zonal mode. In the experimental case illustrated in figure 3.3, the amplitude of the zonal mode is of the same order of magnitude than the amplitude of the radial oscillation, as detailed by the spectrum of the excited modes of figure 3.3b. It goes along with the temporal evolution of the predominant radial and zonal oscillations refolded over two acoustic periods and expressed in normalized amplitudes. A numerical bubble is implemented from the experimental data issued by this modal decomposition and its top-view contour is drawn in dashed red lines on the experimental snapshots of figure 3.3a. This experimental bubble corresponds to a similar case of zonal harmonics $n = 4$ than the theoretical case displayed in figure 3.3d. Even if, we cannot observe the axisymmetric recirculation loops in our top-view configuration, we can discern in the experimental video sequence that particles get regularly blurry as they move around the bubble, which confirms that particles come out and in the focal plane and that there does exist a dependence in elevation, such as figure 3.3d demonstrates.

3.2.2 The “sectoral mode only” case

Sectoral modes have as much azimuthal deformation lobes as the modal degree n they belong to. Strictly speaking, they have $2n$ anti-nodes and $2n$ nodes of interface displacement along the azimuthal coordinate. Because the number of nodal parallels of any spherical harmonics equals $n - m$, sectoral modes ($n = m$) are devoid of it and have their only longitudinal displacement anti-node at the equator, as illustrated in figure 3.4b, where they exhibit an azimuthal shape that corresponds to a $\cos(m\phi)$. This azimuthal shape is easily recognizable from a top-view observation, as shown in figure 3.5a and figure 3.5d for bubbles oscillating on a sectoral mode $n = 3$ and $n = 4$, respectively. The bubble's silhouette $s(\phi,t)$ from a top-view exactly equals the bubble interface $r(\theta,\phi,t)$ at $\theta = \frac{\pi}{2}$,

$$s(\phi,t) = r(\frac{\pi}{2},\phi,t) = R_0 + a_{00}(t) + a_{nn}(t) f_{nn} P_{nn}[0] e^{im\phi}. \tag{3.3}$$

By decomposing the top-view bubble's silhouette $s(\phi,t)$ on the spherical harmonic Y_{nn}, the amplitude $a_{nn}(t)$ of the sectoral mode is calculated as follows

$$a_{nn}(t) = \frac{\gamma_{nn}}{2\pi}\int_0^{2\pi} s(\phi,t) e^{-im\phi}\ d\phi, \tag{3.4}$$

where $\gamma_{nn} = \Big(f_{nn}P_{nn}[0]\Big)^{-1}$. When performing this modal decomposition on an experimental bubble animated by a sectoral mode $n = 3$, it results what is depicted in figure 3.5b. The sectoral oscillation is three times greater than the radial one and reaches an amplitude of 15 µm.

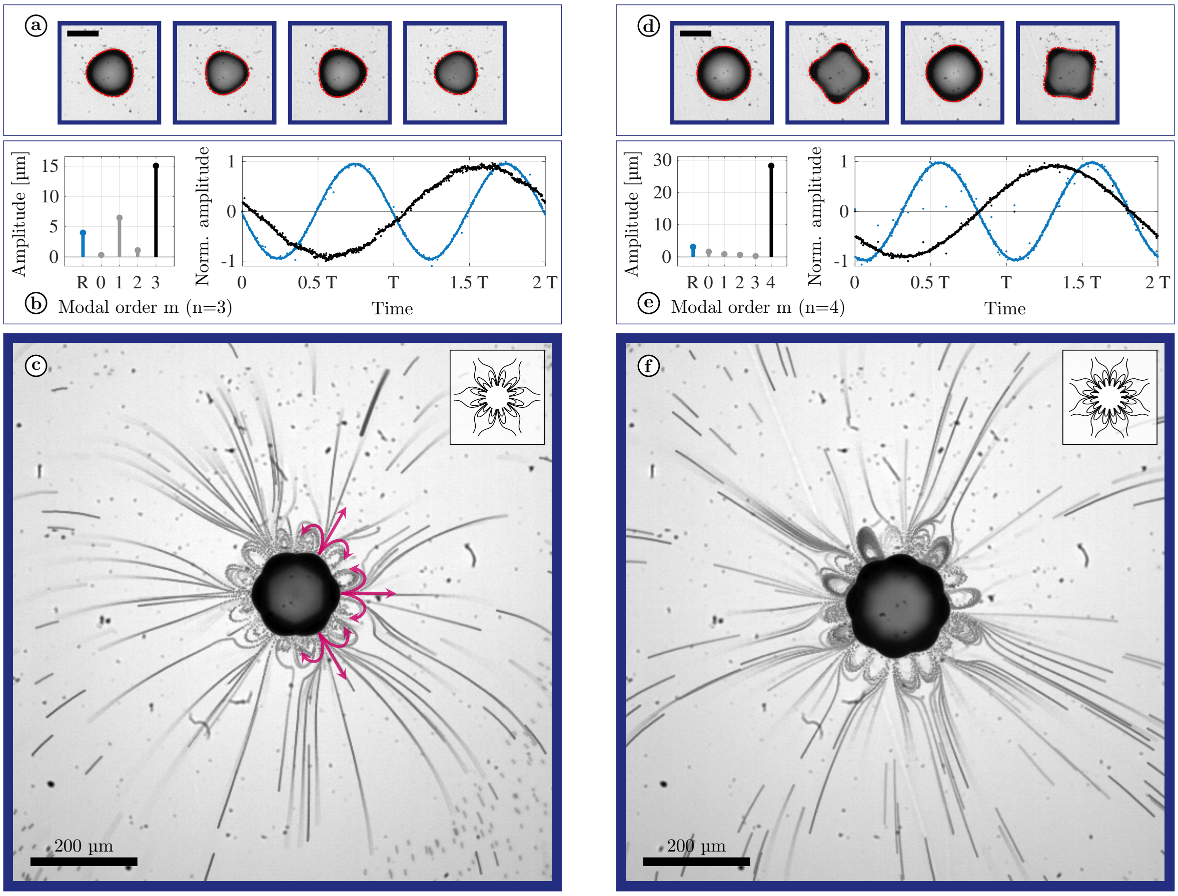

Figure 3.5: Modal analysis and associated microstreaming pattern of a microbubble of equilibrium radius 73.8 µm oscillating on a sectoral mode $n = 3$ (left) and a microbubble of equilibrium radius 88 µm oscillating on a sectoral mode $n = 4$ (right). The information is similarly structured as in figure 3.3.

When a bubble is animated by a sectoral mode only, the single azimuthal streaming contribution that may exist in our configuration is due to the interaction of the sectoral mode with itself. It generates a streaming pattern that has a $4n$-lobe flower shape, where lobes are assembled by pair. The same streaming signature is obtained in figure 3.5f in the case of a sectoral mode $n = 4$. The pattern displays 16 lobes that are also arranged by pair. It should also be mentioned that, in both cases, the rotational direction of the flow is such as to propel the particles away from the anti-nodes and to attract them back towards the nodes of displacement of the bubble interface. Each pair of recirculation loops is thus surrounded by areas of particles propelled with a positive radial velocity. This motion behavior is outlined with red arrows in figure 3.5c. Similar streaming signatures are also obtained for cases of sectoral modes of degree $n = 5$ and $n = 6$, illustrated in figure 3.6.

According to our knowledge of microstreaming patterns induced by axisymmetric modes, these general observations can be interpreted as follows. The bubble interface

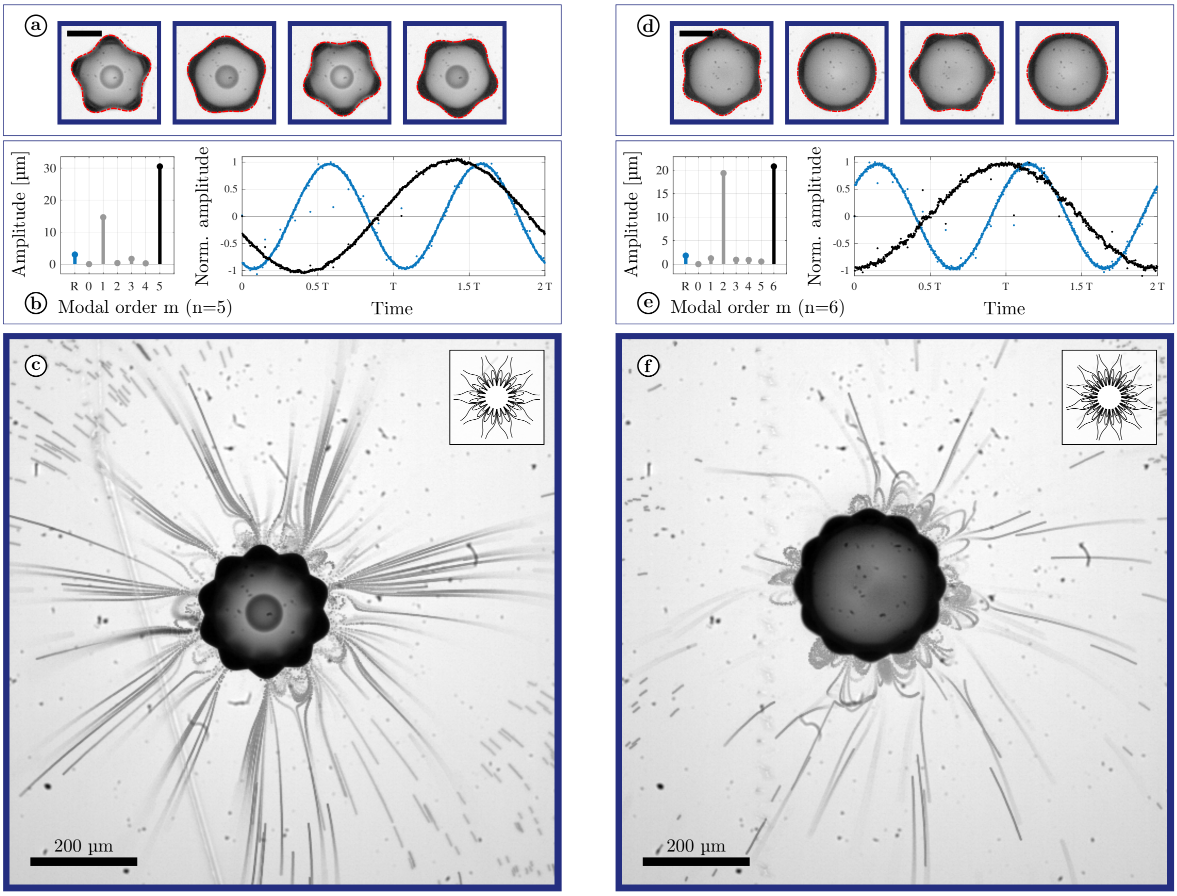

Figure 3.6: Modal analysis and associated microstreaming pattern of a microbubble of equilibrium radius 107.7 µm oscillating on a sectoral mode $n = 5$ (left) and a microbubble of equilibrium radius 132.1 µm oscillating on a sectoral mode $n = 6$ (right). The information is similarly structured as in figure 3.3.

motion of a sectoral mode from a top-view reminds the interface motion of an axisymmetric mode of same degree visualized from a side-view : They both present the same number of nodal lines, in elevation for axisymmetric modes, and in azimuth for sectoral modes. In conclusion, it could be argued that, just like the self-interaction of an axisymmetric mode of degree n presents $4n$ lobes of streaming around the bubble [Inserra et al., 2020a], a bubble exclusively animated by a sectoral mode generates a streaming signature as a $4n$-lobe flower shape.

It is worth noting that in the case of odd-order modes, an important misleading non-zero amplitude associated to a mode of order $m = 1$ usually appears (see figures 3.5b and 3.6b). This has been numerically confirmed to be an artefact issued from our calculation method of the biased bubble two-dimensional projection. The evidence is given in figure 3.7 following a two-step procedure of analysis. First, figure 3.7a presents the result of our algorithm of modal analysis applied to an experimental bubble, letting appear a

ⓐ Modal analysis of an experimental bubble undergoing a sectoral mode $n = 5$

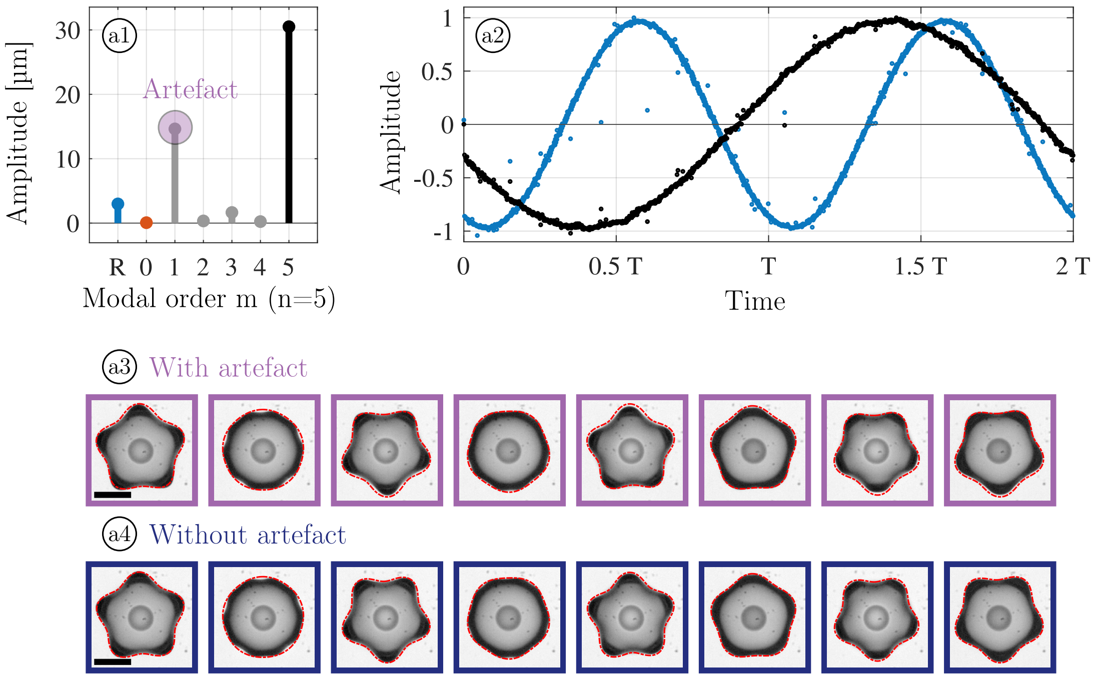

ⓑ Equivalent numerical bubble implemented without artefact

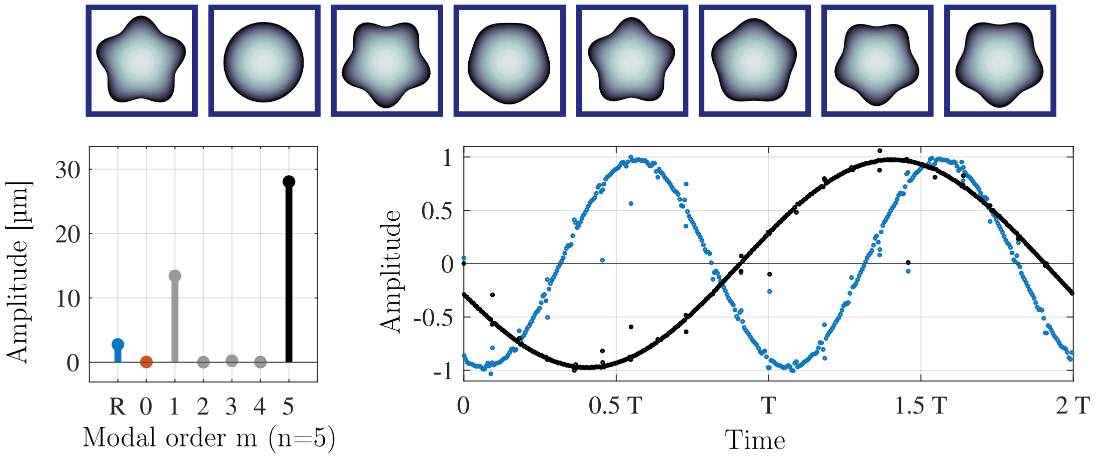

Figure 3.7: Demonstration of the appearance of an unwanted artefact in the modal analysis of odd m-order modes, here applied to a bubble of radius 107.7 µm oscillating on a sectoral mode of degree $n = 5$ (same bubble as in figure 3.6). The appearance of a $m = 1$ modal component in the spectrum (a1) is first qualitatively confirmed as artefact thanks to the superimposition of an equivalent numerical bubble contour on the experimental snapshots with (a3) and without (a4) considering the presumed artefact in its implementation. The scale bars equal 100 µm. The modal analysis with the exact same algorithm of a numerical bubble implemented without the presumed artefact (b) makes the $m = 1$ modal component reappear, quantitatively confirming their existence as artefact only.

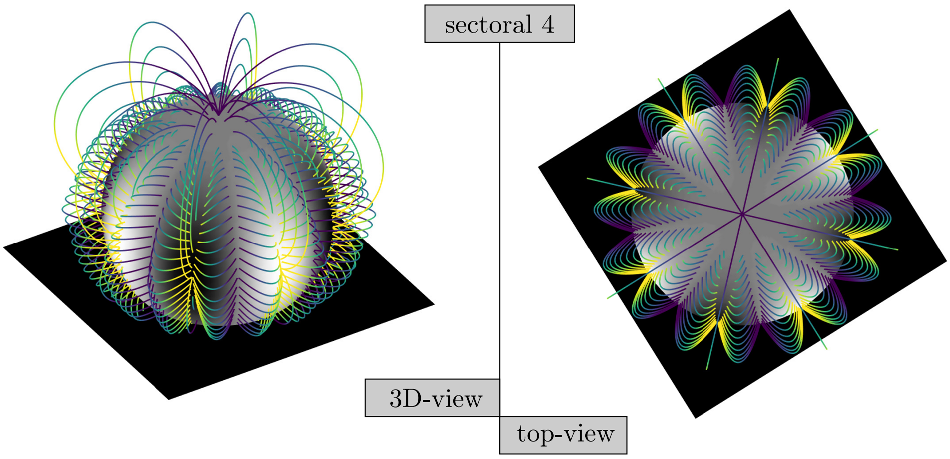

Figure 3.8: Artist's view of the microstreaming induced by a bubble oscillating on a sectoral mode of degree $n = 4$, represented from a three-dimensional perspective (left) and from a top-view (right). The color map relates to the derivative of the fluid displacement with respect to the radial coordinate, from dark to light shades for streamlines having negative to positive radial velocities.

sectoral mode $n = 5$ of amplitude 30 µm, but also, a presumed artefact (a tesseral mode $m = 1$) of amplitude 15 µm. In a second stage, the exact same algorithm is applied to a numerical bubble implemented without the presumed artefact. It turns out that an artefact (still a tesseral mode $m = 1$) of same amplitude reappears (see figure 3.7b). It therefore demonstrates that this misleading non-zero amplitude was indeed an artefact. This affirmation is also reinforced by analyzing the oscillatory dynamics of the misleading tesseral mode. Indeed, its oscillatory characteristics (onset, dynamics, inter-modal phase and extinction) exactly match the ones of the predominantly investigated sectoral mode. All these dynamical similarities never occur when a tesseral mode is truly existent.

In elevation, sectoral modes are characterized by displacement nodes at the poles and displacement anti-nodes at the equator, resembling therefore from a side-view to a dipole mode. Such motion is often reported in works investigating acoustic streaming, whether it concerns a free bubble [Longuet-Higgins, 1998, Davidson and Riley, 1971, Doinikov et al., 2019b] or a tethered one [Tho et al., 2007, Collis et al., 2010]. The associated streaming pattern is characterized by the presence of antifountain-like vortices in elevation at the poles of the bubble. As qualitatively sketched in figure 3.8, such an antifountain-like pattern could be expected in elevation around a bubble animated by a sectoral mode, though certainly marked by a symmetry break in the lower hemisphere due to the presence of the wall. This may be an important difference with zonal modes, which, unlike sectoral modes, possess an anti-node of displacement at their north pole. We will further discuss this in appendix A.2, in which a complete aside is made on the streaming visualized from a lateral perspective. Emphasis is placed on the comparison between zonal and sectoral modes, and their very opposite induced fluid flow. In what concerns us for the moment, it is expected that important fluid flows develop in both azimuth and elevation dimensions due to the sectoral oscillation, even though only the azimuthal part of the particles motion located at the equator is clearly visible from our experimental top-view.

At last, because of a greater modal density of higher degree modes, the occurrence of sectoral modes only becomes scarcer when the bubble equilibrium radius and the associated modal degree increase. As a consequence, experimental occurrences of stable sectoral modes alone were less obvious for modal degrees higher than $n = 6$.

3.2.3 The “tesseral mode only” case

We have seen in chapter 2 that tesseral modes have the particularity of appearing preferentially for bubbles whose radii are far from the modal resonant radius, while zonal and sectoral modes give a preference to emerge close to that resonant radius. This result is also verified for bubbles excited at constant acoustic pressure and displayed in figure 3.9 for modal degrees $n = 3$, $n = 4$, $n = 5$ and $n = 6$. This gives a possibility for zonal and sectoral modes to exist simultaneously, with the particularity of modal degrees $n = 3$ and $n = 6$ for which this happens at over-resonant radii. The coexistence of tesseral and sectoral modes is quite common too, and will be discussed in section 3.2.5. In contrast, the coexistence of a tesseral mode with another one or with a zonal mode was not observed, at the magnitudes of acoustic pressure explored here. The calculation of the

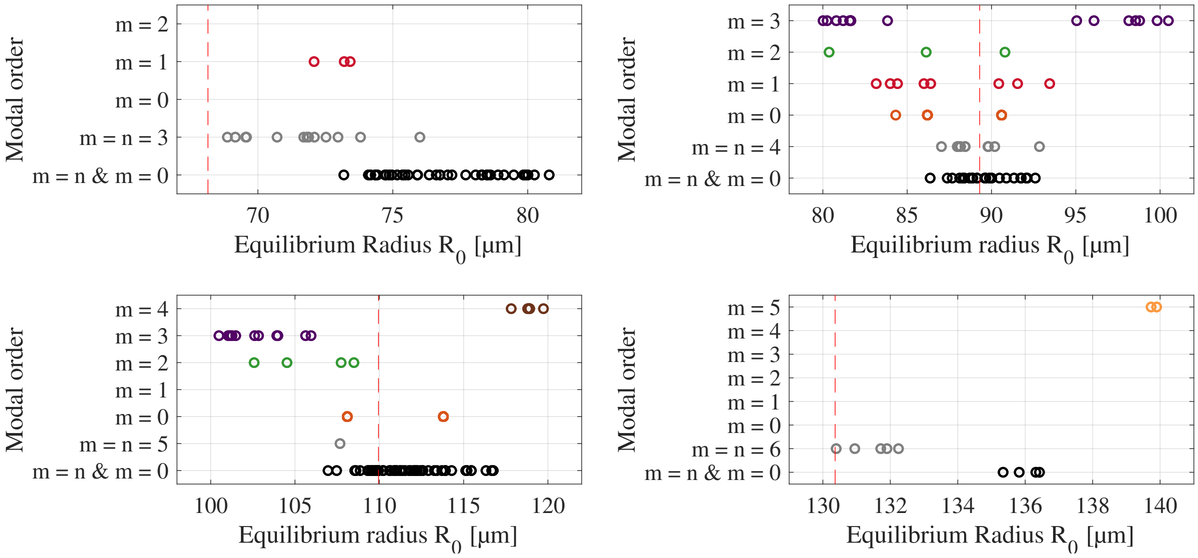

Figure 3.9: Distribution of the experimental occurrences of nonspherical modes for bubbles whose equilibrium radius R_0 is located around the resonant radius associated to the modal degrees $n = 3$ (top left), $n = 4$ (top right), $n = 5$ (bottom left) and $n = 6$ (bottom right), given by the red dashed vertical lines.

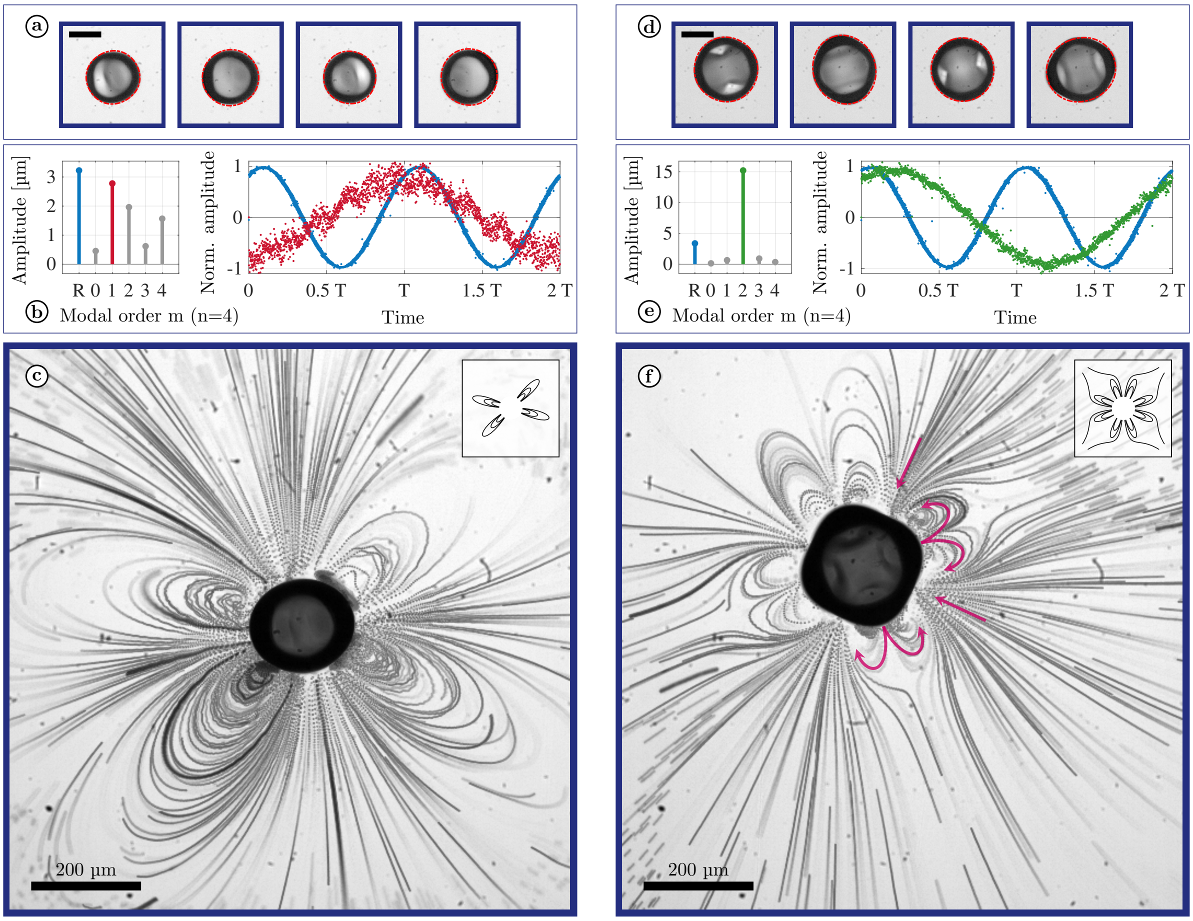

Figure 3.10: Modal analysis of the dynamics and associated microstreaming pattern of microbubbles of equilibrium radius 86.4 µm oscillating on a tesseral mode of order $m = 1$ (left) and a microbubble of equilibrium radius 102.6 µm oscillating on a tesseral mode of order $m = 2$ (right). Both are generating a $4m$-lobe flower-shaped pattern. The information is similarly structured as in figure 3.3.

modal amplitude of a tesseral mode Y_{nm} writes

$$a_{nm}(t) = \frac{\gamma_{nm}}{2\pi}\int_0^{2\pi} s(\phi,t)e^{-im\phi}\,d\phi, \tag{3.5}$$

where $\gamma_{nm} = \left(f_{nm}P^*_{nm}\sin\theta^*_m\ \frac{s^*(\phi,t)}{R_0+\tilde{a}_{nm}f_{nm}P^*_{nm}}\right)^{-1}$.

Tesseral modes also differ from zonal and sectoral modes by the presence in their modal deformations of nodal lines in both elevation and azimuth. For instance, each tesseral mode of order $m = 1$ has two nodal meridians, regardless the modal degree n it belongs to, but a number of $n - m$ nodal parallels that differs with its degree. In a microscope top-view configuration, the observation of the bubble and the induced particles

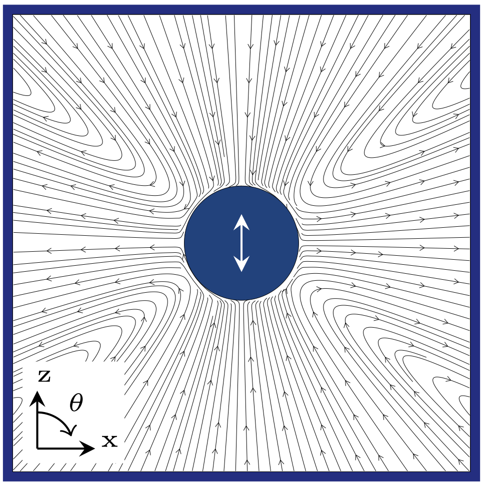

Figure 3.11: Theoretical prediction of the side-view microstreaming induced by the self-interaction of an axisymmetric mode of degree $n = 1$, i.e. a roughly vertical translation oscillation. Issued by Inserra et al. [2020a], the streaming pattern has a quadrupole shape, closely similar to the one induced by a tesseral mode $m = 1$, as illustrated in figure 3.10c.

motion is performed in a horizontal focal plane of finite thickness. From that perspective, at a given angle θ, the azimuthal bubble contour of any tesseral mode 1 possesses two nodes and two anti-nodes of displacement. As a direct consequence, all the self-interacting tesseral modes $m = 1$ ever experienced in this work for $n = 3$ to $n = 6$ have always developed from a top-view a microstreaming characterized by a 4-lobe shape, as an example is illustrated in figure 3.10c. This is in line with the previous logic related to sectoral modes, where the number of recirculation loops equals two times the number of nodal meridians. The particles are thus animated by a flow motion going away from the displacement anti-nodes and towards the displacement nodes of the bubble interface. An analogy can be drawn between such a tesseral mode $m = 1$ observed in a horizontal focal plane and a solid-body translation oscillation without shape deformation. Such bubble translation motion is widely investigated in literature and generally associated to quadrupole-shaped patterns [Longuet-Higgins, 1998, Collis et al., 2010, Doinikov et al., 2019b], as an example is given in figure 3.11. The resemblance with the streaming pattern induced by a tesseral mode $m = 1$ is close (see figure 3.10c).

Analogously, tesseral modes of order $m = 2$ possess four nodal meridians. Similarly, it is expected that such bubble oscillation would generate a microstreaming characterized by $4m$ lobes, and this is exactly what is shown in figure 3.10f, where eight lobes are clearly visible. Similarly as the tesseral mode $m = 1$, the $4m$ recirculation loops are assembled two by two, each pair being located between two displacement nodes of the bubble interface and surrounded by region of dense streamlines associated to a fluid motion going

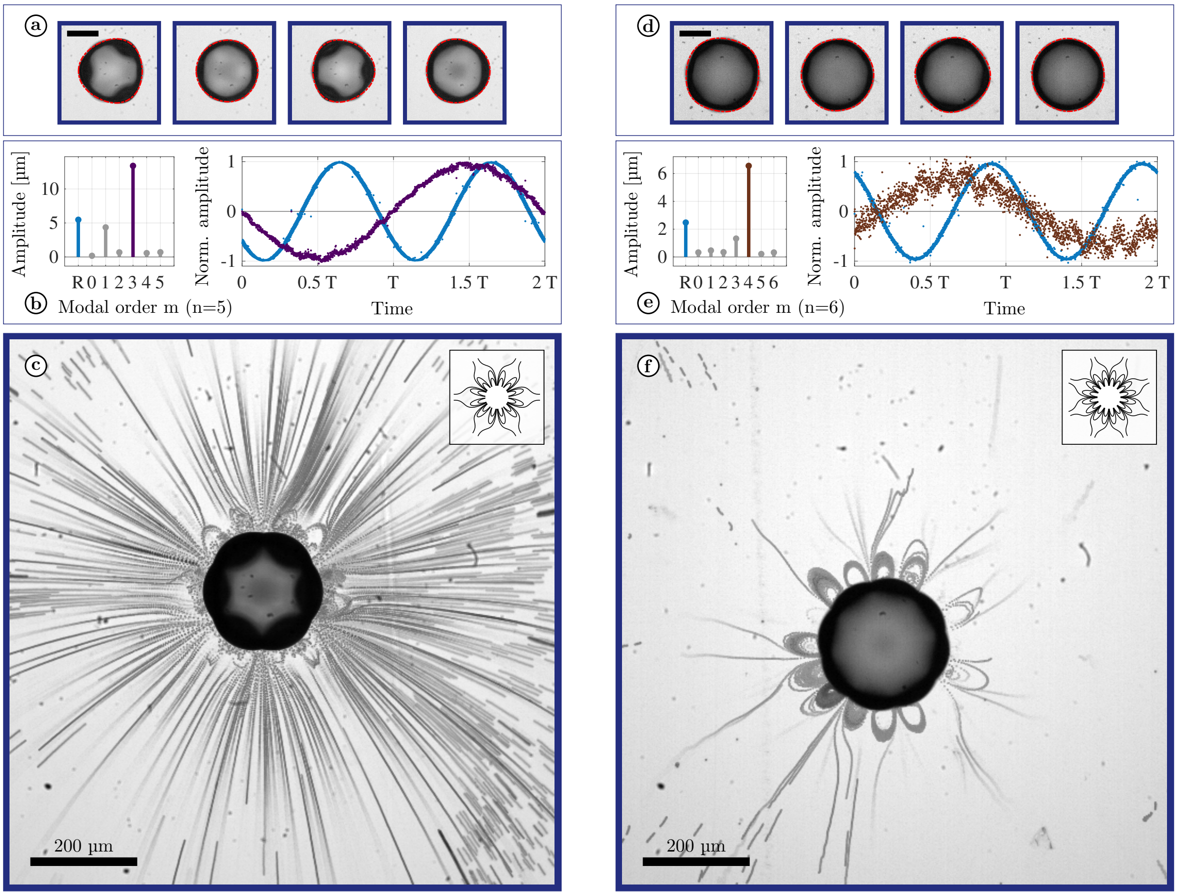

Figure 3.12: Modal analysis of the dynamics and associated microstreaming pattern of a microbubble of equilibrium radius 101.5 µm oscillating on a tesseral mode of order $m = 3$ (left) and a microbubble of equilibrium radius 118.8 µm oscillating on a tesseral mode of order $m = 4$ (right). Both are generating a $4m$-lobe flower-shaped pattern. The information is similarly structured as in figure 3.3.

towards the bubble interface. The bubble nonspherical mode here represented belongs to the modal degree $n = 4$. We believe that as the presence of the wall facilitates the triggering of some asymmetric modes, it might in the same way inhibits others. This might be the reason why we have not experienced self-interacting tesseral mode $m = 2$ for every modal degrees n that were investigated in this work.

As illustrated in figure 3.12, the microstreaming induced by tesseral modes of order $m = 3$ and $m = 4$ exhibits a similar signature: $4m$ lobes assembled by pair, with a great density of particles in the equatorial plane coming towards the bubble interface and more particularly towards the displacement nodes of the bubble interface. In addition, it appears that the recirculation loops become smaller as the modal order m increases.

Lastly, it is worth noting a difference that exists between the microstreaming associated to a bubble animated by a tesseral mode or a sectoral mode. While both present a very similar streaming with a $4m$-lobe flower shape, the major distinction between them is the sign of the radial direction of the fluid motion in the equatorial plane, positive for sectoral modes and negative for tesseral modes.

With these first three experimental cases, we made the tour of our top-view experimental microstreamings induced by a wall-attached bubble exclusively animated by each of the main classes of spherical harmonics: zonal, sectoral and tesseral. There remain two scenarios of modal interaction that we met all along this experimental work. First, the probably least shy and most stable configuration: the modal coexistence and interaction between a sectoral and a zonal mode. Lastly, the probably most difficult to identify and quantify, but not so rare, configuration: the modal coexistence and interaction between a sectoral and a tesseral mode.

3.2.4 The "sectoral and zonal modes combo" case

By investigating the shape modes dynamics of a wall-attached bubble, we have evidenced in chapter 2 the recurrent coexistence of sectoral and zonal modes around the resonant radius and reported it in Physical Review E [Fauconnier et al., 2020]. The emergence of bubble nonspherical modes was investigated along an increasing pressure ramp, and the triggering of zonal and sectoral modes oscillating simultaneously was highlighted. In this current experimental configuration aiming at the study of the induced microstreaming, bubbles are driven at constant acoustic pressure, but the coexistence of zonal and sectoral is still frequently observed. As a reminder, microstreaming results from the interaction between two modes oscillating at the same frequency [Doinikov et al., 2019a], as well as the self-interaction of a shape mode [Inserra et al., 2020a]. The microstreaming induced by a bubble oscillating predominantly on two parametrically-excited shape modes (here the zonal and sectoral ones), in addition to the spherical oscillation (oscillating at the driving frequency), will lead to the second-order velocity field

$$\boldsymbol{v}^{(2)} \simeq \boldsymbol{v}^{(2)}_{z-s} + \boldsymbol{v}^{(2)}_{z-z} + \boldsymbol{v}^{(2)}_{s-s}, \tag{3.6}$$

where $\boldsymbol{v}^{(2)}_{z-s}$ refers to the second-order velocity induced by the interaction of zonal and sectoral modes, and $\boldsymbol{v}^{(2)}_{z-z}$ (respectively $\boldsymbol{v}^{(2)}_{s-s}$) refers to the second-order velocity induced by the self-interacting zonal mode (respectively sectoral mode). The interaction between two modes would be the largest when they are in phase quadrature [Marmottant and Hilgenfeldt, 2003]. As a result, depending on the phase and amplitude relations between zonal and sectoral modes, one or another contribution is likely to prevail on others. Capturing and measuring with accuracy the modal variables becomes then critical. When sectoral and zonal modes coexist, the calculation of the amplitude $a_{n0}(t)$ of the zonal

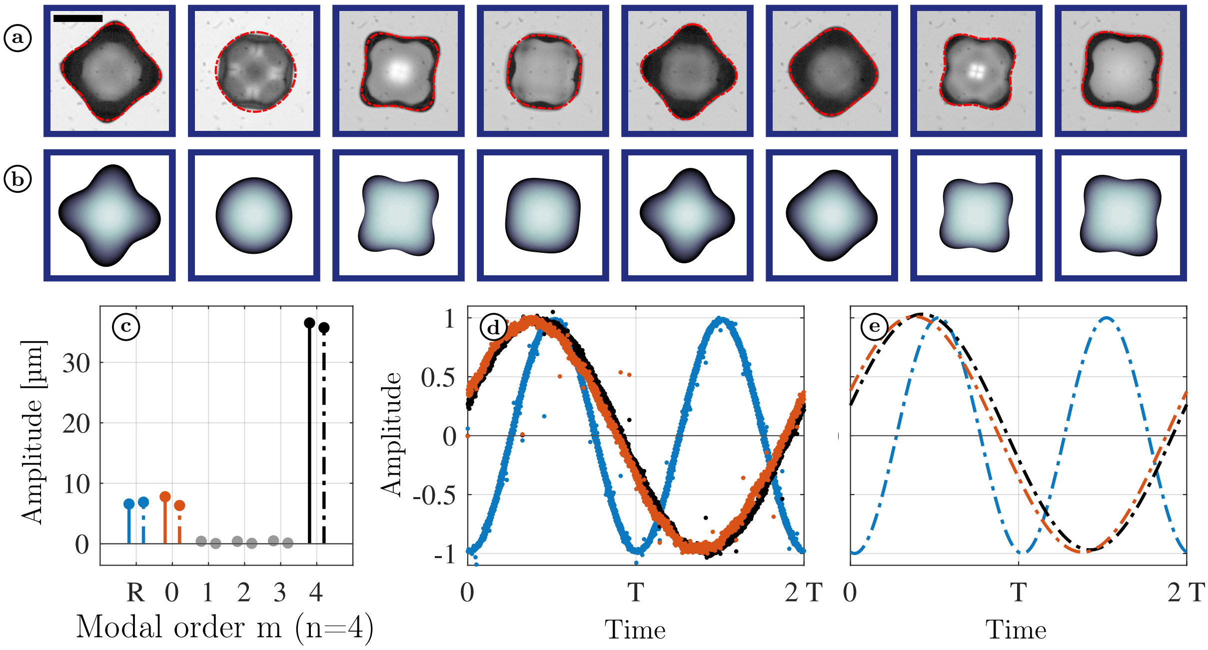

Figure 3.13: Example of the result obtained with our modal analysis method, here applied to a bubble of radius 88.1 µm oscillating simultaneously on a sectoral and a zonal mode of degree $n = 4$. The information is structured as follows. (a) Snapshot series of the top-view contour display the microbubble at different instants along a complete subharmonic period of duration 2T. The scale bar equals 100 µm. The red contour is a numerical reconstruction issued from the processed modal amplitudes displayed in (b). (b) Snapshots of a numerical bubble, implemented with the parameters obtained from the modal analysis of the experimental bubble. (c) Spectrum of the excited modes $n = 4$ of the experimental bubble (solid lines) and the numerical bubble (dashed lines) is expressed in µm, as a function of the modal order m, 'R' standing for the radial oscillation ($m = n = 0$). Temporal evolution of the normalized amplitudes of the predominant radial, zonal and sectoral refolded over two acoustic periods for the experimental bubble (d) and the numerical bubble (e).

mode is performed as in section 3.2.1, but the calculation of the amplitude $a_{nn}(t)$ of the sectoral mode requires some adjustments. The reason for that is the shift of the longitudinal position of the maximal displacement of the sectoral mode, as it does in the last two schematics of figure 3.4c. The amplitude $a_{nn}(t)$ is then no longer normalized by the associated Legendre Polynomial at $\theta = \frac{\pi}{2}$, but by the general expression

$$a_{nn}(t) = \frac{\gamma_{nn}}{2\pi} \int_0^{2\pi} s(\phi, t) e^{-in\phi} \, d\phi, \tag{3.7}$$

where $\gamma_{nn} = \left(f_{n0} P^*_{n0} \sin\theta^*_m \, \frac{s^*(\phi,t)}{R_0 + \tilde{a}_{nn} f_{nn} P^*_{nn}} \right)^{-1}$. Figure 3.13 demonstrates the ability of our method for approaching the amplitudes of zonal and sectoral modes. The top-view observation of an experimental microbubble's silhouette of equilibrium radius 88.1 µm al-

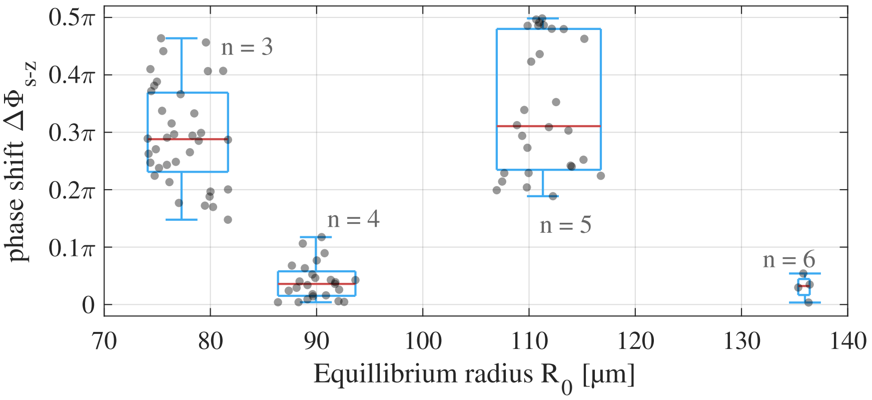

Figure 3.14: Distribution of the phase shift $\Delta\Phi$ between zonal and sectoral modes as a function of the bubble's equilibrium radius R_0, for degrees $n = 3$ to 6.

lows not only the detection of the presence of radial, zonal and sectoral modes, but also an accurate quantification of their respective amplitude and relation of phase. In order to validate our method, a similar modal analysis has been performed on a numerical bubble's silhouette implemented from the obtained experimental parameters (a_{00}, a_{40}, a_{44} and the relative phase shifts). Figure 3.13 shows that the modal amplitudes are accurately recovered (maximal error of 2 µm), as it is the case for the phase shift.

Above the instability pressure threshold of a given degree n, the occurrence of sectoral modes alone is scarcer than the coexistence of sectoral and zonal modes. In addition, sectoral and zonal modes of even degree $n = 4$ and $n = 6$ evidence a recurrent disposition to oscillate in-phase, unlike modes of odd degree $n = 3$ and $n = 5$ for which the phase shift is greater and may vary in a broader range. This behavior is summed up in figure 3.14 for the whole set of experimental data, each dot being a different microbubble animated simultaneously by a zonal and a sectoral mode. When it concerns odd degree ($n = 3$ and $n = 5$), we know that zonal and sectoral modes never oscillate in phase and coexist in a more competitive behavior (see section 2.2.6), highlighted here with an important variance of their phase shift. It varies within a broad range $[0.1\pi\ 0.5\pi]$, in contrast with the case of even degree $n = 4$ and 6 where the phase shift is recurrently constrained below 0.1π. We remind that the magnitude of the microstreaming interaction is governed by the phase shift between the two interacting modes [Longuet-Higgins, 1998, Marmottant and Hilgenfeldt, 2003]. Following the work of Longuet-Higgins [1998], when a radial oscillation (of amplitude ϵ_0) interacts with a translation oscillation (amplitude ϵ_1), the magnitude of the resulting flow is given by the so-called dipole strength $d_2 = \epsilon_0\epsilon_1 R_0^2 \sin\Delta\Phi$, where $\Delta\Phi$ is the phase shift between the radial and translation oscillations. Accordingly, we can therefore expect the interaction of zonal and sectoral modes of even degree to be weaker in comparison to the one induced by odd degrees.

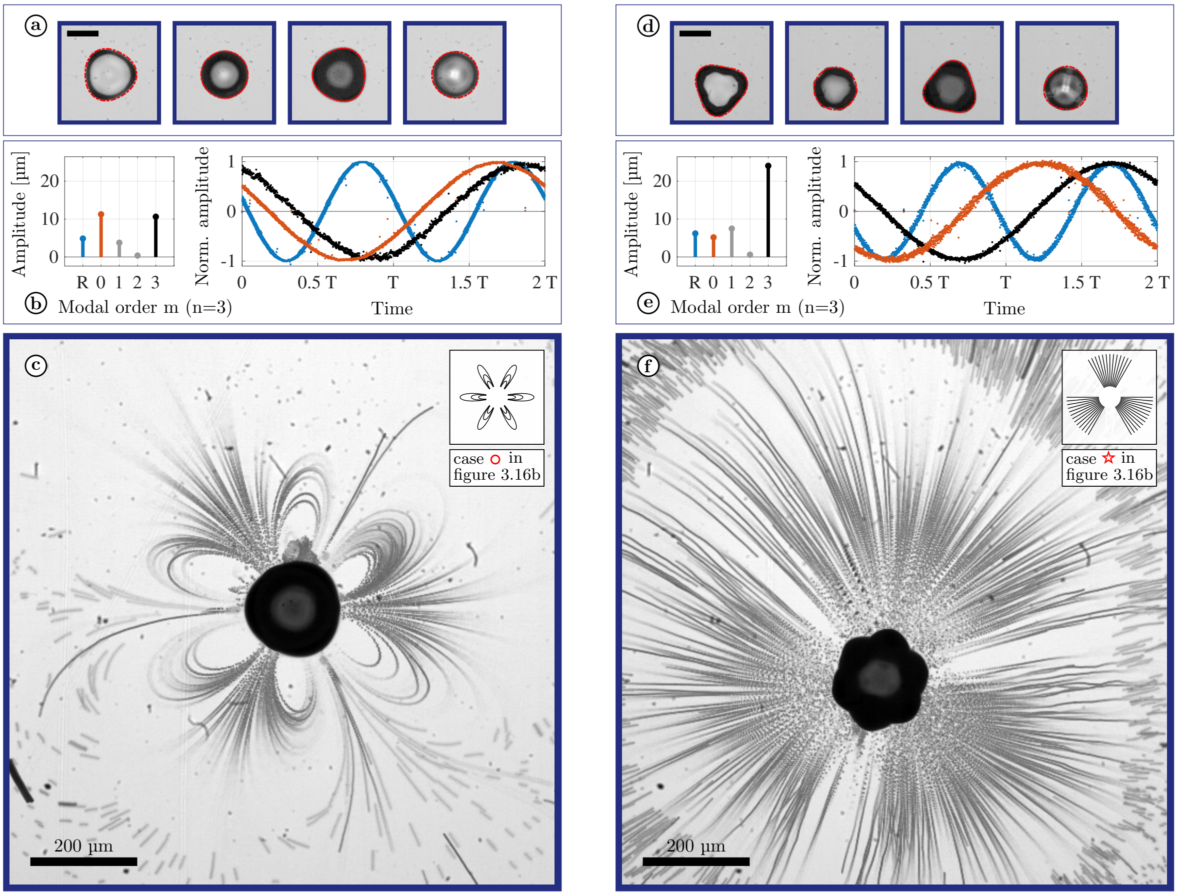

Figure 3.15: Modal analysis of the dynamics and associated microstreaming pattern of a microbubble of equilibrium radius 80.2 µm oscillating on a sectoral mode and a zonal mode of degree $n = 3$, generating a $2n$-lobe flower-shaped streaming pattern (left) and of a microbbuble of equilibrium radius 75.4 µm oscillating on a sectoral mode and a zonal mode of degree $n = 3$, generating a n-pointed star-shaped streaming pattern (right). The information is similarly structured as in figure 3.3.

When a bubble oscillates simultaneously on a zonal and a sectoral mode of degree $n = 3$, two different scenarios of microstreaming stand out, as illustrated in figure 3.15. Both scenarios clearly differentiate themselves in the ability for the streaming flow to present or not recirculation loops in the visualized equatorial plane. In figure 3.15c, a $2n$-lobe flower shape characterized by a fluid flow moving away from a displacement antinode of the bubble interface and coming back towards another is observed. Actually, it is very likely that the particles are actually heading towards zonal-related nodes of displacement that are hidden at a different position in elevation. The progression from a sharp to a blurry appearance of particles throughout their looping circulation reinforces this hypothesis. This $2n$-lobe flower-shaped pattern contrasts with the one shown in figure 3.15f where particles are propelled from the bubble interface with an outward one-

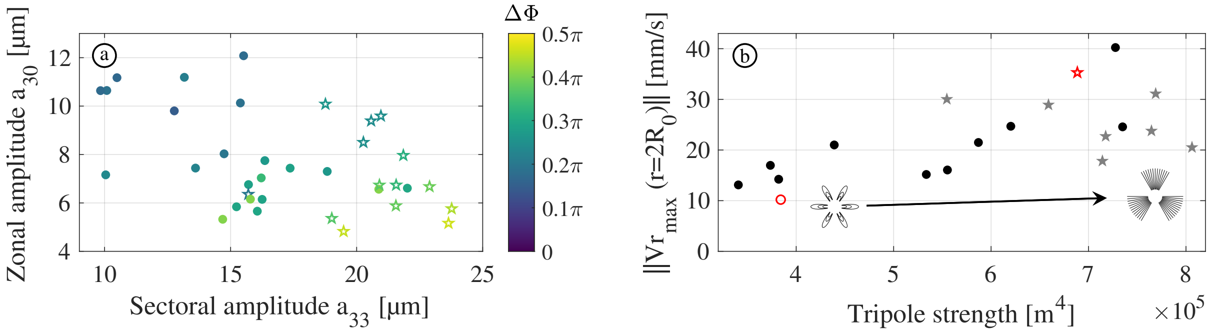

Figure 3.16: The preferential appearance of flower-shaped (•) or star-shaped (☆) patterns induced by a combination of sectoral and zonal modes of degree $n = 3$ is investigated as a function of their phase shift ΔΦ and amplitudes a$_{33}$ and a$_{30}$ (a) as well as a function of their tripole strength $= a_{30} \cdot a_{33} \cdot R_0^2 \cdot \sin \Delta\Phi$ correlated by the maximal radial velocity of propelled particles Vr_{max} measured at a distance $r = 2R_0$ from the bubble barycenter (b). Two particular red open markers represent the two chosen cases of figure 3.15 and their position in this tripole strength map.

way motion. For the degree $n = 3$, this pattern resembles a star with 3 branches, and we refer to it as a n-pointed star shape. These two patterns are resulting from a bubble exhibiting both a zonal and a sectoral oscillation, as shown in the modal analysis displayed in figures 3.15b and 3.15e. Clearly, both the amplitudes of the nonspherical modes and their phase shift differ, and so are the relative strength of each interaction underlying the two presented patterns, as indicated in equation (3.6). For the bubble exhibiting a $2n$-lobe shape in figure 3.15c, the pattern probably results from the three-fold interaction described in equation (3.6), without predominance of one on another. However, due to the greater phase shift between zonal and sectoral modes in the case of the n-pointed star shape, the interaction between these two modes on the resulting pattern is probably predominant. It is worth noticing that this pattern looks like a zonal-induced microstreaming pattern (see figure 3.3c for instance), but here regularly interrupted with a spatial period $2\pi/n$.

In order to understand how these two scenarios differ, figure 3.16a gives an overview of the experimental data where there is coexistence and interaction between a zonal mode and a sectoral mode of degree $n = 3$. The preferential occurrence of flower-shaped or star-shaped patterns is investigated as a function of the amplitudes of the sectoral mode a_{33} and the zonal mode a_{30}, as well as their phase shift ΔΦ. At a first glance, a preferential generation of flower shapes occurs when the sectoral amplitude is weak, regardless the zonal amplitude. On the other hand, when the sectoral mode amplitudes become stronger, star-shaped patterns become predominant. For these patterns, the tracking particles are propelled with such an important velocity that they are never steered back to the bubble interface and thus do not experience any recirculation loops. This observation is asserted by figure 3.16b where the propelling velocity of the particles measured at a distance $2R_0$ from the bubble center is plotted as a function of the tripole strength $d_3 = a_{30} \cdot a_{33} \cdot R_0^2 \cdot \sin \Delta\Phi$. This expression was inspired from the dipole strength as defined by Longuet-Higgins [1998] in the case of a translation bubble motion. Clearly, the generation of star-shaped patterns is associated to the highest magnitudes of tripole strength, while flower-shaped patterns are globally restricted to the lowest magnitudes.

Based on the observation of figure 3.16a, a correlation between phase shift and modal amplitudes, which highlights the modal competition of sectoral and zonal modes of degree $n = 3$ mentioned before, also deserves to be noted. As a matter of fact, the modal coexistence does not happen unconditionally, quite the contrary. The progressive rise in power of the sectoral mode conditions the zonal mode, provided that a phase shift operates and that the zonal mode suffers a reduction in its amplitude.

Lastly, it should be specified that, due to some inadequate sets of data for accurately measuring the particles velocity through the Fiji software [Schindelin et al., 2012] and the plugin Trackmate [Tinevez et al., 2017], the number of experimental occurrences of figure 3.16b differs from the number in figure 3.16a.

When $n = 5$, similar results come out. Same $2n$-lobe and n-pointed star-shaped patterns are observed. Similarly as before, the strongest sectoral amplitude is associated to the n-pointed star shape (figure 3.17f) in comparison to the lobe-type pattern (Fig 3.17c). For the results presented here, identical magnitudes of the zonal oscillations are obtained for both cases. Figure 3.18 gives an overview of the distribution map of microstreaming patterns induced by interacting zonal and sectoral modes of degree $n = 5$, as a function of their phase shift and modal amplitudes a_{55} and a_{50}. Even if a clear boundary between star-shaped and flower-shaped patterns is not as obvious as it was for the case $n = 3$, the global trend still goes in the direction of a preferential generation of star-shaped patterns when the sectoral mode outweighs the zonal amplitude. On the other hand, at weaker zonal and sectoral amplitudes, star-shaped patterns can only arise when the phase shift is sufficiently large. Somehow, the phase shift compensates the weak sectoral mode and facilitates in this way the emergence of star-shaped patterns. This is further proof that star shapes and flower shapes are related patterns that have a common boundary, a critical threshold in intensity of interaction that swings the response of the fluid from one pattern to another. Finally, a correlation between phase shift and modal amplitudes also deserves to be mentioned. Unlike the case $n = 3$, the phase shift is here inversely related with the sectoral amplitude.

Sectoral and zonal modes of even degree $n = 4$ show ease to coexist. They emerge and exist together without inhibiting each other [Fauconnier et al., 2020]. As a result, their phase shift is not as variable as it was for odd-degree modes (see figure 3.14), and the microstreaming patterns are then less different and exclusively limited to $2n$-lobe flower

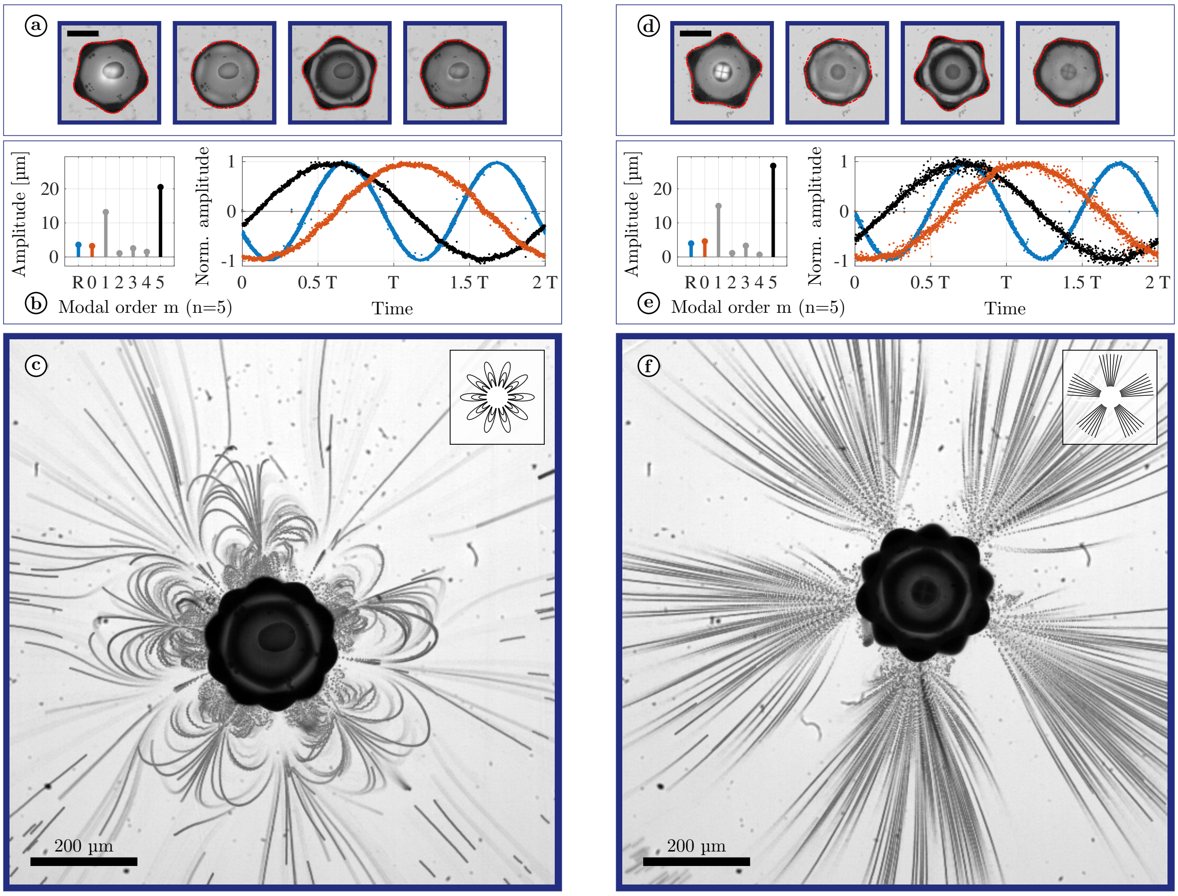

Figure 3.17: Modal analysis of the dynamics and associated microstreaming pattern of a microbubble of equilibrium radius 112.1 µm oscillating on a sectoral mode and a zonal mode of degree $n = 5$, generating a $2n$-lobe flower-shaped streaming pattern (left) and of a microbubble of equilibrium radius 110.2 µm oscillating on a sectoral mode and a zonal mode of degree $n = 5$, generating a n-pointed star-shaped streaming pattern (right). The information is similarly structured as in figure 3.3.

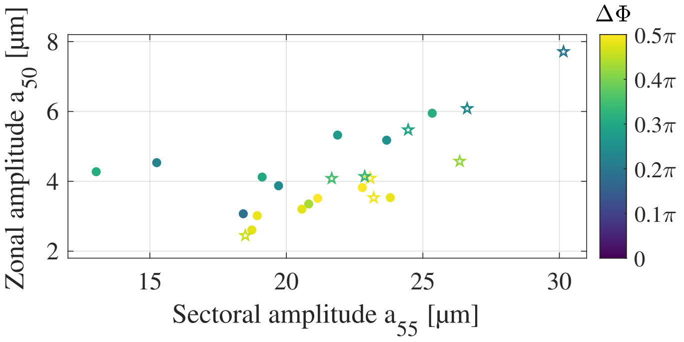

Figure 3.18: The preferential appearance of flower-shaped (●) or star-shaped (☆) patterns induced by a combination of sectoral and zonal modes of degree $n = 5$ is investigated as a function of their phase shift $\Delta\Phi$ and amplitudes a_{55} and a_{50}.

shapes (see figure 3.19). Despite this, we will see in figure 3.20 that we yet experienced a great variability in the magnitudes of fluid velocity.

The two different scenarios illustrated in figure 3.19 are related to closely similar asymmetric modal amplitudes and phase shift between zonal and sectoral oscillations, while they display the two most opposite microstreaming patterns we experienced for the case of a degree $n = 4$. Since the interaction strength of even-degree zonal and sectoral modes is generally less than that of largely phase-shifted odd-degree modes, it results in flower-shaped patterns with early stages of star shapes instead of fully developed star-shaped patterns. When measuring the velocity of particles propelled by the bubble anti-nodes at a distance $2R_0$, clear differentiation occurs between the flower shapes and the seemingly 4-pointed star shapes (see figure 3.20). This differentiation occurs along the amplitude of

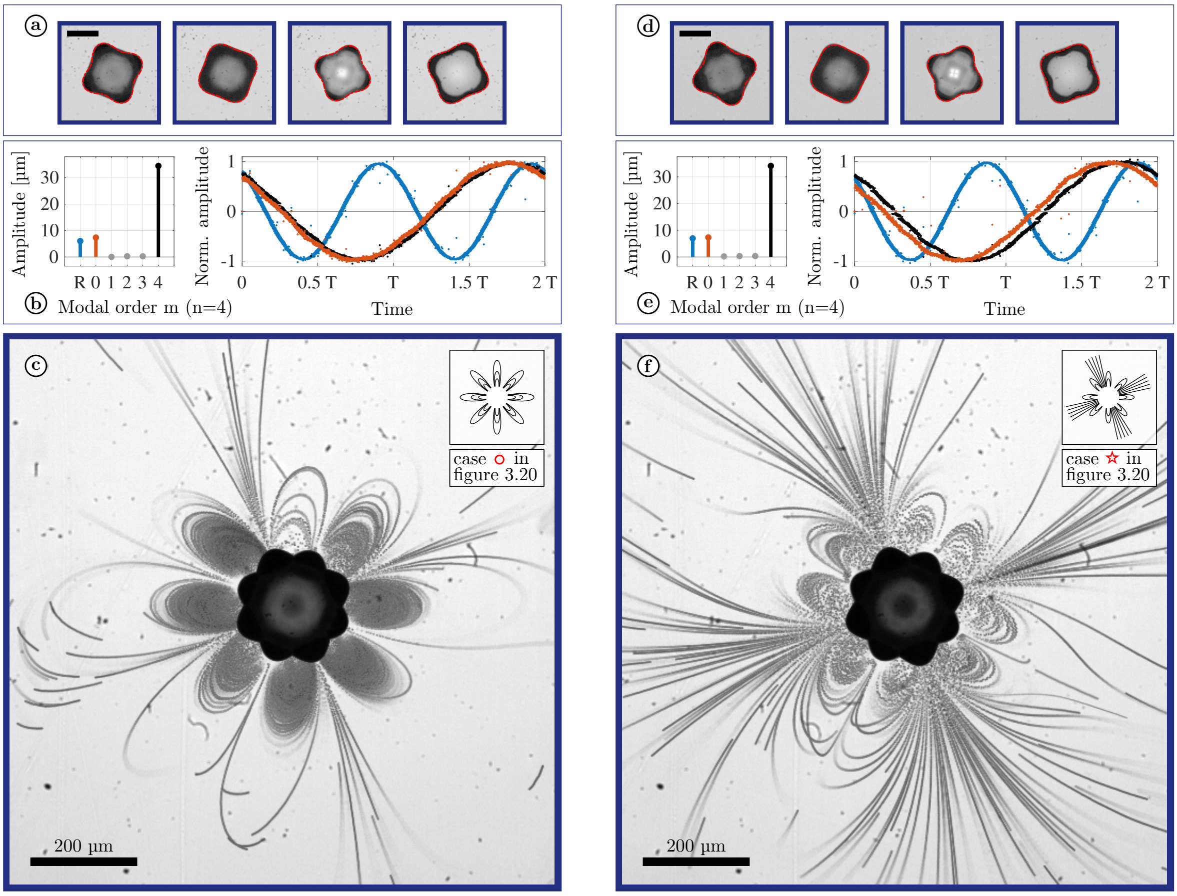

Figure 3.19: Modal analysis of the dynamics and associated microstreaming pattern of a microbubble of equilibrium radius 87.4 µm oscillating on a sectoral and a zonal mode of degree $n = 4$ generating a $2n$-lobe flower-shaped streaming pattern (left) and of a microbubble of equilibrium radius 87.7 µm oscillating on a sectoral and a zonal mode of degree $n = 4$ generating a $2n$-lobe flower-shaped streaming pattern accompanied with early stages of a star shape (right). The information is similarly structured as in figure 3.3.

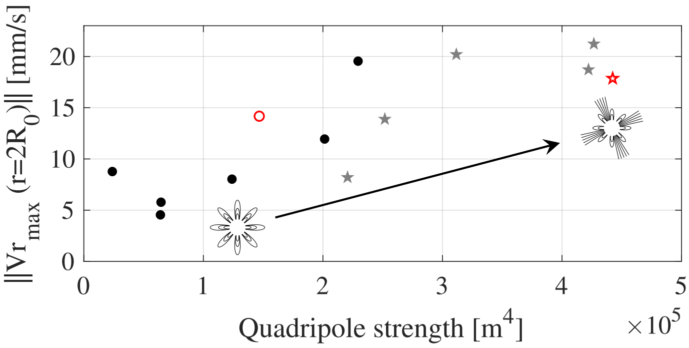

Figure 3.20: The preferential appearance of flower shapes (●) or flower shapes with early stages of star shapes (☆) induced by a combination of sectoral and zonal modes of degree $n = 4$ is investigated as a function of their quadrupole strength $= a_{40} \cdot a_{44} \cdot R_0^2 \cdot \sin \Delta\Phi$ correlated by the maximal radial velocity of propelled particles $\mathrm{Vr}_{\max}$ measured at a distance $r = 2R_0$ from the bubble barycenter. Two particular red open markers represent the two cases selected in figure 3.19 and their position in this quadrupole strength map.

the quadrupole strength $d_4 = a_{40} \cdot a_{44} \cdot R_0^2 \cdot \sin \Delta\Phi$. Again, confined flower-shaped patterns are clearly restricted at the lowest magnitudes of quadrupole strength. On the other hand, higher magnitudes of quadrupole strength seem to force the fluid flow to adopt more like an outward one-way motion (see figure 3.20f).

Concerning sectoral and zonal modes of degree $n = 6$, the coexistence is also facilitated. Figure 3.14 evidenced a phase shift between modes always confined below 0.05π. This translates into even less diversified streaming signatures as in the case of degree $n = 4$. Not helped by a higher modal density, only a few rare cases of coexistence between zonal and sectoral modes absent from any other tesseral mode were experienced, an example

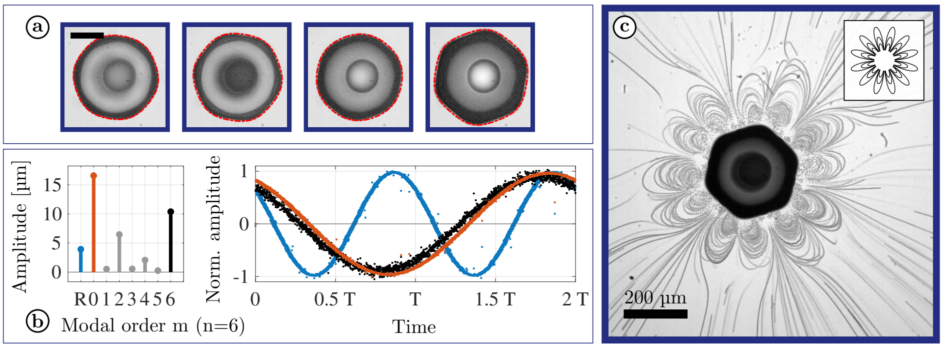

Figure 3.21: Modal analysis of the dynamics and associated microstreaming pattern of a microbubble of equilibrium radius 135.8 µm oscillating on a sectoral mode and a zonal mode of degree $n = 6$, generating a $2n$-lobe flower-shaped pattern. The information is similarly structured as in figure 3.3.

of which is given in figure 3.21. This streaming pattern with twelve lobes summarizes all cases of interacting sectoral and zonal modes of degree $n = 6$.

3.2.5 The "sectoral and tesseral modes combo" case

The fifth and last experimental case concerns the microstreaming induced by an interaction between sectoral and tesseral modes. Due to the complexity of discerning the tesseral mode oscillation from the sectoral one, the bubble modal content is in this case only investigated in a qualitative way. Figure 3.22a (respectively, figures 3.22b and 3.22c) presents an experimental case of interaction of a sectoral mode $n = 3$ with a tesseral mode $m = 1$ (respectively, a sectoral mode $n = 4$ with a tesseral mode $m = 2$, and a sectoral $n = 4$ with a tesseral mode $m = 1$). All these three nonspherical bubbles generate a 4-lobe streaming pattern. Figure 3.22d presents an experimental case of interaction of a sectoral mode $n = 6$ with a tesseral mode $m = 3$. It generates a 6-lobe shaped pattern. Experimental occurrences of streaming induced by sectoral and tesseral modes are not the most usual and certainly not the easiest scenario to analyze and interpret. It will be difficult to draw conclusion, since the number of possible modal configurations is important and not all of them are observable in our configuration. As a reminder, the tethering to the wall acts as a filter on the bubble modal behavior, facilitating the emergence of certain nonspherical modes and inhibiting others. These four examples given in figure 3.22 have been wisely chosen among the large panel of patterns in order to illustrate the non-exclusivity of specific patterns (here, 4-lobe shape) to a single bubble modal configuration and that, in definitive, a rule of thumb can not be easily advanced.

To sum up the results on streaming patterns, figure 3.23 gives an overview of the complete variety and classification of the microstreaming patterns induced by nonspherical modes of an ultrasound-driven wall-attached bubble, as they were experienced in this work. Four experimental cases are summarized here: self-interacting zonal, self-interacting sectoral, self-interacting tesseral and zonal-sectoral interacting combo. Although a self-interacting sectoral mode and a self-interacting tesseral mode of a same order m generate similar top-view streaming signatures and are represented in figure 3.23 with similar $4m$-lobe symbols, they can be differentiated by considering the sign of the radial fluid velocity at the equator, as represented with pink arrows in figure 3.5c (for sectoral modes) and in figure 3.10f (for tesseral modes). In the case of sectoral modes, recirculation loops are assembled by pair with an inward motion, while in the case of tesseral modes, recirculation loops are assembled by pair with an outward motion. This feature is recurrent regardless the modal degree to which is related each sectoral or tesseral mode. In addition, we observed that sectoral modes of a wall-attached bubble give rise to an antifountain-like

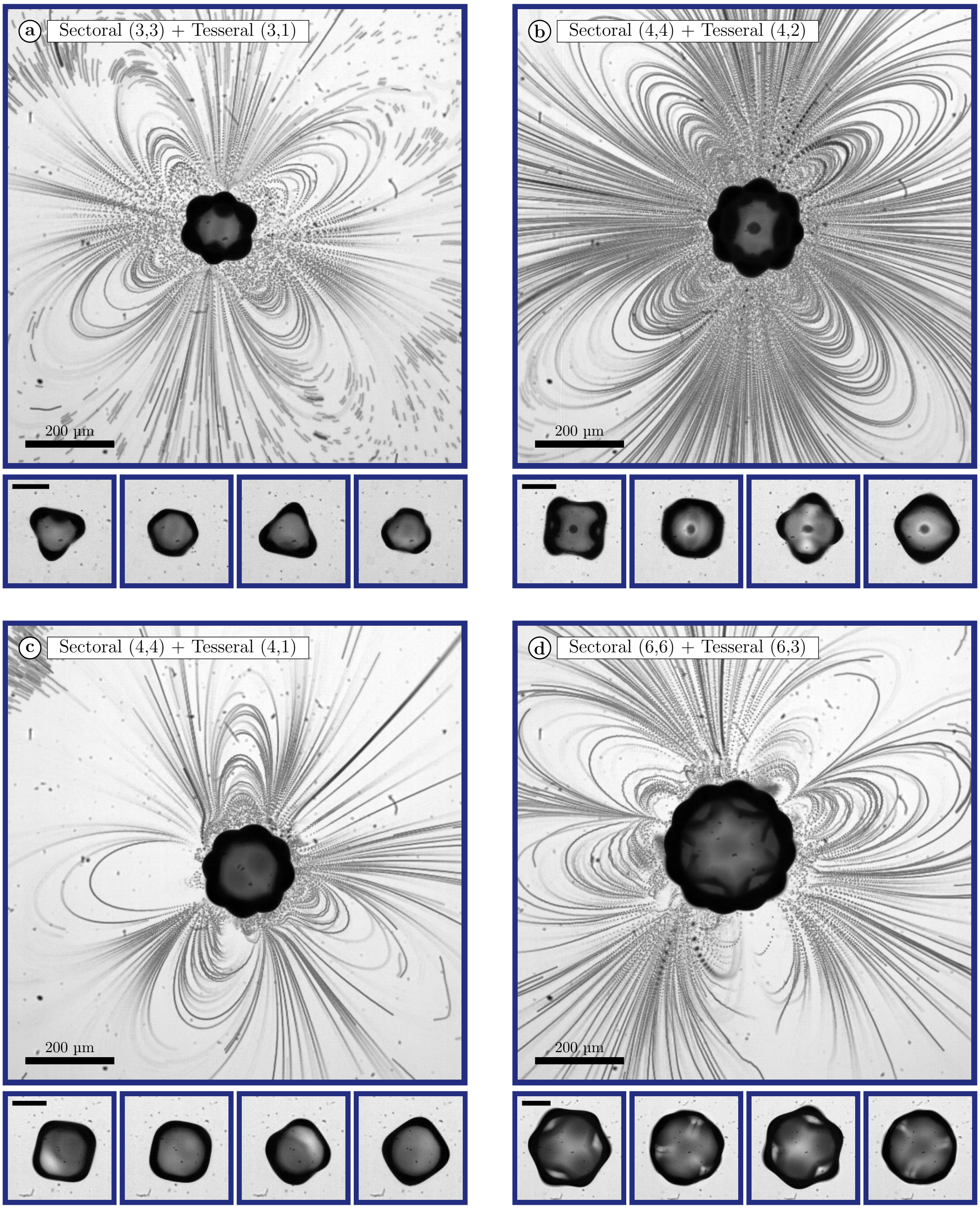

Figure 3.22: Microstreaming induced by a bubble of equilibrium radius 70.3 µm oscillating simultaneously on a sectoral mode $n = 3$ and a tesseral mode $m = 1$, generating a 4-lobe shaped pattern (a), by a bubble of equilibrium radius 90.8 µm oscillating simultaneously on a sectoral mode $n = 4$ and a tesseral mode $m = 2$, also generating a 4-lobe shaped pattern (b), by a bubble of equilibrium radius 92 µm oscillating simultaneously on a sectoral mode $n = 4$ and a tesseral mode $m = 1$, also generating a 4-lobe shaped pattern (c) and by a bubble of equilibrium radius 134 µm oscillating simultaneously on a sectoral mode $n = 6$ and a tesseral mode $m = 3$, generating a 6-lobe shaped pattern (d). The scale bars on the small snapshots all equal 100 µm.

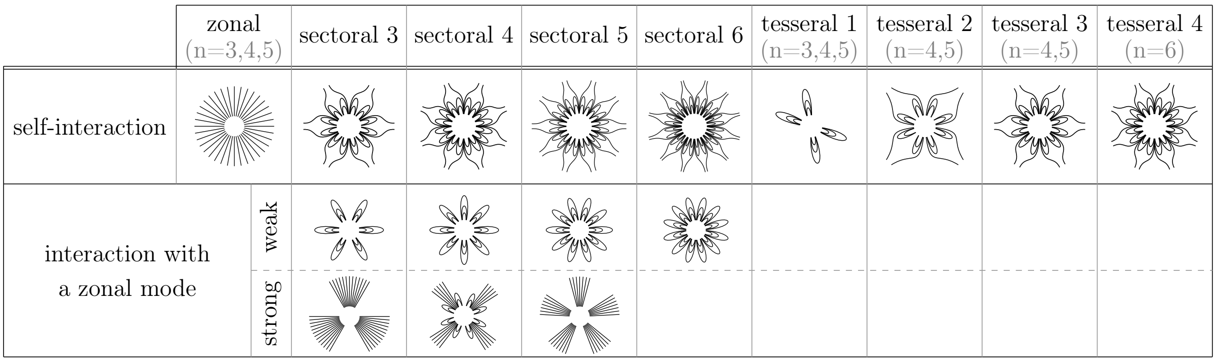

Figure 3.23: Schematics of the complete variety of the microstreaming patterns as we experienced them, from a top-view. The notations in gray on top of columns are the degrees for which we experienced the microstreaming patterns as described.

behavior of the surrounding fluid above the bubble, characterized with a negative radial velocity along the normal to the top wall surface (See figure 3.8), which may significantly differ in the case of tesseral and zonal modes.

3.3 Conclusion

The formation of specific microstreaming patterns induced by a wall-attached microbubble undergoing asymmetric shape modes is analyzed with respect to its time-resolved dynamics. In our experimental setup, each main class of spherical harmonics $Y_{nm}(\theta, \phi)$ is experienced: zonal ($m = 0 < n$), sectoral ($n = m \neq 0$) and tesseral ($0 < m < n$). The microstreaming induced by a bubble animated by a sectoral mode alone reveals a streaming signature characterized by a $4n$-lobe flower shape. Very similarly, self-interacting tesseral modes give rise to $4m$-lobe flower-shaped patterns. The modal configuration that involves tesseral and sectoral interacting modes is illustrated through four cases, for which a rule of thumb is hard to advance. On the other hand, in a scenario staging the coexistence of sectoral and zonal modes, the microstreaming induced by their interaction can produce two kinds of patterns: $2n$-lobe flower and n-pointed star shapes. The preferential emergence of one or another pattern of streaming is discussed on the basis of the modal amplitudes and phase shift between both shape modes. For modes of odd degree $n = 3$ and $n = 5$, an important modal competition induces greater phase shifts and thus stronger modal interaction and more diverse shapes of streaming patterns than in the case of even degree $n = 4$ and $n = 6$ where the modal coexistence is more facilitated. Globally, the amplitude of the sectoral mode, encouraged with a decisive phase shift, appears to have an important responsibility in the generation of a microstreaming signature characterized by a flower-shaped (weak amplitude a_{33}, phase shift and quadrupole strength) or a star-shaped (strong amplitude a_{33}, phase shift and quadrupole strength) pattern around the bubble.

Despite zonal and sectoral modes of even degree behave less competitively and present weaker phase shift and thus modal interaction, the level of flow spreading of the always recurrent $2n$-lobe flower shape seems to be governed by the streaming strength and its capacity to reach high magnitudes of radial velocity and to propel particles located in the equatorial plane with an outward one-way motion. Both scenarios, the flower-shaped and the star-shaped pattern, seem to have different areas of high velocity activity, confined near the bubble or away from the bubble in front of the anti-nodes of the bubble interface displacement, respectively. Controlling the bubble's size and dynamics could make it possible to promote the generation of one or another sort of streaming pattern, hence the oriented and optimized generation of shear stresses on a nearby wall or biological cell.

The now improved understanding of the dynamics and induced streaming of a non-spherically oscillating wall-attached microbubble will allow an in-depth explanation of the influence it can have on a nearby biological cell. To this end, chapter 4 explores original methods for assessing this mechanical interaction at both the acoustic and the fluidic time scales.

Chapter 4

Mechanical interaction with a biological cell

The sonoporation of a biological cell membrane is a recurrent topic of research whether it concerns the blood-brain barrier (BBB) opening or the transfection of genetic materials. Classically performed non-invasively by means of resonant microbubbles, another recurrent matter is the common knowledge that a cloud of acoustically driven microbubbles can be a very complex, erratic and destructive cocktail, especially when interacting with a population of biological cells. This chapter presents an experimental study of the bubble-cell interaction, based on two postulates:

- First, we believe that investigating this mechanical interaction at the micro-scale level of one single bubble and one single cell could help in understanding the complex macro-scale phenomenon.
- Second, because bubble nonspherical deformations are at the origin of important bubble displacements and formation of streaming, the focus will be on these bubble shape modes and their influence on a nearby biological cell.

With the perspective of studying these induced effects, two cellular models are suggested: an oocyte and a megakaryocyte. The nature of these cells and the good practices concerning their preparation are detailed in the first section 4.1. Section 4.2 takes stock of the experimental setup and the methods for manipulating the cells and for assessing their response. The experimental results are displayed in section 4.3 where the bubble-cell behavior is investigated at the single-cell scale through five consecutive approaches:

- the single bubble characterization in the cell medium (section 4.3.1),
- the bubble pushing-pulling action on a cell (section 4.3.2),
- the propagation of shear waves within a cell (section 4.3.3),
- the motion of cells in bubble-induced streaming (section 4.3.4),
- the internalization of fluorescent markers (section 4.3.5).

4.1 The choice of a cellular model

With the aim of investigating the mechanical interaction between a biological cell and a microbubble, a cellular model had to be selected by considering two important points: the size of the cell and its likeliness to be sonoporated. Because we are technically limited by a maximal recording rate of 180 kHz and hence the use of a low-frequency transducer, we are restricted in working with bubbles with relatively important sizes. In section 2.1.1 and figure 2.3, the acoustic response of our transducer has revealed its harmonic content and the possibility of working with bubbles of radius about 35 µm and 45 µm, respectively resonant at the 85 kHz third harmonic and the 66.5 kHz second harmonic, accordingly to Minnaert's frequency defined in equation (1.5). Since the objective is to approach a bubble-cell sizing ratio of 1:1 in order to be in a configuration comparable as those encountered in medical applications where UCA sizing in the range 1-10 µm injected in the bloodstream interact with red and white blood cells, a cellular model sizing in the diameter range 50-90 µm had to be found.

4.1.1 Oocytes

A first convenient cellular model which was easy for us to provide is a mouse oocyte. A handful of oocytes could be delivered to us by Jean-Michel Vicat and the Faculty of Medicine of Laënnec. For this precious help, we thank them very much.

Because it has a large size in the range 70-100 µm, such an oocyte is a perfect candidate to be placed near a similarly sizing bubble acoustically driven at 66.5 kHz. Even if occurrences of sonoporation of xenopus oocytes have been achieved by Deng et al. [2004], these cells are, by nature, reluctant to let in external foreign particles. Protected by an encompassing zona pellucida ensuring in particular a role of filter on what can enter, i.e. a spermatozoon with an intact plasma membrane, oocytes are at a first glance not really prone to be permeabilized.

Moreover, this zona pellucida appears to be somehow adhesive after having been collected from the animal. For the experimental purpose of Jean-Michel Vicat's team, the oocytes are washed and this adhesive layer is thus wiped out. At the end, when the cells are delivered to us, these adhesive properties are no longer. This does not help them to adhere to a substrate and a method must be found to efficiently fasten the cells. This is accomplished thanks to a microaspiration system, a glass capillary, a flexible hose and a syringe (Hamilton Gastight® 1710). The homemade manufacture of a glass capillary and the microaspiration method are presented later, in section 4.2.4.

The truth is that the sanitary crisis did not help to perform an extensive study on oocytes. This last part of thesis work chronologically arrived after the first works on the bubble dynamics, presented in previous chapters, and at the exact moment the COVID-

19 virus (SARS-CoV-2) entered our lives. For this reason, only two one-day series of experiments have been realized. Soon it became more convenient to dispose of cells without depending on an outside supplier and thus to start cultivating cells within our premises. This made it possible to manage the accessibility to cells during the consecutive lockdowns. For that reason, and due to a doomed lack of experimental data, no result on oocytes will be displayed in this chapter. Yet, some images and a brief discussion are given in appendix B.

4.1.2 Megakaryocytes

Another cellular model has been employed in this thesis work: a cell line of human megakaryoblasts MEG-01 (CRL-2021, American Type Culture Collection, Manassas, Virginia). They were selected for the purpose of our cell study not only for their nature and their likeliness to be targeted for sonoporation and drug deliverance in clinical applications, but also because of their particularity to have a large size when they are reaching maturity. These bone marrow cells are responsible for the production of thrombocytes in the vascular network and are characterized by a three-phase evolution, during which they grow in size. Firstly megakaryoblasts, they become then promegakaryocytes and afterwards megakaryocytes. At that final stage, they start developing a granular appearance due to the production on their membrane of thrombocytes, which they finally release in the blood circulation upon the cell itself breakup. Since we chose the largest cells among the whole cell population we could find to perform the bubble-cell interaction experiments, it is likely that these are fully mature megakaryocytes, and not megakaryoblasts. In addition, it is worth noting that these cells are not pleomorphic, in the sense that they maintain a constant shape common to all from the first to the final stage of their growth, namely a roughly spherical shape or a spherical capped shape for the adherent ones.

Cell culture

Concerning their culture, the cells were grown in $75\,\mathrm{cm}^2$ flasks (Corning®) filled with 15 mL Roswell Park Memorial Institute (RPMI) medium supplemented with 10 % fetal calf serum (FCS) and 1 % L-glutamin, then incubated at 37 °C and 5 % CO_2. The medium renewal is done twice a week. Although these cells do not show a high propensity to adhere to their substrate, this consists in scraping the few adherent ones, then centrifuging them and diluting the cellular pellet into 15 mL fresh medium at a ratio of 1:5 to 2:5 in order to keep the culture below a recommended approximate density of 10^6 cells/mL. Provided these conditions of culture are respected, they have the capacity to double their population in 36 to 48 hours.

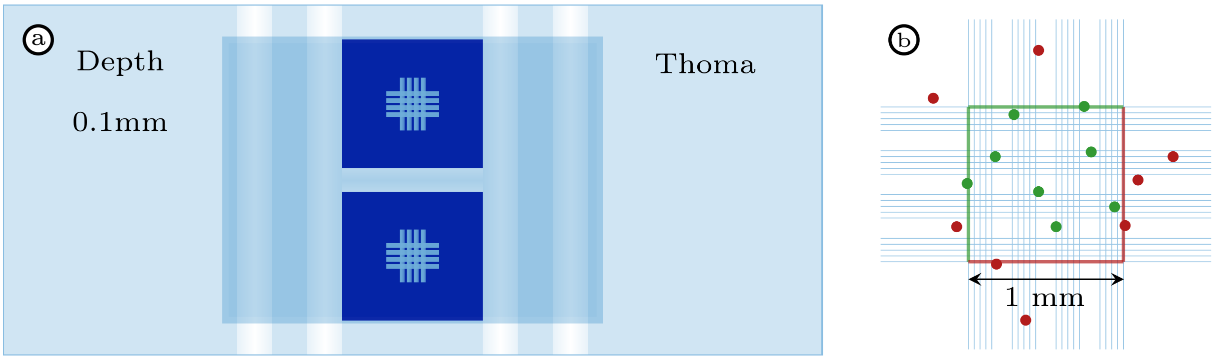

Figure 4.1: (a) Schematics of a Thoma's cell of which both counting-chambers are filled with a 10 µL sample of the initial cell culture solution diluted in 10 µL blue trypan solution. (b) A schematic zoom on a counting-chamber on which the method on how cells are taken into account (green ones) or not (red ones) in the total count, whether a cell is located inside or outside the large square, or on one of its four edges.

Cell counting

When there was a need for an important and controlled density of cells in the experimental tank, or more simply when there was a need for an information on the dilution rate to be carried out to optimize the cell culture, the counting of cells was performed using a trypan blue solution (Corning®, 29-900-CI 0.4 % in PBS) and a Thoma's cell of which a schematics is given in figure 4.1a. The Thoma's cell is a cytometer, a counting-chamber device that allows to make an estimation of the number of cells in suspension in an initial solution. 10 µL of this solution containing all cells is diluted in 10 µL of blue trypan solution, then inserted between a thin glass slide and the Thoma's cell, in the two counting-chambers. The count is done as illustrated in figure 4.1b, by taking into account the cells located inside the large square of 1 mm edge and located on top and left edges but not on right and bottom ones. This gives two numbers of cells, N_1 and N_2, one for each of both counting-chambers. Given that the thickness of solution under the glass slide measures 0.1 mm, the total volume then contained in each square is about 0.1 µL. The final number of cells in the initial solution is then approximated by applying the following calculation

$$\text{Number of cells } /\text{mL} = \frac{N_1 + N_2}{2} \, f_{cd} \, 10^4 \tag{4.1}$$

where f_{cd} is the concentration-dilution factor, which equals 20 µL / 10 µL = 2, in our case.

Cell population

For the need of our experimental investigation of the interaction between a biological cell and an oscillating bubble, one single cell would be sufficient, while we were growing each

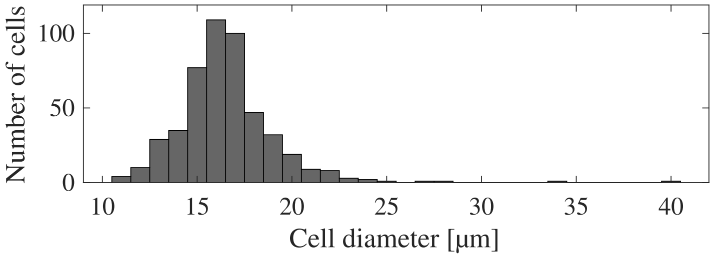

Figure 4.2: Counting of a typical sample consisting of 500 hundred cells issued from our population of megakaryocytes (MEG-01).

week millions of cells. The selection criterion in cell size, for ensuring a bubble-to-cell size ratio of 1:1, was so restrictive that finding one suitable cell was not effortless.

The megakaryocytes are described in literature as cells sizing in a very broad range from 10 to 100 µm [Levine et al., 1982]. This is one of the main reasons why these cells were chosen for the purpose of this work. Unfortunately, we scarcely observed such large cells. Actually, we think we did when the cells were still in culture, but once they were scrapped from the flask's bottom, brought out of their culture flask and transferred within the experimental tank, it is as if those few very large cells had disappeared. While the typical desired cell diameter was at least 50 to 60 µm, the most cells we could find were much smaller. It is likely that these large sought cells are fully mature megakaryocytes and may have therefore already planned out their apoptosis, a form of programmed cell death, with the view to serve their purpose, i.e. the release of their production of thrombocytes. In the scheme of things, the absence of very large cells once observed in the experimental tank could be explained by a stress induced by this preparation and transfer of cells, which could speed up their apoptosis.

From snapshots taken in the experimental tank, the equivalent diameter of about five hundred cells randomly hand-picked has been measured. The total count as a function of the cell diameter is given in figure 4.2, on which the cellular distribution presents a rather bell-shaped curve around a peak at 16 µm, with a couple events above 25 µm. Some rare cells larger than 40 µm could be found with some luck, but this was definitely not a generality. Throughout all our experiments, megakaryocytes larger than 50 µm have been found, twice.

Mycoplasma test

Mycoplasmas are part of the smallest known living-free organisms. They are bacterias typically sizing in the range 0.2-1 µm. Due to the absence of cell wall and the smallness of their genome, their capacity to live and grow is highly dependent on their possibility to take advantage of host cells, especially mammalian cells, and their nutrients. When a mycoplasmal infection happens, if this does not quickly lead to the destruction of the host cells, it can in many cases generate tumorigenesis, growth difficulties or changes in the metabolisms of host cells [Borchsenius et al., 2020]. With good laboratory and culture practices as well as recurrent detection tests, the apparition of mycoplasmas can be controlled. To that end, our cell line of megakaryocytes has endured such detection test, which was performed by the laboratory Anticorps Anticancer of the Centre de Recherche en Cancérologie de Lyon. The MycoAlert$^{\text{TM}}$ Mycoplasma Detection kit was employed. It takes advantage of the activity of enzymes of mycoplasma which is not present in healthy eukaryotic cells. When the MycoAlert solution is added to the culture sample, it reacts with the eventual mycoplasma's enzymes and causes the generation of ATP. The presence or the absence of mycoplasma is then evaluated by comparing the level of ATP before and after the addition of MycoAlert solution. The result of the detection test carried out on our MEG-01 cells line was negative. Our megakaryocytes are mycofree.

4.2 Methodology

4.2.1 Experimental setup

Figure 4.3 depicts a schematic of the experimental setup, which barely differs from the one employed for the visualization of the dynamics of nonspherical shape modes. For welcoming the cellular population, the content of the tank is replaced by cell culture medium (Dulbecco's Modified Eagle Medium DMEM, high glucose, without L-glutamin) preheated in an incubator at 37 °C. We noticed that the longer the culture medium was kept in the incubator, the more the gas concentration decreased and that our bubbles were less prone to grow by rectified diffusion. When the medium was kept too long in the

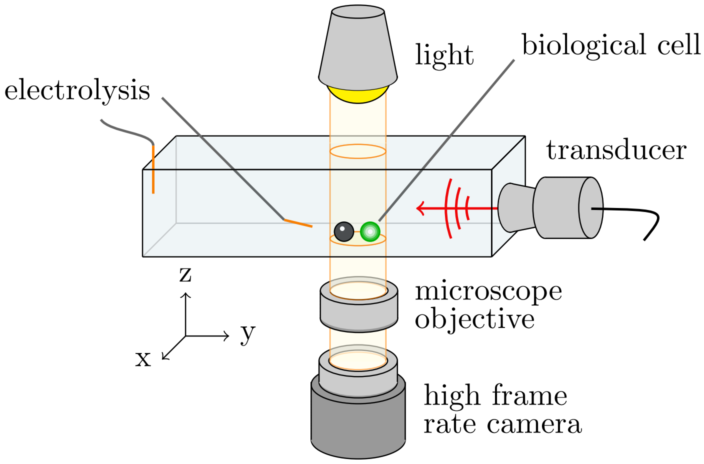

Figure 4.3: Schematic representation of the experimental setup.

incubator, bubbles dissolved very quickly in such a poorly (not measured) gassed medium, even when no ultrasound was activated. In the opposite case, bubbles had a tendency to grow indefinitely by rectified diffusion, until occupying all the microscope field of view and that imaging nearby cells became impossible. A right balance was difficult to achieve. At a first glance, it appeared empirically that the best conditions of bubble size stability were obtained for an incubating time about 6 to 8 hours. Once the DMEM and the cells were poured into the tank, it quickly cooled and reached, after approximately three hours, a temperature of about $26.7 \pm 0.5\,^{\circ}\mathrm{C}$ without going lower for the rest of the day. The microscope lamp was very likely responsible for this asymptotic value higher than the room temperature.

For the observation of the interaction between a megakaryocyte and a microbubble at the acoustic time scale, the transducer is driven at the frequency of its third harmonic, which is 85 kHz (see figure 2.3). As a reminder, it allows to approach an approximate 1:1 sizing ratio between a resonant microbubble and a large megakaryocyte. The visualization with an inverted microscope of such a micrometric cell through a 50 mm height tank filled with cell medium made the question of light critical. The amount of light was restricted by the need for a short exposure time, the 20× magnification objective lens allowing to achieve an adequate image scale of 1 µm/pixel and a frame rate inevitably superior than twice the driving frequency. All these limitations left no other choice but to work with a frame size of 136 x 128 pixels, or equivalently 136 x 128 µm, and thus with a couple of cell and bubble that fitted the frame size. As a consequence, the frame rate was limited to a maximal value of 177 215 Hz, yet sufficient to describe the 85 kHz oscillations.

4.2.2 Mechanical characterization of cell culture medium

With the view to learn more about what we were dealing with and what to expect in terms of modal behaviors of an ultrasound-driven bubble immersed in the DMEM, the characterization of the medium is required. Information about its mass density and surface tension were lacking on the manufacturer's website. The sparse literature contains some works that explore the surface tension of few cell mediums eventually added with fetal bovine serum for optimization purposes of computational fluid dynamics analysis [Hinderliter et al., 2010, Poon, 2020] or added with polymers in order to monitor intracellular biomolecules in living cells [Lin et al., 2014]. In any cases, their measurement is performed at 37 °C. Because these information could not be found for our experimental case of pure DMEM at room temperature, we undertook to measure these quantities. The mass density of DMEM was easily obtained with a density meter (Anton Paar, DMA 35). At 21.2 °C, DMEM weights $1.0064 \times 10^{3}\,\mathrm{kg \cdot m^{-3}}$. For quantifying its surface tension, an optical tensiometer (Biolin Scientific, Attension Theta Lite) has been employed. Operating with an internal software, it requires an information about the dynamic viscosity of

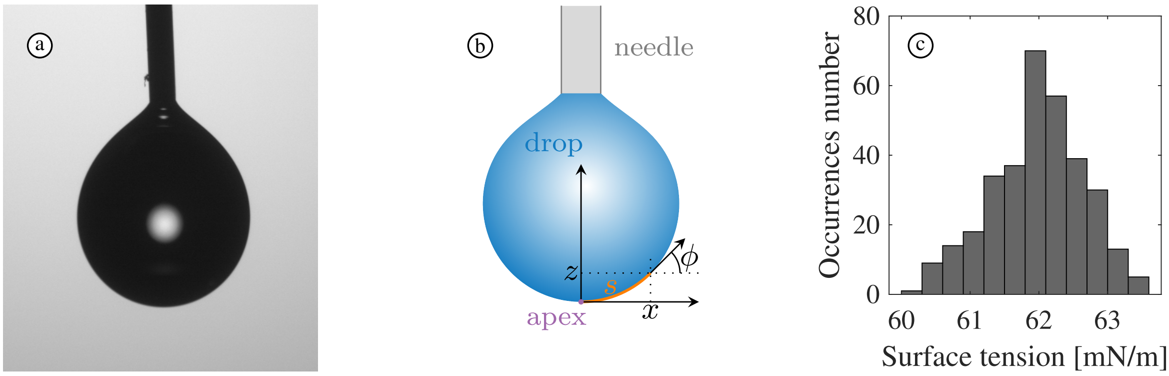

Figure 4.4: (a) Experimental snapshot of a DMEM pendant drop. (b) Geometry of the system under study. (c) Distribution of the measurements of surface tension.

the DMEM at 20 °C that is set to 959.8 mPa · s according to Hinderliter et al. [2010]. The system optically evaluates the shape of a drop suspended at the tip of a needle. From a snapshot such as the one given in figure 4.4a, the software recovers a value of surface tension γ [Lauren, 2017] by applying the following expression inspired from Tate's law on the drop coming out of a dropper

$$\gamma = \frac{\Delta\rho\, g\, R_0}{\beta}, \tag{4.2}$$

where $\Delta\rho$ is the difference of density between the air and the fluid to characterize, g is the gravity constant, R_0 is the drop radius of curvature at the apex and β is a parameter related to the drop shape. It can be calculated with these three differential equations

$$\frac{dx}{ds} = \cos\phi, \quad \frac{dz}{ds} = \sin\phi, \quad \frac{d\phi}{ds} = 2 + \beta z - \frac{\sin\phi}{x}, \tag{4.3}$$

where x, z, s and ϕ are defined such as depicted in figure 4.4b. The set of values obtained for the surface tension are gathered in figure 4.4c in the form of a histogram, showing a normal distribution around a peak value of 62 mN · m^{-1}. The variability might be explained by the absence of an antivibration system beneath the tensiometer. The pendant drop was apparently vibrating on the video acquisition. In the forthcoming of this manuscript, the surface tension of DMEM is set to a mean value of 62 mN · m^{-1}. For reference, the surface tension of water at 20 °C equals 72.8 mN · m^{-1}.

4.2.3 Image processing

The image processing method that concerns the bubble is the same as the one briefly described in section 2.2.1. Due to a weak contrast of the image of cells, the post-processing part concerning them differs. The method summarized as a block diagram in figure 4.5 is performed as follows. Before starting the extraction of the cell contour, a noisy mask is applied on the bubble. Only remaining the cell to be treated, the image is thresholded in order to uniform the shades of dark gray that constitute the image of the cell. Then, a low-pass filter is applied in order to reduce the noise present in the whole image and slightly smooth the cell contour, before applying a minimization algorithm for detecting the areas of similar gray shade. The area corresponding to the cell is selected on the basis of its previously manually located centroid. The image is finally binarized and undergoes a cell contour extraction procedure similar to that applied to the bubble.

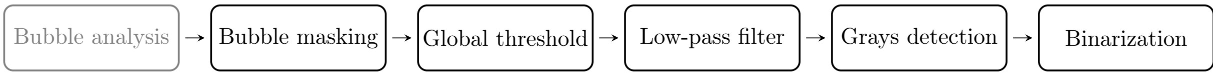

Figure 4.5: Block diagram of the image processing method for extracting the coordinates of the biological cell contour.

4.2.4 Cell fastening

In order to investigate the bubble-cell interaction through several parameters, and especially as a function of the bubble-cell distance, there is a need of controlling the position of the cell with respect to the bubble attached at the tank's bottom. The first idea was to fasten the cells to a glass capillaries by aspiration, facilitating thereafter its fine displacement thanks to a micromanipulator and the study of a same bubble-cell couple with an adjustable interspace.

Manufacture of a glass capillary

Home-made glass capillaries could be manufactured at low cost thanks to a micropipette puller (Sutter Instrument® P-1000). Borosilicate glass capillaries (World Precision Instruments, 1B100-4, 1 mm outer diameter, 0.58 mm inner diameter) were chosen to fit the capillary holder (Narishige, HI-9). The difficulty with a pipette puller is to find a functional recipe to create adequate capillaries, especially when the desired result is somehow exotic and not referred in the manufacturer's pipette cookbook [Sutter Instrument, 2018]. While the puller has integrated premade recipes for preparing ready-to-use patch or injection pipettes of 1-3 µm, fabricating capillaries with a larger tip may necessitate a manual scoring and breaking of the sealed glass tip in a post-pulling stage. A so-called "glass-on-glass" procedure is laid out in large detail in the cookbook and will not be further discussed here. Starting from recipes given in the cookbook, the pulling parameters were empirically adjusted so that it fitted our 1B100-4 capillaries. Capillaries of inner diameters (ID) about 6-8 µm (without manual scoring) and 14-20 µm (with manual scoring) were successfully obtained. The recipe parameters are summarized in table 4.1.

Resulting ID	Ramp	Heat	Pull	Velocity	Time	Pressure	Scoring
6-8 µm	492	502	15	15	120	500	no
14-20 µm	492	522	0	150	0	200	yes

Table 4.1: Recipes to use with the P-1000 micropipette puller in order to obtain 6-8 µm and 14-20 µm inner diameter (ID) glass capillaries, without and with a post-pulling manual scoring procedure, respectively.

Cell microaspiration

The cell microaspiration is accomplished thanks to a glass capillary, a flexible hose filled with cell medium and a syringe (Hamilton Gastight® 1710). Filling the hose with cell medium has a twofold objective. First of all, it ensures a correct ionic balance all around the cell, inside the capillary and elsewhere in the tank. Second, it improves the control of the applied depression, thanks to the weak compressibility of the liquid compared to air and thus a larger range of pressure, unlike when filled with air and that the maximum displacement of the piston caused insignificant pressure change. Due to the presence of a stiff zona pellucida, the attachment to a glass capillary by microaspiration worked relatively well for the case of oocytes. A same method has been attempted at many times with megakaryocytes with differently sizing glass capillary (manually scored or not) and unfortunately led to failings only. The megakaryocytes, much less resistant than oocytes, were most of them finishing completely lysed. When this was not the case, the few surviving specimens were observed to rapidly reorganize themselves within the capillary in a few minutes, even before a bubble could have been nucleated and tethered to the substrate. A plastic-like behavior is clearly evidenced when the cell is expelled from the capillary, as photographed in figure 4.6. After release, the cell retains its plastic deformation for several minutes before slowly regaining its original spherical shape. These observations led to the conclusion that this cell fastening technique by aspiration was not adequate for megakaryocytes, which are too fragile or too motile.

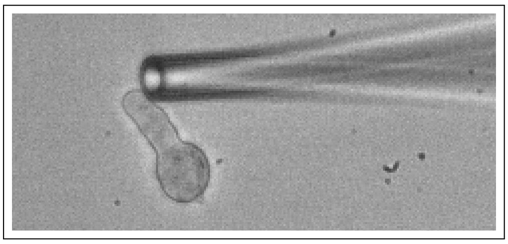

Figure 4.6: Image of a plastically deformed megakaryocyte after having been maintained by microaspiration through a capillary for a few minutes and then released.

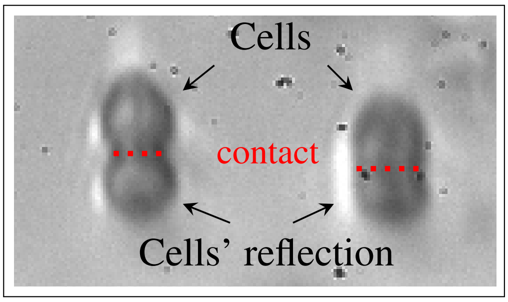

Figure 4.7: Side-view of two substrate-adhering megakaryocytes, letting their reflections appear on the substrate.

Cell tethering

Unable to fasten megakaryocytes by means of glass capillaries and cell aspiration, an alternative method had to be found. At the same time as certain megakaryocytes were attempted to be aspirated, we noticed that all the other cells quickly sedimented and had an ability to adhere to the bottom of the tank while keeping a relatively circular shape. Images of cells were taken in a side-view configuration so that their position on the substrate could be acknowledged, whether they adopt more like a super-hemispherical or a sub-hemispherical shape. A typical example of substrate-adhering megakaryocytes is displayed in figure 4.7. When this snapshot was taken, the cells had been poured in the tank for more than three hours. After a rapid sedimentation, they began to adhere to the substrate and maintained such a super-hemispherical shape for hours. This is obvious in figure 4.7 on which two typical megakaryocytes and their reflection on the substrate are visible. The way our cells are super-hemispherically standing on the substrate gives us a possibility for placing it in a face-to-face position with a wall-attached bubble. Yet, the poor image quality of figure 4.7 asserts the interest of imaging the cell, and therefore the bubble, under a microscope and therefore in a top-view configuration.

In conclusion, throughout this thesis work, the tethering of oocytes will be accomplished by aspiration through a glass capillary, and in the case of megakaryocytes, by sedimentation and natural substrate-attachment.

4.2.5 Characterization of the cell deformation

Since both microbubble and cell are visualized under a microscope, their dynamics are investigated from their top-view contour. With that in mind, geometrical indexes had to be defined in order to evaluate their respective motion. Concerning the microbubble, its modal behavior is determined following the modal analysis of its contour described in chapter 3. Concerning the cell, it needs more than one geometrical variable in order to differentiate and quantify its overall dynamics that is actually characterized by a solid-body translation and a deformation. In that respect, two geometrical quantities are defined. The first one is the close-to-bubble (CtB) cell's point, which is the point of the cell membrane that is the closest to the bubble, as illustrated in figure 4.8a. The cell deformation and the bubble pushing-pulling action were already experimentally investigated by van Wamel et al. [2004] and Wang et al. [2018], and theoretically by Guo et al. [2017] using the excursion of this point. However, due to the rather super-hemispherical shape of the adhering megakaryocyte, it also undergoes an important translation motion, which tends to diminish the cell deformation. To distinguish these two kinetic responses, translation and deformation, a second index, the so-called cell strain, which is defined as the ratio of the in-axis cell diameter to its orthogonal diameter, as illustrated in figure 4.8b, is also taken into consideration. These two indexes are observed with respect to the bubble modal amplitudes and the displacement of the close-to-cell (CtC) bubble's point, which is reciprocally the point of the bubble contour that is the closest to the cell membrane. If the bubble is significantly larger than the cell, one can suspect that this point defined in a two-dimensional perspective is no longer the bubble interface point closest to the cell membrane in the three-dimensional perspective. This confirms the need for cells and bubbles to have comparable sizes. Also, it should be noted that, if the bubble is animated by a shape mode, as soon as the displacement anti-node of the nonspherical deformation does not occur in front of the cell, it is possible that this CtC bubble's point

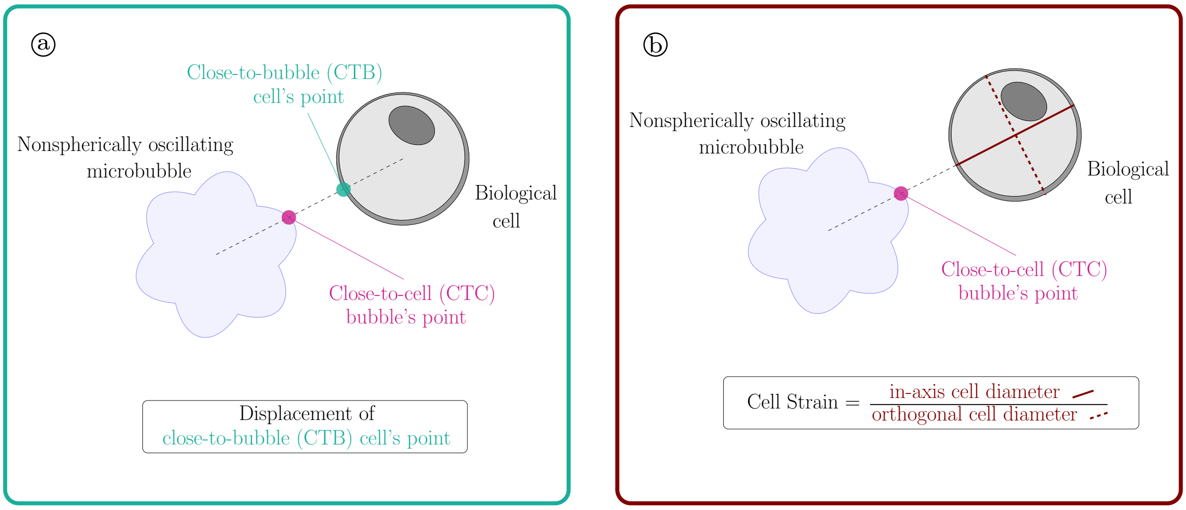

Figure 4.8: Visual description of the geometrical indexes employed for describing the mechanical cell response with respect to the bubble dynamics and the displacement of the close-to-cell (CtC) bubble's point, which is the point that belongs to both the bubble surface and the center-to-center segment. (a) The displacement of the close-to-bubble (CtB) cell's point, which is the point that belongs to both the cell membrane and the center-to-center segment. (b) The evolution of the cell strain is the ratio of the in-axis cell diameter to the orthogonal cell diameter. The color code employed here is kept in the figures of section 4.3.2 investigating the bubble-cell interaction at the acoustic time scale.

would not correctly reflect the bubble deformation responsible for the cell response. We make this informed choice of definition, while knowing that this geometrical parameter, more impacted by a not controlled angle of the nonspherical mode than are the others, is also less engaging on the characterization of the cell response.

4.3 Bubble-cell interaction

4.3.1 Single bubble behavior in cell medium

Similarly as in chapter 2, the emergence of bubble shape modes has been investigated as a function of the acoustic pressure, as depicted in figure 4.9. Sectoral modes are privileged in this configuration for which degrees $n = 3$, $n = 4$ and $n = 5$ were experienced. The resonance of the radial oscillation appears to meet the resonance of the modal degree $n = 4$, at very low acoustic pressure. At a first glance, sectoral modes of degree $n = 5$ have exclusively been experienced off resonant radius, but that's without taking into account the fact that too large bubbles, and hence too spread out bubble-cell couples (too large for the imaging frame) were actually out of investigation. This is why no bubble of radius larger than 47-48 µm was investigated. In definitive, bubbles basically behave similarly as in water, with an expected shift in resonance, as obviously expected due to the change in the driving frequency, and as predicted by the Francescutto curves drawn in solid lines in figure 4.9. These curves were implemented with the physical parameters measured in section 4.2.2.

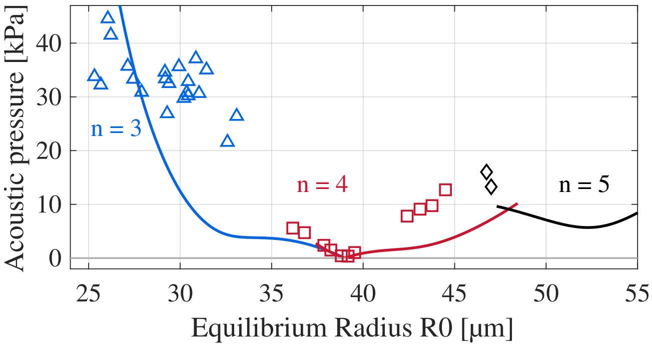

Figure 4.9: Instability thresholds of sectoral modes (subharmonic frequency = 42.5 kHz) as a function of the bubble equilibrium radius for modal degrees $n = 3$, $n = 4$ and $n = 5$. Experimental wall-attached bubbles (geometric markers) are compared with free bubble theory (solid lines), according to Francescutto and Nabergoj [1978].

4.3.2 Bubble pushing-pulling action

The pushing-pulling action of a microbubble has proven its capacity for sonoporating the membrane of biological cells [van Wamel et al., 2004, Wang et al., 2018]. This was performed with adhering epithelial cells and spherically oscillating microbubbles. As far as we are aware, this has never been experienced or described theoretically at the single-cell scale for a bubble undergoing nonspherical shape modes. Thence, we investigate throughout this section the generation of cell deformations in presence of a nearby bubble undergoing nonspherical modes. The focus is done on sectoral modes of degree $n = 3$ and $n = 4$, although tesseral modes of order $m = 1$ and $m = 2$ have been experienced too. The modulation of the driving signal with a triangle-shaped envelope (modulation frequency $f_m = 25\,\text{Hz}$) allows to encounter different bubble modal configurations for

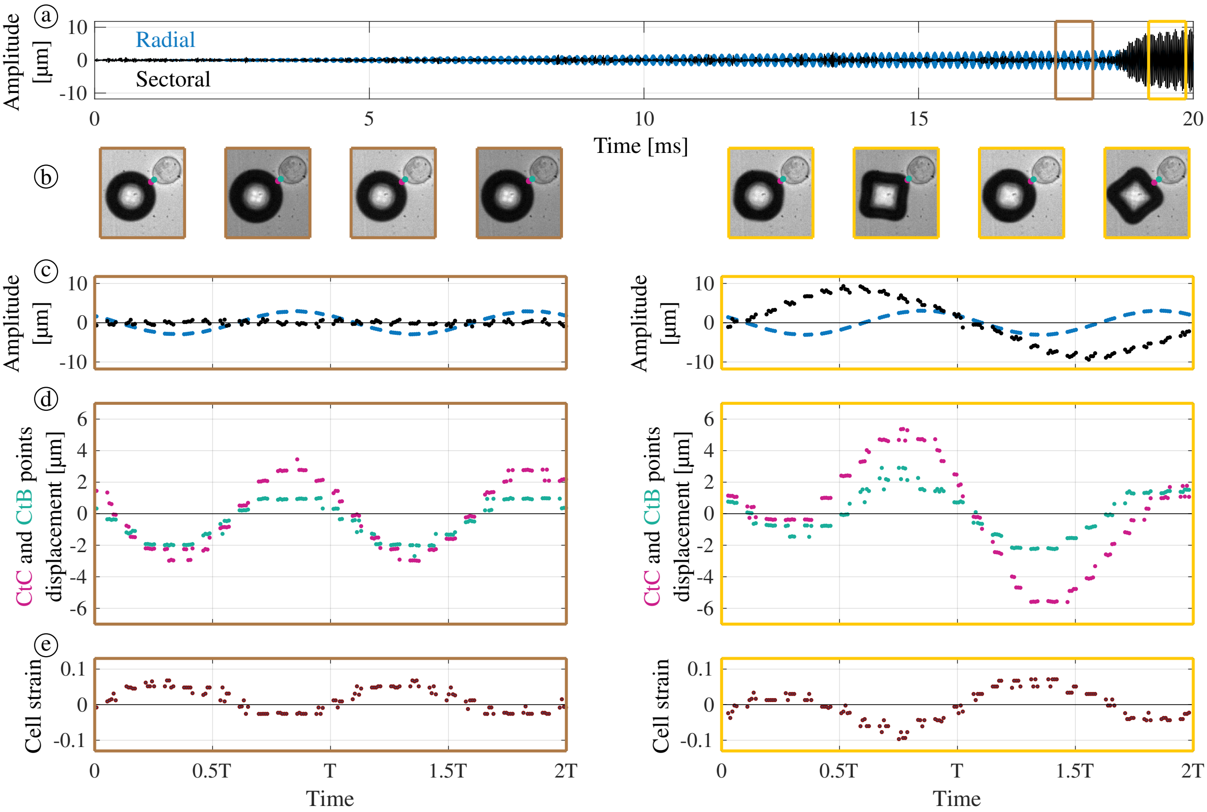

Figure 4.10: Mechanical response of a cell of diameter $c_\varnothing$ ~43 µm to a subharmonically oscillating microbubble animated by a sectoral mode $n = 4$. The center-to-center distance between both cell and bubble is about ~67 µm. Two regions of interest are highlighted by colored areas along the increasing pressure ramp (a), in a way to have two scenarios of bubble dynamics, a radial motion only (left) and an additional sectoral mode (right). Snapshot series at the acoustic time scale (b). Zooms on the modal amplitudes of radial and sectoral modes (c), the CtC bubble's and CtB cell's points displacement (d) and the cell strain evolution (e), subtracted by their value at rest, in which the data are refolded over two acoustic periods.

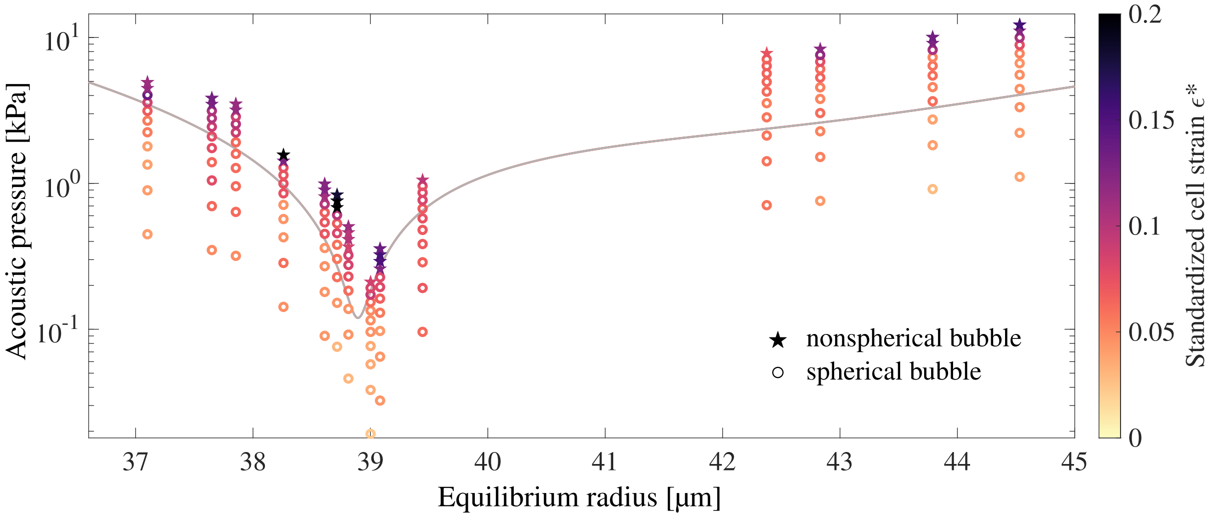

Figure 4.11: Standardized cell strain $\epsilon* = \frac{(D_{cc}-R_0)}{R_0}\epsilon$ induced by the pushing-pulling action of a bubble undergoing a sectoral mode $n = 4$ and investigated as a function of the bubble radius and the increasing acoustic pressure.

similar experimental parameters: bubble and cell distance and sizes. The acoustic field is considered to be of constant amplitude when the observation of the bubble-cell pair is limited to around a hundred experimental points, as accomplished in figure 4.10. Two instants along the 20 ms increasing pressure ramp are defined so as to dissociate two experimental configurations: a bubble oscillation on a radial oscillation only and the presence of an additional sectoral mode $n = 4$. By refolding on two acoustic periods, the bubble modal content can be correlated to the CtB cell's point and the cell strain ϵ. When regarding at the cell response in presence of the sectoral mode, the dynamics of the CtB cell's point exhibits an evident subharmonic behavior. It illustrates perfectly the importance of the phase relation between modes, given that while the sectoral amplitude reaches 10 µm, the bubble surface displacement, counterbalanced by an out-of-phase radial oscillation, barely reaches a 5 µm maximal excursion for a 3 µm maximal displacement of the CtB cell's point. Concerning the strain, the cell meets twice more peak-to-peak amplitude with the emergence of the sectoral mode.

Among the whole experimental data set, this example of bubble-cell pair is one of the most intense in terms of cell deformation. This is explained by the particularly important proximity of the bubble to the cell. The cell deformation caused by the sectoral mode $n = 4$ decreases faster with the bubble-cell distance than that induced by the radial oscillation. At long distance, the cell periodically pushed and pulled by the bubble undergoing a radial and a sectoral mode only exhibits a strain oscillating at the driving frequency. At short bubble-cell distance, the cell experiences a subharmonic strain in addition to the radial contribution. To interpret this, one can consider the cell in the acoustic far-field area of the microbubble, and the radial mode as a monopole source oscillating at the

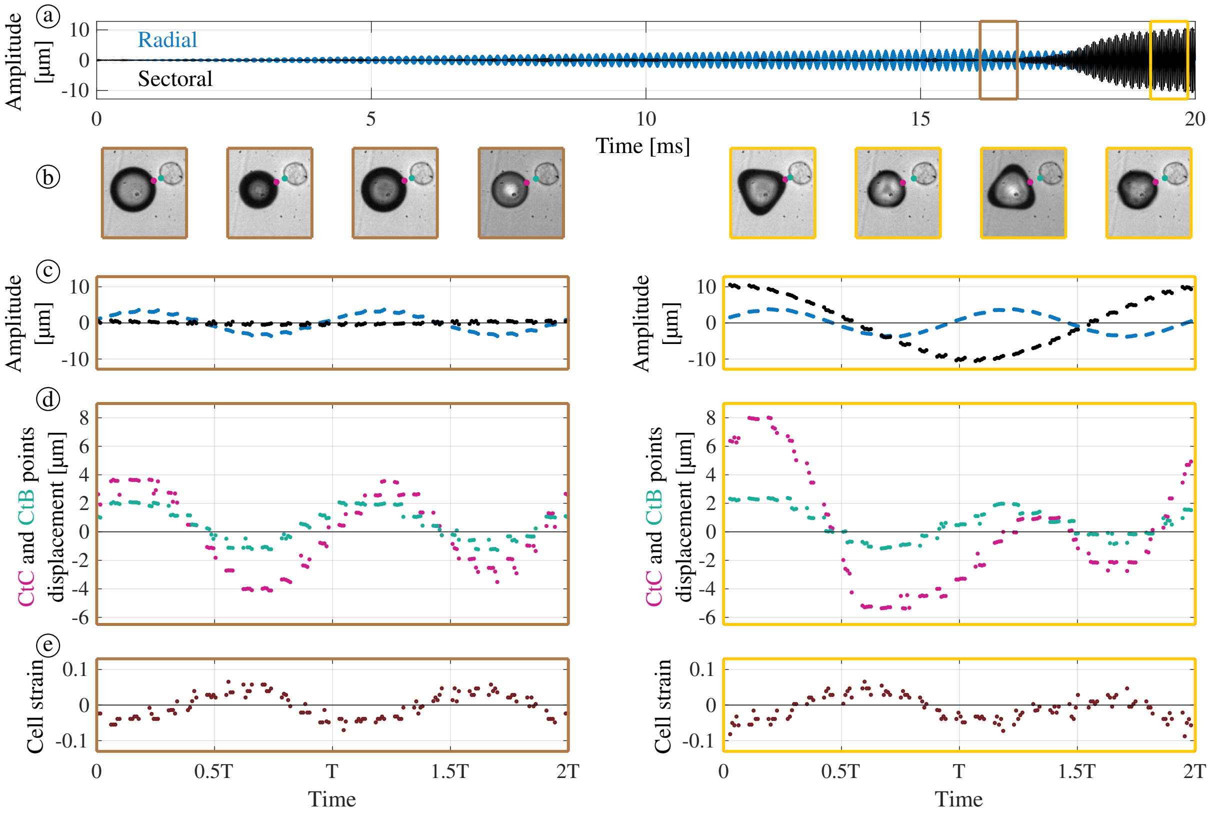

Figure 4.12: Mechanical response of a cell of diameter $c_\varnothing$ ~18 µm to a subharmonically oscillating microbubble animated by a sectoral mode $n = 3$. The center-to-center distance between both cell and bubble is about ~62 µm. Two regions of interest are highlighted by colored areas along the increasing pressure ramp (a), in a way to have two scenarios of bubble dynamics, a radial motion only (left) and an additional sectoral mode (right). Snapshot series at the acoustic time scale (b). Zooms on the modal amplitudes of radial and sectoral modes (c), the CtC bubble's and CtB cell's points displacement (d) and the cell strain evolution (e), subtracted by their value at rest, in which the data are refolded over two acoustic periods.

fundamental frequency with an omnidirectional far-field directivity and a power radiation greater than that of a sectoral mode.

All experimental occurrences, where a bubble oscillating on a sectoral mode $n = 4$ only has been seen interacting with a cell, are summed up in figure 4.11. Therein the cell strain is described as a function of the bubble radius R_0 and the acoustic pressure. Due to a large range of values, the y-axis is presented on a logarithmic scale. To take consideration of all parameters, the cell strain ϵ is standardized as $\epsilon* = \frac{(D_{cc}-R_0)}{R_0}\epsilon$, where D_{cc} is the center-to-center bubble-cell distance and ϵ is the cell strain as defined in figure 4.8b. As a reference, the theoretical instability threshold curve for free bubble [Francescutto and Nabergoj, 1978] is displayed in solid gray line. Figure 4.11 highlights the sectoral mode contribution to the total cell strain. Even if the radial oscillation can by itself cause a significant cell strain, the sectoral mode brings also an important participation, making

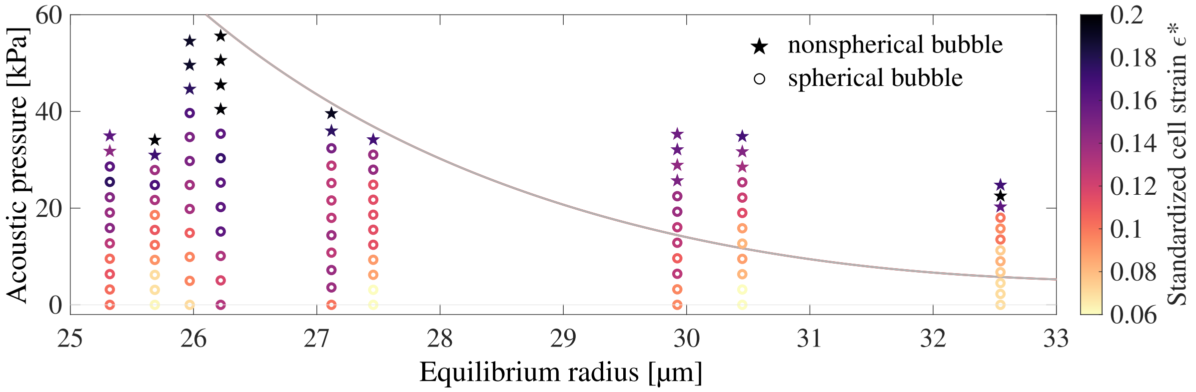

Figure 4.13: Standardized cell strain $\epsilon* = \frac{(D_{cc}-R_0)}{R_0}\epsilon$ induced by the pushing-pulling action of a bubble undergoing a sectoral mode $n = 3$ and investigated as a function of the bubble radius and the increasing acoustic pressure.

the cell strain leaping high out of its uniform growth (along the increasing amplitude pressure) which would have occurred in the absence of the sectoral mode.

A similar study of the cell response has been performed in the case of smaller bubbles undergoing a sectoral mode of degree $n = 3$. An example is given in figure 4.12. Despite similar modal amplitudes as in the sectoral mode $n = 4$ example, the subharmonic contribution in the cell strain is weak. A different phase shift than in the case of the sectoral mode $n = 4$, leading to a synchronization of the modal maximal deformations, would let think that such a strong 8 µm amplitude displacement of the CtC bubble's point would promote an important cell strain, through a kind of constructive interference. In the contrary, it rather seems that the cell strain was even stronger at the time the bubble dynamics was only radial.

When all experimental occurrences of bubble-cell interaction in presence of a sectoral mode $n = 3$ are gathered and displayed as before in a single representation, it results what is depicted in figure 4.13. High cell strains are not necessarily related to nonspherical bubble deformations. It helps but it is not a *sine qua non* causation.

4.3.3 Shear waves propagation

The elasticity of a biological tissue highly depends on its structure and state of health. While methods for measuring it at the macroscopic level do not lack and are already applicable in the medical field [Sarvazyan et al., 2011], its transportation at the microscopic level leads to complications. One reason is the complexity of the high-frame rate tracking of possibly large wavelengths in a micrometric object.

Shear stresses in a viscous medium can be calculated by retaining the gradient of the displacement field. The different ways for inducing shear stresses in biological cells

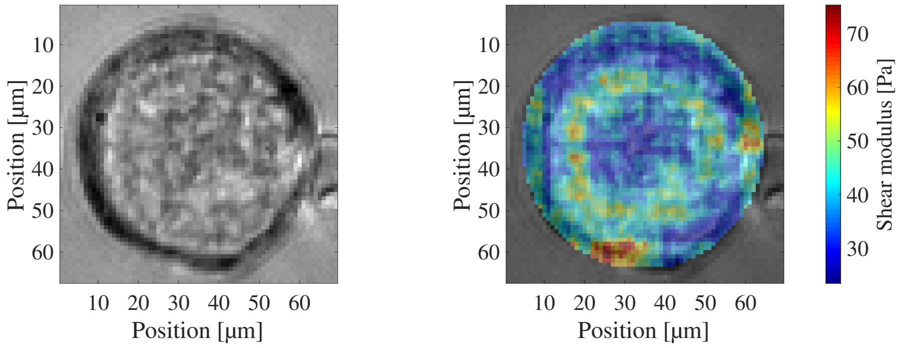

Figure 4.14: Snapshot of a megakaryocyte of about 60 µm diameter (left) and its shear modulus map obtained by elastography through the action of a microbubble animated by a radial oscillation and a sectoral mode $n = 4$, in a 85 kHz acoustic field (right).

especially differentiate in their necessity to access the region of interest or not. Elasticity maps in an oocyte have already been observed in real time thanks to the action of a 15 kHz-oscillating glass capillary brought in contact with the cell [Grasland-Mongrain et al., 2018]. If the access is difficult such as within *in-vivo* environments, the remote action of ultrasound could be a noninvasive and localized solution for generating shear stress. As any wave attenuates when propagating through a dissipative medium, there exists an upper critical frequency above which shear waves encounter an evanescent behavior and are not able to propagate in a medium. In this way, propagating shear waves were recently observed in a gelatin phantom until a frequency of 20.4 kHz [Laloy-Borgna et al., 2021]. If the objective is to image a deep position in a tissue, hard to reach due to dissipation, ultrasound-driven microbubbles could make things easier. As far as we are aware, cellular elastography with microbubbles has never been reported in literature and we propose in this section first evidences of feasibility, whereas these mentioned experimental works give us confidence in the possibility of inducing shear waves in megakaryocytes with microbubbles.

An optical image of an investigated cell and a resulting elasticity map are given in figure 4.14, the latter being obtained with the kind collaboration of Sibylle Grégoire and Gabrielle Laloy-Borgna. This was performed using an 85 kHz acoustic field of constant amplitude. While one would have thought that the use of such a high frequency would not have allowed to propagate acoustic waves, it turned out experimentally that the little amount of energy transmitted into the cell was actually sufficient to perform an elasticity measurement. This elasticity map has been computed using an algorithm adapted from Grasland-Mongrain et al. [2018] based on a Helmholtz decomposition of the two-dimensional displacement field. The divergence-free part is directly connected through the classical wave equation to the propagation speed of shear waves, and hence to the shear modulus, by considering the cell as a linear, infinite (compared to shear wave wavelength) and isotropic medium. Experimentally, the displacement field is obtained by particle imaging velocimetry (PIV) analysis, and the shear wave speed with a passive elastography algorithm. Briefly, this algorithm consists in applying to each pixel a temporal cross-correlation with all other points. The analysis of the resulting focal spots and their curvature informs on the shear wave wavelength and thus on its propagation speed.

By assuming in the whole megakaryocyte a constant density of $1.1\,\mathrm{mg \cdot cm^{-3}}$ [Nakeff and Floeh, 1976], an information of shear elasticity can be recovered. It appears in figure 4.14 that the cell is characterized following the radial direction by three successive layers of different elasticity. This can be hard to interpret given that it is unclear where the imaging focal plane locates with respect to the cell, close to the contact, at its equator or higher in elevation. Nevertheless, an interpretation for this variation in elasticity is suggested in the following. The presence of a circular area of higher shear modulus (about 50-70 Pa) can be explained by the tethering. At a first glance, if there is cellular attachment, the elasticity measured in the region of the contact is higher because of a densification of its cytoskeleton due to the formation of actin-based connections with the substrate. From a top-view perspective, due to the super-hemispherical shape of the cell (see figure 4.7), this tethering-induced stiffening appears as a circular area, following the contact line, located half way between the center and the edge of the cell two-dimensional projection in the (x,y) plane.

Unlike previously where it was necessary to sufficiently approach the bubble towards the cell in order to induce membrane deformations, this elastography method is based on the assumption of induced diffuse waves. Consequently, a short bubble-to-cell distance is not necessary, and is even rather to be avoided, at the risk of generating guided waves. In fact, the close location of the microbubble with respect to the biological cell and the presence of largely predominant harmonic and subharmonic oscillations can be responsible for artifacts in the elasticity map. The exemplary case chosen in figure 4.14 reveals such an error resulting in values of shear modulus that locally reach fallacious magnitudes higher than elsewhere, going beyond 70 Pa.

In conclusion, the shear modulus of this megakaryocyte has been measured to be about 25-35 Pa, although the tethering can locally induce an increase of the cellular stiffness, up to 50-60 Pa. Higher values are associated to artifacts only.

4.3.4 Cells in streaming

Tumbling cells

In this section, the cells and their dynamics are no longer investigated tethered but in suspension in the medium. As the bubble experiences a nonspherical mode and induces streaming in its vicinity, it appeared that the nearby suspended cells showed a strong

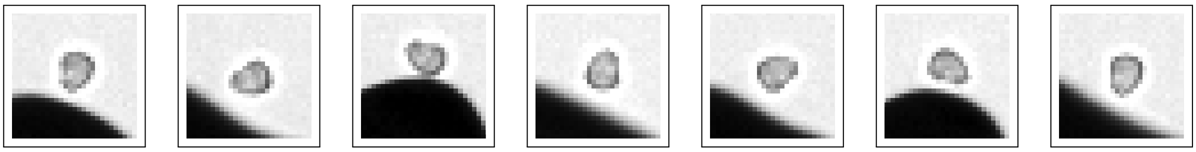

Figure 4.15: Snapshot series of a tumbling cell in the vicinity of a bubble undergoing a sectoral mode of degree $n = 5$ under the action of a 30.5 kHz acoustic field.

tendency to be trapped on what could be the stagnation points of the recirculation loops and to spin on itself. This behavior was already reported in literature for the case of lipid vesicles [Marmottant et al., 2008, Pommella et al., 2015]. In these works, a deformation of the vesicle membrane was also observed on the side of the vesicle near the bubble, all the more important as the vesicle was elastic. Such asymmetric deformation has not been experienced for our case of tumbling megakaryocytes, which only encounter a rigid-body rotation, as illustrated in figure 4.15, for the case of a 20 µm diameter cell in the vicinity of a bubble undergoing a sectoral mode $n = 5$. The induced streaming at the equator is mainly azimuthal (no longitudinal dependency). Thence, the cell tumbles around the z-axis, at a location halfway between an anti-node and a node of the bubble interface displacement. This motion occurs at the fluidic time scale and not at the acoustic time scale, since it is carried out by the streaming. The cell's initial position of the first snapshot is recovered in the seventh snapshot (see figure 4.15). Because a duration of 0.5 ms separates each snapshot, the angular velocity of the cell can be approximated in this case to be about $2\pi/3\,\mathrm{rad} \cdot \mathrm{ms}^{-1}$. It should be noted that the observation is done here with the 10× magnification microscope objective lens, hence an image scale of 2 µm/pixel.

The example given in figure 4.15 was an exemplary case. When all our results are gathered in a single representation, it results what is depicted in figure 4.16a. A relation between tumbling velocity and cell diameter can be drawn, for which larger cells are

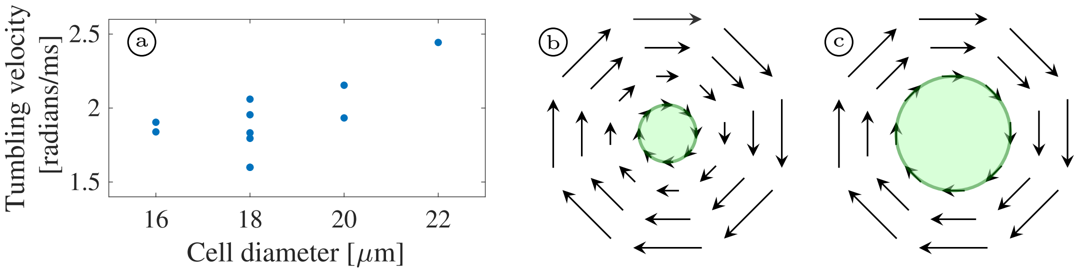

Figure 4.16: Relation between the size of a megakaryocyte and its tumbling velocity while trapped on the stagnation point of a streaming recirculation loop induced by a bubble sectoral mode of degree $n = 5$. The experimental results (a) are schematically explained (b-c): The larger is the cell, the greater is the streaming velocities applying on its surface, and thus so is the cell tumbling velocity.

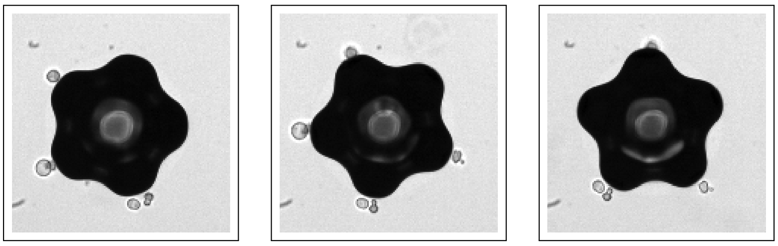

Figure 4.17: Snapshots of a bubble undergoing a sectoral mode $n = 5$ and rotating in a clockwork motion. The tumbling cells trapped in the stagnation points follow the bubble interface as it rotates.

associated to higher tumbling velocities. The point of stagnation, characterized by a zero flow velocity, is located at the center of closed streamlines. As one moves radially away from this point of stagnation, the velocity field grows in magnitude. If the cell is indeed trapped on a stagnation point, the velocity field that applies on its surface thus grows with the cell radius, due to an increased distance from the stagnation point but also to an extended cell surface on which the fluid can apply stresses and make the cell tumbling. This point of view is schematized in figures 4.16b and 4.16c where two cells of different size are schematically placed on the stagnation point of similar streaming fields. The resulting torque is necessarily greater when the cell is larger, which may explain the correlation between cell size and tumbling velocity displayed in figure 4.16a.

In addition to this tumbling motion, it is worth noting that we experienced rotating sectoral modes. This had already been reported in literature by [Mekki-Berrada et al., 2016], in the case of bubbles flattened between two elastic walls, who measured a constant angular velocity of about 0.5 revolution/s for every modal degrees. In our experimental configuration, the direction of rotation may change and the angular velocity is not constant, quite the contrary, as it may actually vary in a broad range of 0-0.8 revolution $\cdot$ s^{-1}. The underlying causes for these changes in direction and variations in velocity remain so far unknown. An example of a rotating sectoral mode $n = 5$ in a clockwork motion is given in figure 4.17 where tumbling cells are visible. They maintain their constant position relatively to the bubble nonspherical deformation and describe then a sort of spiral motion all along the bubble oscillation and rotation.

Flowing cells

When the cells caught in the streaming and being attracted towards the bubble do not encounter a possibility for being trapped on a stagnation point near the bubble interface, or when the trapped cells leave their position under the action of a disruptive event, e.g. a collision with another cell or an abrupt change in the bubble dynamics, they can be subject to a bubble-induced projection in a one-way outward movement, following the equatorial

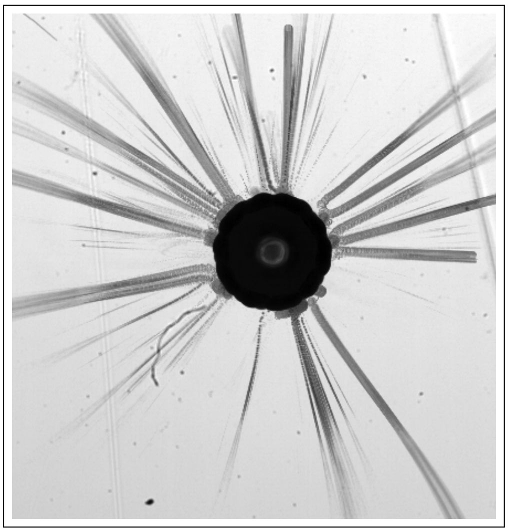

Figure 4.18: Flowing cells around the same microbubble as illustrated in figures 4.15 and 4.17, simultaneously animated by a sectoral mode $n = 5$ and a rotational motion. The cells are arriving out-of-focus from above the bubble and are then propelled by the bubble displacement anti-nodes located at the equator, in a one-way outward movement.

plane, which is also the focal plane, as a reminder. An example given in figure 4.18 reuses the same bubble as the one illustrated in figures 4.15 and 4.17. The cells follow the antifountain-like streaming motion induced by the bubble sectoral mode, arriving out-of-focus from above the bubble and leaving it from its displacement anti-nodes located at the equator.

4.3.5 Fluorescent particles internalization

Propidium iodide

Propidium iodide (PI) is a fluorescent agent, with excitation maximum of 493 nm (green-blue) and emission maximum of 636 nm (red), that binds to nucleic acids, e.g. DNA and RNA contained in biological cells, by intercalating between the bases. Its inability to penetrate an intact membrane makes it commonly used to assess cellular membrane integrity and cell viability, when binding to RNA contained in the cytoplasm. On the same basis, this makes PI an adequate fluorescent marker to evaluate the impacts, reversible or not, of mechanical stresses on a biological cell and its membrane. When PI does enter the cytoplasm and binds to RNA, its excitation and emission spectra encounter a frequency shift, resulting in fluorescent excitation maximum of 535 nm (green) and emission maximum of 617 nm (orange-red). Therefore, the PI suspended in the aqueous solution and the internalized PI differentiate by their emission frequency, but also by their emitted light intensity. When bound to acid nucleic, the PI's quantum yield, i.e. the ratio of emitted photons to absorbed photons, becomes multiplied by 20 to 30. With controlled

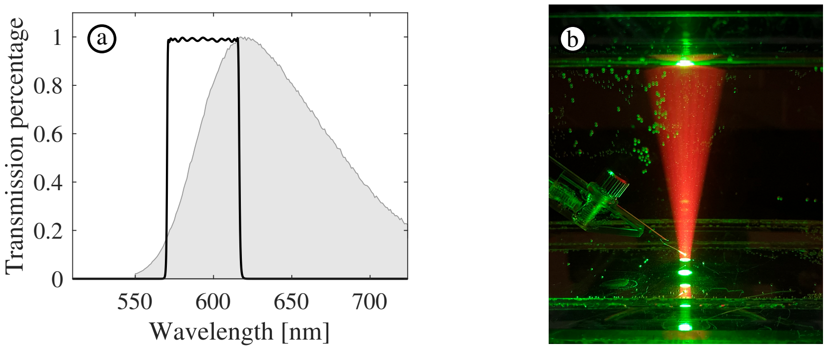

Figure 4.19: (a) The light spectrum of emitting PI when bound to acid nuclei with a maximum at 617 nm (gray) and the microscope filter response (black). (b) A photography of the DMEM filled tank and the region of interest lit by the microscope green light and by the 635 nm red light emitted by the not-bound PI suspended in the DMEM.

light excitation, only the RNA-bound PI can be visualized. This does not prevent the suspended not-bound PI from radiating but at lower emission amplitude and at 636 nm, which can also be seen with the naked eye, such as in figure 4.19b. The emission spectrum when bound to nucleic acids is displayed in gray in figure 4.19a.

PI is especially used in experimental works that investigate the effects of ultrasound-driven microbubbles on nearby cells, either when the bubble is maintained at a controlled distance from the cell and remotely exerts stresses on the cell membrane through a pushing-pulling motion [van Wamel et al., 2006, Wang et al., 2018], either when the oscillating bubble is directly attached to the cell membrane [Kudo et al., 2009, Kooiman et al., 2011]. It should be noted that in these previous studies, the bubble is much smaller than the cell aimed for sonoporation. Actually, the bubbles are ultrasound contrast agents (UCA) sizing in the range 1 to 10 µm, while the cells are large and substrate-adhering fibroblasts or endothelial cells able to cover several tens of micrometers. In such experimental conditions, if we consider the size difference between cells and bubbles, the cellular membrane resembles more like an infinite large wall from the bubble perspective. This is something to take into account when investigating the capacity of an oscillating bubble to generate stresses on a nearby cell, and on which we shall come back later in the discussion part.

Fluorescent imaging

The monitoring of the entry of fluorescent markers within biological cells and their binding to RNA has to be carried out with a different camera than the one employed until now. It is performed with a digital camera (Hamamatsu®, ORCA-Fusion, C14440) connected to the same inverted Nikon Eclipse-Ti microscope. With the 10× magnification optical objective, the image scale has been measured to be 0.65 µm/pixel. We chose to employ PI particles

(Sigma-Aldrich®, 81845-100 mg) as their emission wavelength fitted one of our microscope single-band light filter (BrightLine®, TRITC-B-000), for which the response curve can be found in figure 4.19a, and at a concentration of 25 mg · L^{-1} as it was successfully carried out by van Wamel et al. [2006]. Flasks of 12.5 mg PI solubilized in 12.5 mL pure water (Milli-Q® IQ 7000) were prepared upstream of the experiments, following the manufacturer's recommendations. Under the excitation of a green light, the eventually RNA-bound PI particles emit a strong red light which will be captured by the camera through the filter. As the figure 4.19a suggests, not all of the red light will be visualized, but a certain quantity in sufficient proportion to achieve a qualitative measurement. The images are processed and recorded through the software HCImage Live with a frame rate of about 93 Hz and an exposure time of 65 µs. These are the maximum limits of fast imaging that this camera can achieve.

Results

With the acquisition parameters described in previous section, it is obviously impossible to look at the acoustic time scale bubble oscillation, but the objective is else. On the other hand, if the bubble oscillation is stable enough, it is somehow possible to guess the presence and the type of the bubble nonspherical mode (especially if it is a sectoral mode) from the image averaged over several acoustic periods. This can be seen in figure 4.20a where the bubble is animated by a sectoral mode $n = 4$. We can discern 8 lobes, typical time-

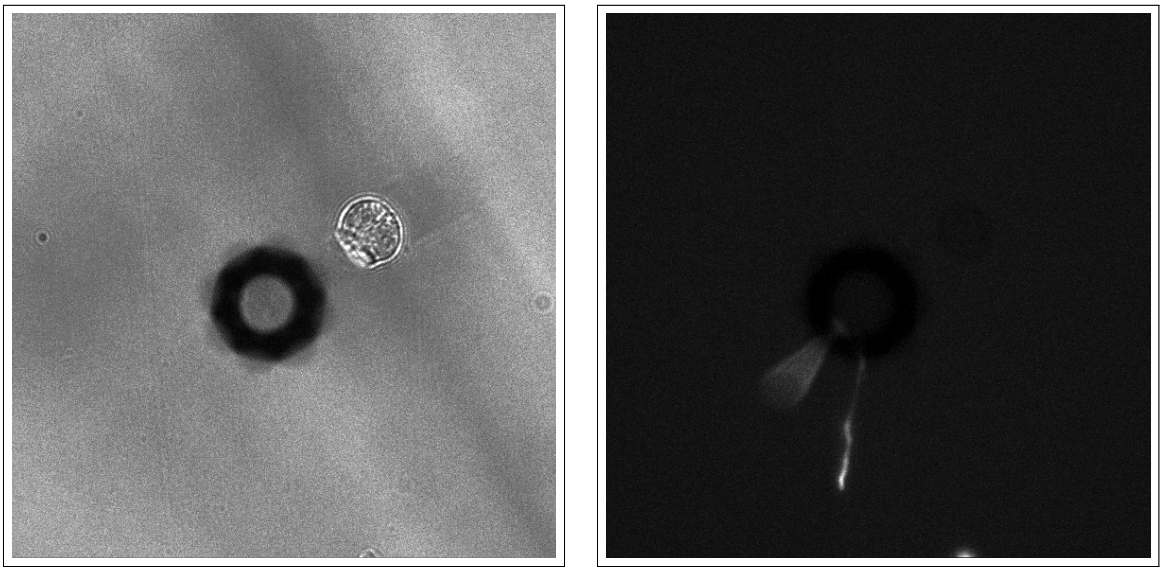

Figure 4.20: Two 65 µs-exposure snapshots, taken at different instants, of a wall-attached bubble of equilibrium radius 37.4 µm animated by a sectoral mode $n = 4$ oscillating near an adhering megakaryocyte of diameter about 41.6 µm, illuminated with the white light (left) and with the green light (right).

averaged signature of this nonspherical mode, as already seen in chapter 3. In addition, there is possibly a zonal mode too, but this alternative setup does not allow us to be certain. In figure 4.20b where only the green light is turned on, the fluorescent cells come into sight. In the lower edge of the image, a small adhering cell already fluorescent before the bubble was placed indicates the proper functioning of fluorescence. In addition, a bouncing-on-the-bubble and fluorescent cell is detected. It is the trail of light that we can observe. During the 65 µs exposure duration, it had the time to move out-of-focus towards the bubble and then to be expelled within the imaging focal plane located near the bubble equatorial plane. It reveals again the antifountain-like behavior of the sectoral-induced streaming. This bouncing fluorescent cell is a particular case, most of the cells caught in the streaming and passing by the bubble being and remaining not fluorescent. Lastly, the large adhering cell that was initially aimed for sonoporation sees itself rejected with a constant outward force, under the action of the bubble-induced streaming, as visible in figure 4.20a. The cell is pushed towards the upper right corner of the image with respect to its narrow contact with the substrate, oval-shaped brighter area, closer to the bubble.

Several experimental attempts led to the same conclusion: Although the cell was clearly under the action of a strong streaming for several minutes and that a pushing-pulling action was also discernible, no internalization of fluorescent particles has been detected in a nearby adhering megakaryocyte aimed for sonoporation. At the acoustic time scale, section 4.3.2 was reporting a limited cell strain whether with or without the presence of a nonspherical mode. In any cases, it would seem, in view of these unsuccessful attempts to internalize particles, that these deformations were too little to hope for successful permeabilization. On the other hand, we can then ask ourselves why the bubble-induced effects at the fluidic time scale did not allow to sonoporate cells, while many publications unanimously agree to say that bubble-induced streaming is the first cause for cell sonoporation. They are also numerous to prove this theoretically for the case of a free bubble spherically oscillating. It should be probably worth reminding that these works consider the cell as an infinite wall, on which a flow would necessarily induce shear stresses, while in a condition of spherical cell small, or similarly sizing, in comparison to the bubble (which is our experimental condition), we can expect the streaming not to be as impairing for the cell membrane due to a possibility for the flow to simply pass by instead of perceiving the cell as an insurmountable obstacle. Theoretically, Doinikov and Bouakaz [2010] demonstrated that, in a case of purely spherical oscillation, a maximal shear stress on a wall, located at a distance d from the center of a free bubble, occurred at a distance $x \simeq 1.13\ d$. If the cell is small compared to the bubble, this location of the maximum shear stress is a point that presumably does not belong to the cell. In contrast, most experimental works reporting successful particles internalization at the micro-scale of one single cell typically employ an UCA (1-10 µm diameter) and situate therefore in an experimental condition of a very small bubble size compared to the targeted biological cell [van Wamel et al., 2004, Okada et al., 2005, van Wamel et al., 2006, Kooiman et al., 2011].

4.4 Conclusion

Studying the mechanical interaction between a single bubble and a biological cell at the micro-scale level could help in understanding the complex macro-scale phenomenon in which a cloud of ultrasound-driven microbubbles interact with a population of biological cells. In this chapter were presented several scenarios of cell's mechanical responses when stimulated by a microbubble undergoing nonspherical shape modes. Bubble-induced cellular motions and deformations took place at both acoustic and fluidic time scales.

At the acoustic time scale, the bubble pushing-pulling action on a tethered cell is investigated along two geometrical indexes, the close-to-bubble cell's point displacement and the cell strain amplitude. From these are evidenced two distinct parts in the cell mechanical response, a solid-body translation and a deformation. For a same amplitude of the radial displacement, the emergence of a bubble sectoral mode induces an increase in the cell deformation, provided the bubble-to-cell distance is very short. At long distance, the cell only perceives the harmonic excitation due to the radial oscillation, while the subharmonic excitation due to the nonspherical oscillation is consequence-free. Tracking shear waves induced in a megakaryocyte by a bubble driven at 85 kHz oscillating on a sectoral mode $n = 4$ has allowed to successfully measure the cellular elasticity. It has been demonstrated that the shear modulus of an adhering megakaryocyte is about 25-35 Pa and seems to locally double near the contact line with the substrate.

At the fluidic time scale, the motion of cells caught in the fluid flow generated by a microbubble oscillating on a sectoral mode $n = 5$ was studied. When they are trapped in the stagnation points of streaming recirculation loops, their tumbling velocity can be explained on the basis of their characteristic size. The more they cover a large span in the flow vortex, the more their speed of rotation is high. When a disruptive event occurs, the cells that were trapped resume to their flowing motion, following an outward trajectory in the bubble equatorial plane.

Lastly, fluorescent markers (propidium iodide) were appended within the experimental medium so that the sonoporation of an adhering megakaryocyte could be assessed, under the action of a nearby nonspherically oscillating microbubble. Although the intensity of streaming did not seem to lack, as well as the acoustic time scale bubble pushing-pulling action, every targeted cells remained untouched, not sonoporated, or not sufficiently enough to let in propidium iodide. Yet, the conclusion must be moderated, especially since one particular cell is not another. To a certain extent, they all differ in their stiffness, internal structure, fragility, resilience and response to a nearby oscillating microbubble. For this reason, saying that bubble nonspherical modes do not facilitate the cellular sonoporation is probably a bit impulsive as a conclusion, so early in the slow quest for localized drug delivery with microbubbles.

Conclusion

The sonoporation, i.e. the ultrasound-induced permeabilization of the membrane of biological cells, is today widely accepted as a promising and effective therapeutic tool for facilitating the cellular uptake of drugs or genes. Moreover, the scientific literature agrees on its relation with the activity of microbubbles activated by acoustics. Although the assets are multiple, there is always a major drawback: The behavior, nucleation, dynamics and extinction of a myriad of microbubbles are very complex, erratic and possibly violent phenomena. Eventually, they can turn into as much ready-to-collapse bombs able to locally rise the temperature up to thousands of Kelvin degrees and the pressure to colossal magnitudes. Nevertheless, the control of their dynamics, and hence of their potential thermal and mechanical energy, could allow to minimize the harmful effects and maximize the therapeutic action. To this end, the present thesis work had as an objective to enhance the comprehension of interacting bubbles and cells through the investigation at the micro-scale level of the mechanical interaction between one single oscillating microbubble and one single biological cell. Prior to placing a cell near a bubble, the underlying mechanisms induced by this bubble oscillatory motion were studied in very wide and detailed terms. The outcomes are summed-up in what follows.

The ultra-fast imaging of a microbubble driven by an amplitude-modulated acoustic field allowed to describe its time-resolved dynamics. Its monitoring along the increasing part of the modulation evidenced, first in a qualitative way, vibration sequences, namely the successive emergence of specific nonspherical modes, that were bubble size-related, hence revealing a nondegeneracy (spectral splitting) of the set of spherical harmonics. Close to the modal resonances, the microbubbles were more inclined to trigger zonal and sectoral modes, while elsewhere tesseral modes were more predisposed to show up firstly. The observation of sectoral and zonal modes dynamics evidenced two different behaviors of competitiveness. Their coexistence, facilitated or not, is explained on the basis of their interplay in amplitude and phase shift, as well as their geometric compatibility. As a result, zonal and sectoral modes of odd degree ($n = 3$ and $n = 5$) display a strong competitiveness: the emergence of one mode occurring at the expense of the other one, accompanied with important and varied phase shifts. On the other hand, zonal and sectoral modes of even degree ($n = 4$ and $n = 6$) show ease to coexist: the emergence of one mode never hinders the other one, and their time-resolved dynamics is always synchronized in phase.

The appending of tracking particles within the experimental medium allowed to bring to light the fluid flows generated by the bubble nonspherical modes. A further quantitative study of the bubble modal content allowed to assign values to amplitudes, so that the modal interaction truly responsible for the formation of streaming could be assessed. Five experimental scenarios were analyzed: a zonal mode, a sectoral mode, a tesseral mode, a combination of zonal and sectoral modes and a combination of tesseral and sectoral modes. Provided the bubble nonspherical oscillation was stable, recirculation loops were experienced with a direction of flow going away from the displacement anti-nodes of the bubble interface and coming back towards its displacement nodes. For most of these modal configurations, a rule of thumb could be drawn for explaining the observed patterns, closely related with the number and the position of nodal lines at the interface of the nonspherical bubble. In the particular case of interacting zonal and sectoral modes for which a more in-depth analysis has been carried out, a differentiation between two sorts of recurrent patterns, flower shapes and star shapes, has been explained by their interaction strength. Besides, some occasional visualizations of streaming from a side-view perspective confirm the previously dictated trends and made it possible to designate the sectoral mode as having a greater mixing power than the axisymmetric zonal mode, the latter being the modal deformation formulated in most of the theories on nonspherical bubbles.

When an oscillating bubble is brought closer to a biological cell, its influence is twofold. At the acoustic time scale it occurs a periodic pushing-pulling action on the cell, and at the fluidic time scale the cell undergoes a steady stress due to the bubble-induced streaming. Despite none of these two mechanisms could have been demonstrated through our experiments as responsible for an internalization of fluorescent markers within megakaryocytes, the study of the dynamics of the bubble-cell pair is nonetheless interesting. This led us to successfully characterize the cellular elasticity and its stiffening caused by its adherence to the substrate, but also to discover and measure the tumbling and flowing motions of suspended cells caught in the vortices of streaming recirculation loops.

Future follow-up and perspectives

From an experimental point of view, the successful sonoporation with an oscillating bubble at the single-cell scale is not brand new, although the involved mechanisms remain so far not fully understood. Also, it is very likely that, depending on whether the biological cell is very large compared to the bubble size, or the opposite situation, the streaming-induced shear stresses that apply on the cell may dramatically change. With that in mind, it would be really worth investigating through precise measurements the effective generation of stresses on a surface of variable area placed near a bubble animated by nonspherical modes. This is an aspect that will be soon investigated by Estelle Meziani during her forthcoming doctoral work. To this end, with the recent purchase of a four channels camera, the fluid flow generated by a wall-attached bubble undergoing asymmetric shape modes could be characterized in the whole fluid volume containing the oscillating bubble. It should also bring the missing information for fully explaining the experimental microstreaming of bubble asymmetric modes, only presented in two dimensions throughout this thesis manuscript.

An other aspect that would also deserve a more in-depth investigation concerns the conditions for which the emergence of particular bubble nonspherical modes takes the advantage on the emergence of others. The mechanisms underlying which shape mode is chosen to grow to a steady-state, and selected out, is not fully revealed so far. As a bubble at rest adopts a spherical shape in order to minimize its surface, the selection of nonspherical modes might also be explained by some aspects involving an energy minimization, and not only the matching of the contact line with the displacement nodes of the bubble nonspherical oscillation. In fact, theoretically predicting the conditioning of the tethering on the appearance of the set of nonspherical modes of a wall-attached bubble would require more than an investigation of the truncated spherical harmonics, given that the contact line mobility, the variability of the contact angle at rest, the possible existence of vertical translation mode (hard to capture in a top-view configuration) or the kinetic energy required for the bubble interface to bend and adopt nonspherical deformations may all play a crucial role. First attempts of the calculation of some of these magnitudes failed to be decisive. The complexity undoubtedly lies in the fact that all these aspects must be taken in consideration as a whole system and not resolved separately, hence the likely need for an extensive resolution of the attached bubble dynamics by numerical simulation.

Our comprehension now enhanced on the dynamics of the whole set of nonspherical modes and their induced streaming especially benefited to Claude Inserra and Alexander Doinikov for initiating an analytic work on the streaming generated by bubble asymmetric modes. In addition to validating the experimental results, this should bring further information on the streaming velocities where it was difficult to make measurements, in the very near vicinity of the bubble interface or elsewhere at varied elevations. This should also allow to assess the shear stresses applying at a given distance, on a nearby wall, for instance.

With a similar aim, it has been multiple times undertaken to implement numerical simulations on the software STAR-CCM+®, which was resolving the Navier-Stokes equation in a meshed domain surrounding a nonspherically oscillating bubble, from an initial condition given by the expression of its interface velocity. We have been so far unable to conclude on first results, even if they were not completely absurd. It is a path that should imperatively be pursued since it could allow to do what the theoretical expressions could not easily, which is, considering the bubble attached to a wall or the presence of a nearby biological cell. With all these tools, the whole picture could probably be completed so that the bubble-cell interaction would have a lot less secrets. This could also bring an explanation for the following unanswered questions. What logic governs the interaction between tesseral and sectoral modes ? To what extent does the tethering quantitatively impact the streaming of axisymmetric modes in comparison to the case of the free microbubble ? Why did all the nearby adhering cells have not been sonoporated ?

Lastly, concerning this recurrent inability to sonoporate cells and internalize particles, it might be interesting to reiterate experiments with some changes in the experimental setup. Keeping PI as a fluorescent marker of RNA, being small enough to be internalized in comparison to other commonly used markers, it could be rewarding to design and 3D-print a sort of blocking frame, or any system, stemming the possibility for the cell to translate. In such a configuration, megakaryocytes would have no other choice but to comply and deform under the bubble action. An alternative would be to change the cellular model for a more naturally substrate-adhering one, e.g. a fibroblast or an endothelial cell. In these conditions, the cellular deformation measured at the acoustic time scale might be stronger so that the membrane stretching and permeabilization would hopefully occur. Through a multi-parameter study, the presence of bubble shape modes and the distance to cell could be finally correlated with the rate of effective sonoporation.

Appendix A

Nonspherical bubbles from a side-view

This appendix explores some bubble shape modes and induced streaming from a lateral perspective, thanks to a variant of our experimental configuration. This allows to have a closer look on the contact with the wall and to discuss in appendix A.1 the tethering-induced discrepancy of the attached bubble nonspherical shapes with respect to the theoretical spherical harmonics and the shape of a numerical free bubble of equivalent modal content. Then, appendix A.2 proposes complementary results of microstreaming visualized from this same alternative side-view perspective. This provides additional information on what was not visible under the single top-view. The comparison is especially done between sectoral and zonal modes, which are furthermore the bubble shape modes most often reported in literature.

A.1 Bubble dynamics

This experimental variant owes its realization from the motivation to examine more closely the bubble shape and dynamics near the contact, which would hopefully bring confidence in our modal analysis and comfort in the interpretation of the results presented before. The question of the possible shift in elevation of the nodal parallels due to the tethering is also a matter still pending. More exactly, the questions that carry this side-view experiment and which were fed in particular by the discussion with Professor A. Maksimov are the followings: Is the number of nodal lines of a nonspherical free bubble and the number of nodal lines in the similar modal case of a tethered bubble the same ? Does the tethering induce a shift in elevation of the nodal parallels ? Assuming that the superior hemisphere of the bubble can be correctly described by the spherical harmonics, does the same hold for the inferior hemisphere ? If a shift operates on the nodal parallels and on the initial position of the equator with respect to the free bubble case, to what extent can

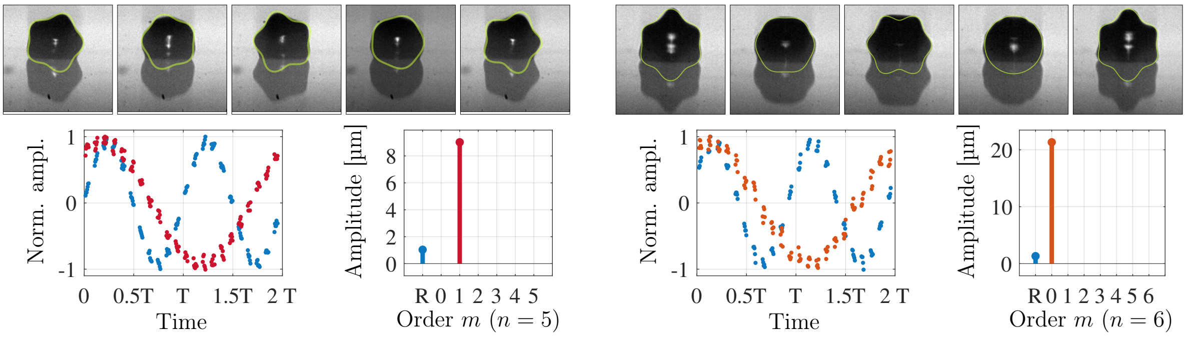

ⓐ Tesseral mode Y_{51}

ⓑ Zonal mode Y_{60}

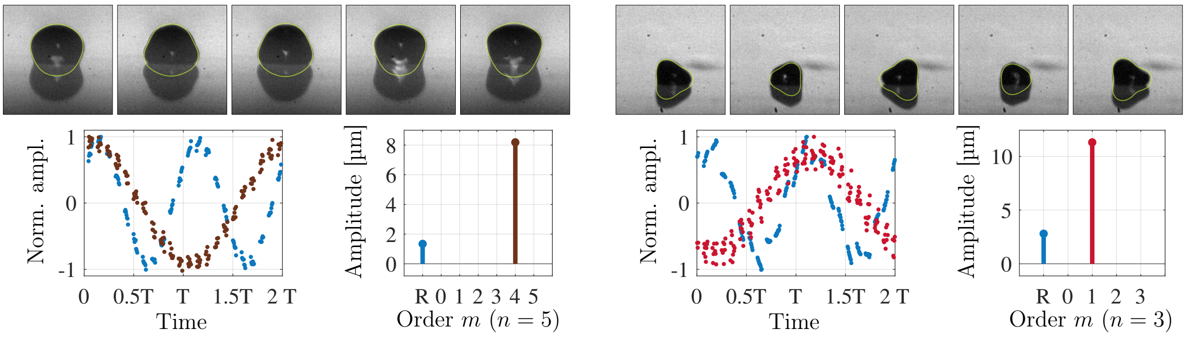

ⓒ Tesseral mode Y_{54}

ⓓ Tesseral mode Y_{31}

Figure A.1: Snapshot series and modal analysis of a microbubble of equilibrium radius 111.9 µm undergoing a tesseral mode Y_{51} (a), a microbubble of equilibrium radius 125.8 µm undergoing a zonal mode Y_{60} (b), a microbubble of equilibrium radius 111 µm undergoing a tesseral mode Y_{54} (c) and a microbubble of equilibrium radius 72.2 µm undergoing a tesseral mode Y_{31} (d), observed from a side-view. The modal parameters obtained from the analysis of the experimental bubble are employed to numerically reconstruct an equivalent nonspherical free bubble of which the contour is superimposed on the experimental snapshots.

it influence our modal analysis tool ?

To serve these purposes and to bring some further answers, the camera was placed in side-view and equipped with an objective lens (Navitar). The image scale has been measured to be 3.7 µm/pixel. The other experimental parameters remain unchanged compared to table 2.1. Several oscillating bubbles were imaged from the side-view and four selected examples are given in figure A.1. The bubble modal content is obtained by decomposition of its contour on the associated Legendre polynomials

$$a_{nm}(t) = \frac{2n+1}{2}\sqrt{\frac{(n-m)!}{(n+m)!}}\int_0^{\pi} r^*(\theta,t)P_{nm}[\cos\theta]d\theta, \tag{A.1}$$

where $r^*(\theta,t)$ is the bubble side-view contour of which the missing truncated part (due to the tethering) has been numerically completed for each m-order projection. This results in falsely important amplitudes for modes that do not really exist, but also to an accurate amplitude calculation of the tethered bubble modes truly present. Also, we have chosen to hide the irrelevant modal amplitudes in the spectra presented in figure A.1. Provided the bubble is correctly orientated with respect to the camera view, the modal calculation is optically validated by superimposing a numerical reconstruction of an equivalent free bubble (amplitude and phase shift obtained from the modal analysis) on the experimental snapshots. This has been performed with good agreement in the four selected examples displayed in figure A.1. At the first look, the contact lines seem immobile and the experimental modal shapes near the wall to be ensured by a great flexibility of the contact angle, seeing that the largest discrepancy between the contours of the equivalent numerical free bubble and the experimental tethered bubble occurs at the contact. In addition, bubbles undergoing few-nodal-parallels nonspherical modes (such as the mode Y_{31} in figure A.1d) seem to present a greater disparity of their lower hemisphere and thus a greater disparity at the equator with the numerically reconstructed free bubble than several-nodal-parallels modes (such as modes Y_{51} in figure A.1a and Y_{60} in figure A.1b) for which the matching is more obvious and the description with the spherical harmonics more appropriate.

In definitive, if there is indeed a shift of the nodal parallels due to the tethering, in comparison with their position in the free bubble case, this change in elevation must only occur very slightly or only very close to the contact. In a top-view configuration, we can expect the observation of shape modes characterized by a low number $(n - m)$ of nodal parallels to be more impacted and distorted by the tethering than shape modes characterized by a higher number of nodal parallels. This might explain the noisy and less accurate oscillation of the tesseral mode Y_{31} in figure A.1d, in comparison to the other modal cases. In our case of tethering with a PMMA substrate, the contact line shows weak or no mobility, which necessarily generates modal selection and, in the same way, reinforces our observations of nondegeneracy of nonspherical modes evidenced in chapter 2.

Lastly, the postulate made in chapter 2, assuming that the modal degree n is known once the bubble radius is measured, is even more evident. The tesseral modes Y_{51} ($R_0 = 111.9\,\mu\text{m}$) and Y_{54} ($R_0 = 111\,\mu\text{m}$) identified in figures A.1a and A.1c, respectively, concern bubble radii in the vicinity of the 108.3 µm resonant radius of the $n = 5$ modal degree. The same is true for the zonal mode Y_{60} ($R_0 = 125.8\,\mu\text{m}$) and the tesseral mode Y_{31} ($R_0 = 72.2\,\mu\text{m}$) identified in figures A.1b and A.1d, respectively, for which the bubble radii approach the resonant radii of the $n = 6$ and $n = 3$ modal degrees, respectively, 130.5 µm and 68.2 µm.

A.2 Microstreaming

In a similar configuration, the visualization of the bubble-induced streaming from a side-view was at first motivated by the will to validate the conjecture made in section 3.2.2 and figure 3.8, which argued that sectoral modes devoid of nodal parallels would generate a quadrupole-shaped pattern following the longitudinal dimension, in a similar way as a translation motion. In addition, the side-view perspective should allow to observe the influence of the wall on the streaming of zonal modes. Since the microstreaming induced by free axisymmetric bubbles is very well documented in literature, comparing the two experimental situations, with and without tethering, should be of great interest. However, because we only achieved an image scale of 3.7 µm/pixel in this side-view setup, the small recirculation loops localized in close proximity of the bubble interface might be difficult to discern.

Sectoral from a side-view

Figures A.2a and A.2b expose experimental images of the side-view streaming generated by a bubble sectoral mode of degree $n = 4$ and $n = 5$, respectively. It very clearly evidences the two superior recirculation loops of a quadrupole-shaped pattern. Due to the truncation of the bubble, the two inferior ones are absent, which does not prevent our conjecture from being confirmed. The fluid particles are ejected by the displacement anti-nodes of the bubble interface and steered back towards the displacement nodes of the bubble interface. The fluid motion exhibits an antifountain-like pattern above the bubble with a very large area of action and significant velocities in the whole frame of visualization. This streaming shape may be reminiscent of fountain-like streaming patterns induced by a radial oscillation interacting with a vertical translation motion [Marmottant and Hilgenfeldt, 2003]. This is not particularly surprising since, if we consider the sectoral mode in a vertical cross-section, sectoral and vertical translation oscillations are analogous oscillatory motions, up to a rotation by $\pi/2$: similar shape deformation and same number of displacement nodes and anti-nodes. Lastly, these two patterns given in figures A.2a and A.2b do not seem to differ significantly from one modal degree to another, at least from this side-view perspective. The velocities of particles are also of the same order of magnitude.

Zonal from a side-view

Figures A.2c and A.2d expose experimental images of the side-view streaming generated by a bubble zonal mode of degree $n = 3$ and $n = 4$, respectively. The fluid motion induced by these zonal modes has a fountain-like behavior above the bubble. This is not surprising as every zonal modes have an anti-node of bubble interface displacement

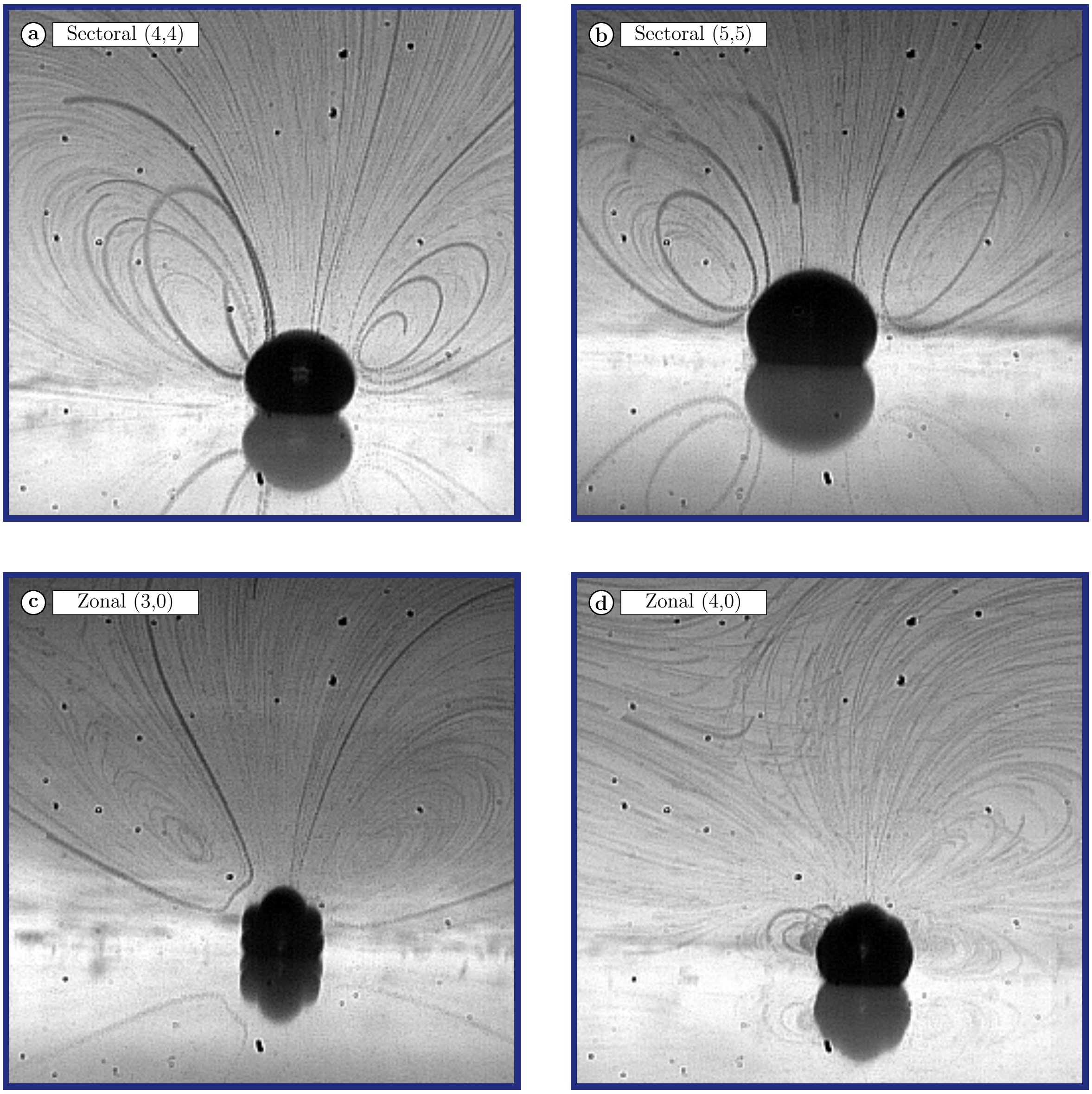

Figure A.2: Observation from a side-view of the microstreaming pattern generated by a bubble undergoing an asymmetric sectoral mode of degree $n = 4$ (a) and $n = 5$ (b) and by a bubble undergoing an axisymmetric zonal mode of degree $n = 3$ (c) and $n = 4$ (d).

at its poles ($\theta = 0$ and $\theta = \pi$). This is a specific feature of zonal modes that no other bubble shape modes has. We could therefore safely conclude that the zonal modes of a wall-attached bubble are the best culprits in inducing a fountain-like streaming. On the other hand, their very limited area of action makes us think that the mixing power of zonal modes is very weak, at least compared to sectoral modes. This discrepancy of the magnitudes of streaming velocity between zonal and sectoral modes is confirmed when comparing with the results of Cleve et al. [2019] who report zonal-induced streaming velocities on the order of $1\,\mathrm{mm} \cdot \mathrm{s}^{-1}$ at a distance $2R_0$, while we have seen in chapter 3 that the streaming induced by sectoral modes can easily reach velocities on the order of 20 to $30\,\mathrm{mm}\cdot\mathrm{s}^{-1}$ at a same distance $2R_0$.

The zonal mode $n = 4$ in figure A.2d exhibits important recirculation loops at the equator, unlike the zonal mode $n = 3$ in figure A.2c. These large toroidal loops (see figure A.2d) that join the two hemispheres, without marking the meeting of streamlines with the anti-nodes of the bubble interface displacement located at the equator, seem hard to interpret. This streaming pattern associated to the zonal mode $n = 4$ of a tethered bubble differs from the equivalent case of the axisymmetric free bubble, which was given in figure 3.3d. This is an evidence of the immense repercussions of tethering on the bubble streaming. In perspective, a better experimental definition close to the bubble interface or an adequate numerical simulation could provide the explanations necessary to identify the exact influence of the wall attachment.

A.3 Conclusion

As a conclusion, the bubble visualization from a side-view highlighted the tethering-induced selection of nonspherical shapes. It appeared that nonspherical modal shapes of an attached bubble can differ importantly close to a slightly movable contact, compared to the theoretical spherical harmonics. Provided that the nonspherical interface of a bubble has few nodal parallels, it is very likely that its top-view contour will be more distorted than in the case of several nodal parallels, in comparison to the theoretical spherical harmonics. A bias is therefore expected in the modal decomposition with spherical harmonics. The question of using spherical harmonics to describe the shape of an attached bubble was worth asking, even if the certainly not trivial exact solution, requiring an access to the contact line dynamics and an extensive comparison of the two experimental cases of free and attached bubbles, is out of the scope of this thesis work.

Lastly, the side-view capture of streaming evidenced the global antifountain- and fountain-like behaviors of sectoral and zonal modes. Sectoral modes clearly induce larger areas of action compared to zonal modes. The comparison with literature confirms this discrepancy in term of the streaming velocity magnitudes. It therefore seems reasonable to think that sectoral modes would have stronger consequences than zonal modes on a nearby wall or biological cell, and would thus be better candidate for inducing cellular sonoporation.

Appendix B

Some aside results on oocytes

As mentioned in section 4.1.1, the arrival in our lives of the COVID-19 virus (SARS-CoV-2) and the implementation of consecutive lockdowns by the health authorities in the years 2020 and 2021 did not allow us to perform an extensive study on oocytes, which were originally chosen as one of the two cell models of this thesis work. This is due to the forced shutdown, and later to the slowdown, of the activities of many companies, universities and laboratories, including our supplier, the Faculty of Medicine of Laënnec. Nevertheless, in order to honor this collaboration and the time spent for implementing these experiments (cells retrieval, glass capillaries manufacture and images post-processing), as well as to discuss some encountered difficulties, this appendix reports few figures and results on interacting bubbles and oocytes.

Overall, two one-day series of experiments on oocytes have been performed in the company of Estelle Meziani, Master 1 student at that time. The first day settled on no result at all, due to our mistake of having kept the oocytes for the day in DMEM instead of a medium more appropriate, which quickly led to their premature death, unfortunately. The second day, M2 medium (Sigma-Aldrich®, M7167-50 mL, with hepes, without penicillin) has been employed to conserve them. As described in details in chapter 4, the oocytes, unable to adhere to a substrate, were fastened by means of a glass capillary and a microaspiration system. When the oocyte attachment was a success, which was not always straightforward, it became easy to keep it immutable as long as needed and to have a great control on the cell-to-bubble distance. This configuration of acoustic parameters and cell size was very convenient, so that images as the ones depicted in figure B.1 could be captured. The curvature of the top-view contour of a 70 µm oocyte is investigated through two different cases of bubble modal configuration: a radial mode only (see figure B.1a) and an additional tesseral mode of degree $n = 3$ and order $m = 2$ (see figure B.1b). In both cases, the first images depict the instantaneous curvature. Then, twenty of them

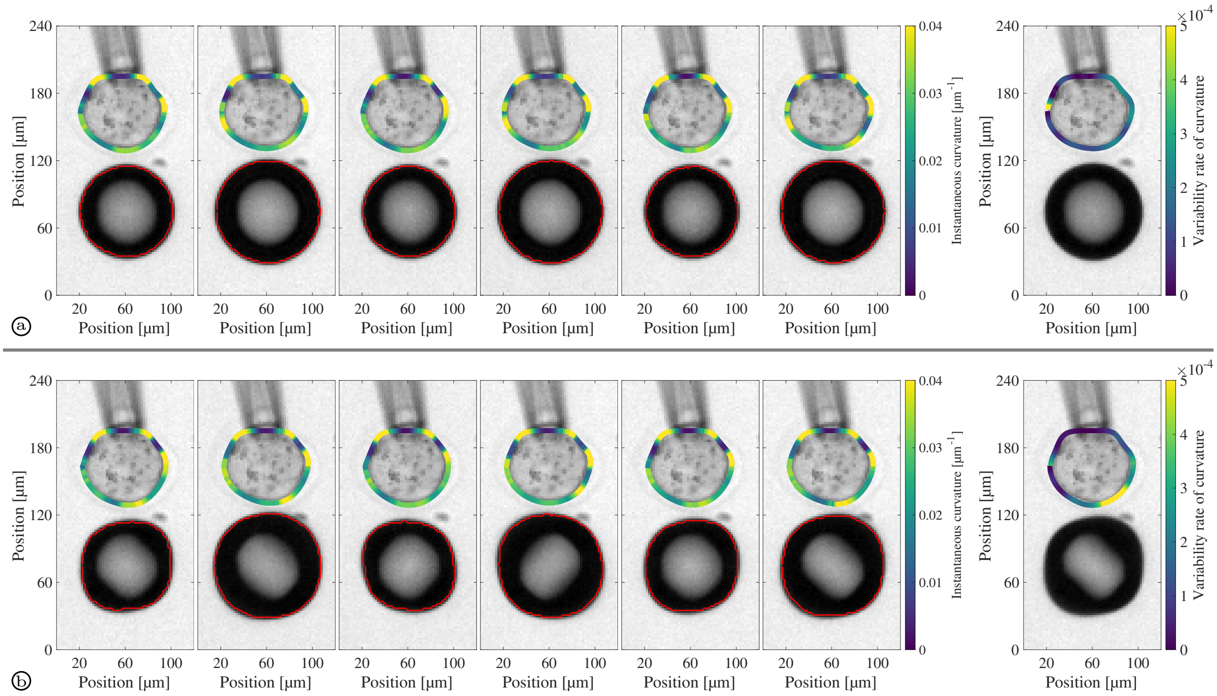

Figure B.1: Snapshot series of a 70 µm oocyte interacting with a bubble ($R_0 = 46$ µm) driven by a 66.5 kHz acoustic field and animated by a radial mode only (a) and by an additional tesseral mode of degree $n = 3$ and order $m = 2$ (b), imaged at a frame rate of 139 650 Hz with a 10× magnification optical lens.

are employed to calculate the variability rate of curvature, which is illustrated in the last snapshot of both sub-figures. It evaluates how the cell curvature varies as a function of time and space, and basically consists in a calculation of the curvature variability. In the case of the tesseral mode, the bubble deformation is out-of-line with the bubble-to-cell axis and it results in a stronger asymmetric curvature rate than in the radial mode only case, as visible in the last snapshots of figure B.1. The apparent asymmetry probably comes from the position in elevation of the cell with respect to the bubble tesseral mode, which possesses only one $(n - m)$ nodal parallel. As a consequence, the oocyte is very likely affected by an hemisphere only of the bubble. Cellular deformations are often quantified as a whole by means of global variables, the axial ratio [Xie et al., 2016], the area stretching [Evans et al., 1976] or the cross section [van Wamel et al., 2004], while the information at the local level could also be meaningful. With this recent analysis, we wanted to explore cellular deformations in an original way. Compared to the geometrical indexes presented in section 4.2.5, this curvature calculation allows to evidence asymmetric local deformations. So far, it seems to very well highlight the interest of triggering bubble nonspherical modes to promote local deformations on a cell membrane.

Bibliography

O. A. Abramova, I. Sh. Akhatov, N. A. Gumerov, Yu. A. Pityuk, and S. P. Sametov. Numerical and experimental study of bubble dynamics in contact with a solid surface. *Fluid Dynamics*, 53(3):337–346, 2018.

S. R. G. Avila and C.-D. Ohl. Fragmentation of acoustically levitating droplets by laser-induced cavitation bubbles. *Journal of Fluid Mechanics*, 805:551–576, 2016.

D. Baresch and V. Garbin. Acoustic trapping of microbubbles in complex environments and controlled payload release. *Proc. Natl. Acad. Sci.*, 117:15490–15496, 2020.

T.B. Benjamin. Pressure waves from collapsing cavities. *Proc. Second ONR Symp. Naval Hyrdodynamics*, pages 207–233, 1958.

P. R. Birkin, Y. E. Watson, and T. G. Leighton. Efficient mass transfer from an acoustically oscillated gas bubble. *Chem. Commun.*, 24:2650–2651, 2001.

P.R. Birkin, D.G. Offin, C.J.B Vian, T.G. Leighton, and A.O. Maksimov. Investigation of noninertial cavitation produced by an ultrasonic horn. *J. Acoust. Soc. Am.*, 130(5): 3297–3308, 2011.

R. Bolaños-Jimenez, M. Rossi, D. Fernandez Rivas, C. J. Kähler, and A. Marin. Streaming flow by oscillating bubbles: quantitative diagnostics via particle tracking velocimetry. *J. Fluid Mech.*, 820:529–548, 2017.

S. N. Borchsenius, I. E. Vishnyakov, O. A. Chernova, V. M. Chernov, and N. A. Barlev. Effects of mycoplasmas on the host cell signaling pathways. *Pathogens*, 9:308, 2020.

N. Bose, D. Carugo, T. Kumar Maiti, X. Zhang, and S. Chakraborty. The role of cell membrane strain in sonoporation characterised by microfluidic-based single-cell analysis. In *15th International Conference on Miniaturized Systems for Chemistry and Life Sciences*, volume 35, pages 1743–1745, October 2011. ISBN 978-0-9798064-4-5.

J.B. Bostwick and P.H. Steen. Dynamics of sessile drops. part 1. inviscid theory. *J. Fluid Mech.*, 760:5–38, 2014.

M. P. Brenner, D. Lohse, and T. F. Dupont. Bubble shape oscillations and the onset of sonoluminescence. *Physical Review Letters*, 75(5):954–957, 1995.

G. L. Chahine, A. Kapahi, J.-K. Choi, and C.-T. Hsiao. Modeling of surface cleaning by cavitation bubble dynamics and collapse. *Ultrasonics Sonochemistry*, 29:528–549, 2016.

C. Chang, J. B. Botswick, P. H. Steen, and S. Daniel. Substrate constraint modifies the rayleigh spectrum of vibration sessile drops. *Physical Review E*, 88:023015, 2013.

C. Chang, S. Daniel J.B. Bostwick, and P.H. Steen. Dynamics of sessile drops. part 2. experiment. *J. Fluid Mech.*, 768:442–467, 2015.

J. E. Chomas, P. Dayton, J. Allen, K. Morgan, and K. W. Ferrara. Mechanisms of contrast agent destruction. *IEEE Trans. Ultrason. Ferroelectr. Freq. Control*, 48:232–248, 2001.

S. Cleve, M. Guédra, C. Inserra, C. Mauger, and P. Blanc-Benon. Surface modes with controlled axisymmetry triggered by bubble coalescence in a high-amplitude acoustic field. *Physical Review E*, 98:033115, 2018.

S. Cleve, M. Guédra, C. Mauger, C. Inserra, and P. Blanc-Benon. Microstreaming induced by acoustically trapped, nonspherically oscillating microbubbles. *J. Fluid Mech.*, 875: 597–621, 2019.

Sarah Cleve. *Microstreaming induced in the vicinity of an acoustically excited, nonspherically oscillating microbubble.* PhD thesis, Université de Lyon, 2019.

J. Collis, R. Manasseh, P. Liovic, P. Tho, A. Ooi, K. Petkovic-Duran, and Y. Zhu. Cavitation microstreaming and stress fields created by microbubbles. *Ultrasonics*, 50:273–279, 2010.

S. Courty, G. Lagubeau, and T. Tixier. Oscillating droplets by decomposition on the spherical harmonics basis. *Physical Review E*, 73:045301(R), 2006.

B. J. Davidson and N. Riley. Cavitation microstreaming. *J. Sound. Vib.*, 15:217–233, 1971.

C. X. Deng, F. Sieling, H. pan, and J. Cui. Ultrasound-induced cell membrane porosity. *Ultrasound Med Biol.*, 30:519–526, 2004.

A. A. Doinikov and A. Bouakaz. Exploration of shear stresses snduced by a contrast agent bubble on the cell membrane. *10ème Congrès Français d'Acoustique*, hal-00541376: Lyon, 2010.

A. A. Doinikov, S. Zhao, and P. A. Dayton. Modeling of the acoustic response from contrast agent microbubbles near a rigid wall. *Ultrasonics*, 49:195–201, 2009.

A. A. Doinikov, L. Aired, and A. Bouakaz. Dynamics of a contrast agent microbubble attached to an eastic wall. *IEEE Transactions on Medical Imaging*, 31:654–662, 2011.

A. A. Doinikov, S. Cleve, G. Regnault, C. Mauger, and C. Inserra. Acoustic microstreaming produced by nonspherical oscillations of a gas bubble. i. case of modes 0 and m. *Phys. Rev. E*, 100:033104, 2019a.

A. A. Doinikov, S. Cleve, G. Regnault, C. Mauger, and C. Inserra. Acoustic microstreaming produced by nonspherical oscillations of a gas bubble. ii. case of modes 1 and m. *Phys. Rev. E*, 100:033105, 2019b.

B. Dollet, S. M. van der Meer, V. Garbin, N. de Jong, D. Lohse, and M. Versluis. Nonspherical oscillations of ultrasound contrast agent microbubbles. *Ultrasound Med. Biol.*, 34(9):1465–1473, 2008.

B. Dollet, P. Marmottant, and V. Garbin. Bubble dynamics in soft and biological matter. *Annual Review of Fluid Mechanics*, 51:331–355, 2019.

S. A. Elder. Cavitation microstreaming. *J. Acoust. Soc. Am.*, 31:54, 1959.

J. M. Escoffre, K. Kaddur, M. P. Rols, and A. Bouakaz. In vitro gene transfer by electrosonoporation. *Ultrasound in Med. and Biol.*, 36:1746–1755, 2010.

E. A. Evans, R. Waugh, and L. Melnik. Elastic area compressibility modulus of red cell membrane. *Biophysical Journal*, 16(6):585–595, 1976.

M. Faraday. On a peculiar class of acoustical figures, and on certain forms assumed by groups of particles upon vibrating elastic surfaces. *Phil. Trans. R. Soc. Lond.*, 121: 299–340, 1831.

M. Fauconnier, J.-C. Béra, and C. Inserra. Nonspherical modes nondegeneracy of a tethered bubble. *Phys. Rev. E*, 102:033108, 2020.

Z. C. Feng and L. G. Leal. Nonlinear bubble dynamics. *Annu. Rev. Fluid. Mech.*, 29: 201–243, 1997.

S. Wan Fong, D. Adhikari, E. Klaseboer, and B. Cheong Khoo. Interactions of multiple spark-generated bubbles with phase differences. *Experiments in Fluids*, 46:705–724, 2009.

M. M. Forbes, R. L. Steinberg, and W. D. O'brien. Examination of inertial cavitation of optison in producing sonoporation of chinese hamster ovary cells. *Ultrasound in Medicine and Biology*, 34:2009–2018, 2008.

A. Francescutto and R. Nabergoj. Pulsation amplitude threshold for surface waves on oscillating bubbles. *Acustica*, 41:215–220, 1978.

V. Garbin, D. Cojoc, E. Ferrari, E. Di Fabrizio, M. L. J. Overvelde, S. M. van der Meer, N. de Jong, D. Lohse, and M. Versluis. Changes in microbubble dynamics near a boundary revealed by combined optical micromanipulation and high-speed imaging. *Applied Physics Letters*, 90:114103, 2007.

G. Gormley and J. Wu. Observation of acoustic streaming near albunex (r) spheres. *J. Acoust. Soc. Am.*, 104:3115–3118, 1998.

S. M. Gracewski, H. Miao, and D. Dalecki. Ultrasonic excitation of a bubble near a rigid or deformable sphere: Implications for ultrasonically induced hemolysis. *J. Acoust. Soc. Am.*, 117:1440–1447, 2005.

P. Grasland-Mongrain, A. Zorgani, S. Nakagawa, S. Bernard, L. Gomes Paim, G. Fitzharris, S. Catheline, and G. Cloutier. Ultrafast imaging of cell elasticity with optical microelastography. *Proc. Natl. Acad. Sci.*, 115:861–866, 2018.

M. Guédra, C. Inserra, C. Mauger, and B. Gilles. Experimental evidence of nonlinear mode coupling between spherical and nonspherical oscillations of microbubbles. *Physical Review E*, 94:053115, 2016.

M. Guédra, S. Cleve, C. Mauger, P. Blanc-Benon, and C. Inserra. Dynamics of nonspherical microbubble oscillations above instability threshold. *Physical Review E*, 96:063104, 2017.

X. Guo, C. Cai, G. Xu, Y. Yang, J. Tu, P. Huang, and D. Zhang. Interaction between cavitation microbubble and cell: A simulation of sonoporation using boundary element method (bem). *Ultrasonics - Sonochemistry*, 39:863–871, 2017.

H. R. Guzman, A. J. McNamara, D. X. Nguyen, and M. R. Prausnitz. Bioeffects caused by changes in acoustic cavitation bubble density and cell concentration: a unified explanation based on cell-to-bubble ratio and blast radius. *Ultrasound in Medicine and Biology*, 29:1211–1222, 2003.

P. M. Hinderliter, K. R. Minard, G. Orr, W. B. Chrisler, B. D. Thrall, J. G. Pounds, and J. G. Teeguarden. Isdd: A computational model of particle sedimentation, diffusion and target cell dosimetry for in vitro toxicity studies. *Particle and Fibre Toxicology*, 7: 36, 2010.

L. M. Hocking. The damping of capillary-gravity waves at a rigid boundary. *Journal of Fluid Mechanics*, 179:253–263, 1987.

Y. Hu, J. M. F. Wan, and A. C. H. Yu. Membrane perforation and recovery dynamics in microbubble-mediated sonoporation. *Ultrasound in Medicine and Biology*, 39:2393–2405, 2013.

C. Inserra, G. Regnault, S. Cleve, C. Mauger, and A. A. Doinikov. Acoustic microstreaming produced by nonspherical oscillations of a gas bubble. iii. case of self-interacting modes n - n. *Phys. Rev. E*, 101:013111, 2020a.

C. Inserra, G. Regnault, S. Cleve, C. Mauger, and A. A. Doinikov. Acoustic microstreaming produced by nonspherical oscillations of a gas bubble. iv. case of modes n and m. *Phys. Rev. E*, 102:043103, 2020b.

J. Kolb and W. L. Nyborg. Small-scale acoustic streaming in liquids. *J. Acoust. Soc. Am.*, 28:6, 1956.

K. Kooiman, M. Foppen-Harteveld, A. F.W. van der Steen, and N. de Jong. Sonoporation of endothelial cells by vibrating targeted microbubbles. *Journal of Controlled Release*, 154:35–41, 2011.

N. Kudo, K. Okada, and K. Yamamoto. Sonoporation by single-shot pulsed ultrasound with microbubbles adjacent to cells. *Biophysical Journal*, 96:4866–4876, 2009.

G. Laloy-Borgna, A. Zorgani, and S. Catheline. Micro-elastography: Toward ultrasonic shear waves in soft solids. *Applied Physics Letter*, 118:113701, 2021.

H. Lamb. *Hydrodynamics.* Cambridge University Press, 1916.

S. Lauren. Surface and interfacial tension. https://www.biolinscientific.com/hubfs/pdf/attension/white-papers-case-studies/surface-and-interfacial-tension-what-is-it-and-how-to-measure-it.pdf. 2017.

S. Le Gac, E. Zwaan, A. van den Berg, and C.-D. Ohl. Sonoporation of suspension cells with a single cavitation bubble in a microfluidic confinement. *Lab on a chip*, 7: 1666–1672, 2007.

R. F. Levine, K. C. Hazzard, and J. D. Lamberg. The significance of megakaryocyte size. *Blood*, 60:1122–1131, 1982.

X. Lin, T. Konno, and K. Ishihara. Cell-membrane-permeable and cytocompatible phospholipid polymer nanoprobes conjugated with molecular beacons. *Biomacromolecules*, 15:150–157, 2014.

M. S. Longuet-Higgins. Viscous streaming from an oscillating spherical bubble. *Proc. R. Soc. Lond*, 454:725–742, 1998.

J. S. Lum, V. Daeichin, D. F. Kienle, D. K. Schwartz, T. W. Murray, and M. A. Borden. Changes in microbubble dynamics upon adhesion to a solid surface. *Applied Physics Letter*, 116:123703, 2020.

J. T. S. Ma and P. K. C. Wang. Effect of initial air content on the dynamics of bubbles in liquids. *IBM Journal of Research and Development*, 6:472–474, 1962.

K. Maeda and T. Colonius. Bubble cloud dynamics in an ultrasound field. *Journal of Fluid Mechanics*, 862:1105–1134, 2019.

A. O. Maksimov. On the volume oscillations of a tethered bubble. *Journal of Sound and Vibration*, 283:915–926, 2005.

A. O. Maksimov. Splitting of the surface modes for bubble oscillations near a boundary. *Phys. Fluids*, 32:102104, 2020.

A. O. Maksimov and T. G. Leighton. Pattern formation on the surface of a bubble driven by an acoustic field. *Proceedings of the Royal Society*, 468:57–75, 2012.

P. Marmottant and S. Hilgenfeldt. Controlled vesicle deformation and lysis by single oscillating bubbles. *Nature*, 423:153–156, 2003.

P. Marmottant, M. Versluis, N. de Jong, S. Hilgenfeldt, and D. Lohse. High-speed imaging of an ultrasound-driven bubble in contact with a wall: "narcissus" effect and resolved acoustic streaming. *Experiments in Fluids*, 41:147–153, 2006.

P. Marmottant, T. Biben, and S. Hilgenfeldt. Deformation and rupture of lipid vesicles in the strong shear flow generated by ultrasound-driven microbubbles. *Proceedings of the Royal Society A*, 464:1781–1800, 2008.

S. Mehier-Humbert, T. Bettingerb, F. Yanb, and R. H. Guy. Plasma membrane poration induced by ultrasound exposure: Implication for drug delivery. *Journal of Controlled Release*, 104:213–222, 2005.

F. Mekki-Berrada, P. Thibault, and P. Marmottant. Acoustic pulsation of a microbubble confined between elastic walls. *Phys. Fluids*, 28:032004, 2016.

M. Minnaert. Xvi. on musical air-bubbles and the sounds of running water. In *15th International Conference on Miniaturized Systems for Chemistry and Life Sciences*, volume 16.104, pages 235–248, 1933.

M. Miyamoto, S. Ueyama, N. Hinomoto, T. Saitoh, S. Maekawa, and J. Hirotsuji. Degreasing of solid surfaces by microbubble cleaning. *Jpn. J. Appl. Phys.*, 46:1236, 2007.

S. Moosavi Nejad, H. Hosseini, H. Akiyama, and K. Tachibana. Reparable cell sonoporation in suspension: theranostic potential of microbubble. *Theranostics*, 6:446–455, 2016.

R. Nabergoj and A. Francescutto. On thresholds for surface waves on resonant bubbles. *Journal de Physique*, 40(C8):306–309, 1979.

A. Nakeff and D. P. Floeh. Separation of megakaryocytes from mouse bone marrow by density gradient centrifugation. *Blood*, 48:133–138, 1976.

X. Noblin, A. Buguin, and F. Brochard-Wyart. Vibrations of sessile drops. *Eur. Phys. J. Special Topics*, 166:7–10, 2009.

B. E. Noltingk and E. A. Neppiras. Cavitation produced by ultrasonics. *Proc. Phys. Soc. Lond.*, 63:674–685, 1950.

W. L. Nyborg. Acoustic streaming near a boundary. *J. Acoust. Soc. Am.*, 30:329–339, 1958.

K. Okada, N. Kudo, K. Niwa, and K. Yamamoto. A basic study on sonoporation with microbubbles exposed to pulsed ultrasound. *Journal of Medical Ultrasonics*, 32:3–11, 2005.

M. S. Ozdas, A. S. Shah, P. M. Johnson, N. Patel, M. Marks, T. Baran Yasar, U. Stalder, L. Bigler, W. von der Behrens, S. R. Sirsi, and M. Fatih Yanik. Non-invasive molecularly-specific millimeter- resolution manipulation of brain circuits by ultrasound-mediated aggregation and uncaging of drug carriers. *Nature communications*, 11:4929, 2020.

M. S. Plesset. On the stability of fluid flows with spherical symmetry. *Journal of Applied Physics*, 25:96–98, 1954.

M. W. Plesset. The dynamics of cavitation bubbles. *Journal of Applied Mechanics*, 16: 277–282, 1949.

A. Pommella, N. J. Brooks, J. M. Seddon, and V. Garbin. Selective flow-induced vesicle rupture to sort by membrane mechanical properties. *Scientific Reports*, 5:13163, 2015.

C. Poon. Measuring the density and viscosity of culture media for optimized computational fluid dynamics analysis of in vitro devices. *bioRxiv*, 2020.

H. Poritsky. The collapse or growth of a spherical bubble in a viscous fluid. *Proc. of the First U.S. Nat. Congr. Appl. Mech.*, 5116:813–821, 1951.

M. Postema and A. Bouakaz. Acoustic bubbles in therapy: Recent advances with medical microbubbles, clouds, and harmonic antibubbles. *Elsevier*, 140:150–152, 2018.

M. Postema and G. Schmitz. Bubble dynamics involved in ultrasonic imaging. *Expert Rev. Mol. Diagn.*, 6:493–502, 2006.

F. Prabowo and C.-D. Ohl. Surface oscillation and jetting from surface attached acoustic driven bubbles. *Ultrasonics Sonochemistry*, 18:431–435, 2011.

A. Prosperetti. Bubble-related ambient noie in the ocean. *J. Acoust. Soc. Am.*, 84: 1042–1054, 1988.

A. Prosperetti. Linear oscillations of constrained drops, bubbles, and plane liquid surfaces. *Phys. Fluids*, 24:032109, 2012.

A. Prosperetti. Vapor bubbles. *Annual review of Fluid Mechanics*, 49:221–248, 2017.

P. Qin, Y. Lin, L. Jin, L. Du, and A. C. H. Yu. Impact of microbubble-to-cell parameters on heterogeneous sonoporation at the single-cell level. page 10.1109, 2015.

J. Rapet, Y. Tagawa, and C.-D. Ohl. Shear-wave generation from cavitation in soft solids. *Applied Physics Letters*, 114:123702, 2019.

L. Rayleigh. On the circulation of air observed in kundt's tubes, and on some allied acoustical problems. *Phil. Trans. R. Soc. Lond.*, 175:1–21, 1884.

L. Rayleigh. On the pressure developed in a liquid during the collapse of a spherical cavity. *Philosophical Magazine*, 34:94–98, 1917.

F. Reuter and R. Mettin. Mechanisms of single bubble cleaning. *Ultrasonics Sonochemistry*, 29:550–562, 2016.

A. Sarvazyan, T. J. Hall, M. W. Urban, M. Fatemi, S. R. Aglyamov, and B. S. Garra. An overview of elastography - an emerging branch of medical imaging. *Curr. Med. Imaging Rev.*, 7:255–282, 2011.

J. Schindelin, I. Arganda-Carreras, E. Frise, V. Kaynig, M. Longair, T. Pietzsch, S. Preibisch, C. Rueden, S. Saalfeld, B. Schmid, J.-Y. Tinevez, D. J. White, V. Hartenstein, K. Eliceiri, P. Tomancak, and A. Cardona. Fiji: an open-source platform for biological-image analysis. *Nature Methods*, 9:676–682, 2012.

C. A. Schneider, W. S. Rasban, and K. W. Eliceiri. Nih image to imagej: 25 years of image analysis. *Nature Methods*, 9:671–675, 2012.

T. Segers, N. de Jong, D. Lohse, and M. Versluis. *Microfluidics for medical applications. Chapter 5. Microbubbles for medical applications.* Albert van den Berg, Loes Segerink, 2015.

S. J. Shaw. Nonspherical sub-millimeter gas bubble oscillations: Parametric forcing and nonlinear shape mode coupling. *Physics of Fluids*, 29:122103, 2017.

S. Shklyaev and A. V. Straube. Linear oscillations of a compressible hemispherical bubble on a solid substrate. *Phys. Fluids*, 20:052102, 2008.

T. A. Spelman and E. Lauga. Arbitrary axisymmetric steady streaming: flow, force and propulsion. *Journal of Engineering Mathematics*, 105:31–65, 2017.

P.V.R. Suryanarayana and Y. Bayazitoglu. Effect of static deformation and external forces on the oscillations of levitated droplets. *Phys. Fluids A*, 3(5):967–977, 1991.

Sutter Instrument. *Pipette Cookbook.* Sutter Instrument, 2018.

Y. Tagawa and I. R. Peters. Bubble collapse and jet formation in corner geometries. *Physical Review Fluids*, 3:081601, 2018.

Y. Tagawa, S. Yamamoto, K. Hayasaka, and M. Kameda. On the pressure impulse of a laser-induced underwater shock wave. *Journal of Fluid Mechanics*, 808:5–18, 2016.

T. Tandiono, E. Klaseboer, S.-W. Ohl, D. Siak-Wei Ow, A. Boon-Hwa Choo, F. Li, and Claus-Dieter Ohl. Resonant stretching of cells and other elastic objects from transient cavitation. *Soft matter*, 9:8687–8696, 2013.

P. Tho, R. Manasseh, and A. Ooi. Cavitation microstreaming patterns in single and multiple bubble systems. *J. Fluid Mech.*, 576:191–233, 2007.

J.-Y. Tinevez, N. Perry, J. Schindelin, G. M. Hoopes, G. D. Reynolds, E. Laplantine, S. Y. Bednarek, S. L. Shorte, and K. W. Eliceiri. Trackmate: An open and extensible platform for single-particle tracking. *Methods*, 115:80–90, 2017.

T. A. Tran, J.-Y. Le Guennec, P. Bougnoux, F. Tranquart, and A. Bouakaz. Characterization of cell membrane response to ultrasound activated microbubbles. *IEEE transactions on ultrasonics, ferroelectrics, and frequency control*, 55:44–49, 2008.

C. Tropea, A. L. Yarin, and J. F. Foss. *Handbook of Experimental Fluid Mechanics.* Springer, 2007.

B. van Elburg, G. Collado Lara, G.-W. Bruggert, T. Segers, M. Versluis, and G. Lajoinie. Feedback-controlled microbubble generator producing 1×10 6 monodisperse bubbles per second. *Review of Scientific Instruments*, 93:035110, 2021.

A. van Wamel, A. Bouakaz, F. ten Cate, and Nico de Jong. Effects of diagnostic ultrasound parameters on molecular uptake and cell viability. October 2002.

A. van Wamel, A. Bouakaz, M. Versluis, and N. de Jong. Micromanipulation of endothelial cells: ultrasound-microbubble-cell interaction. *Ultrasound in Medicine and Biology*, 30: 1255–1258, 2004.

A. van Wamel, K. Kooiman, M. Harteveld, M. Emmer, F. ten Cate, M. Versluis, and N. de Jong. Vibrating microbubbles poking individual cells: drug transfer into cells via sonoporation. *Journal of Controlled Release*, 112:149–155, 2006.

M. Versluis, D.E. Goertz, P. Palanchon, I.L. Heitman, S.M. van der Meer, B. Dollet, N. de Jong, and D. Lohse. Microbubble shape oscillations excited through ultrasonic parametric driving. *Physical Review E*, 82:026321, 2010.

H. J. Vos, B. Dollet, M. Versluis, and N. de Jong. Nonspherical shape oscillations of coated microbubbles in contact with a wall. *Ultrasound in Med. & Biol.*, 37(6):935–948, 2011.

M. Wang, Y. Zhang, C. Cai, J. Tu, X. Guo, and D. Zhang. Sonoporation-induced cell membrane permeabilization and cytoskeleton disassembly at varied acoustic and microbubble-cell parameters. *Scientific Reports*, 8:3885, 2018.

X. Xi, F. Cegla, R. Mettin, F. Holsteyns, and A. Lippert. Study of non-spherical bubble oscillations near a surface in a weak acoustic standing wave field. *J. Acoust. Soc. Am.*, 135(4):1731–1741, 2014.

Y. Xie, N. Nama, P. Li, Z. Mao, P.-H. Huang, C. Zhao, F. Costanzo, and T. Jun Huang. Probing cell deformability via acoustically actuated bubbles. *Small*, 12:902–910, 2016.

H. Yu and S. Chen. A model to calculate microstreaming-shear stress generated by oscillating microbubbles on the cell membrane in sonoporation. *Bio-medical materials and engineering*, 24:861–868, 2014.

Y. Zhou, R. E. Kumon, J. Cui, and C. X. Deng. The size of sonoporation pores on the cell membrane. *Ultrasound Med Biol.*, 35:1756–1760, 2009.

Y. Zhou, K. Yang, J. Cui, J. Y. Ye, and C. X. Deng. Controlled permeation of cell membrane by single bubble acoustic cavitation. *Journal of Controlled Release*, 157: 103–111, 2012.

P. V. Zinin and J. S. Allen. Deformation of biological cells in the acoustic field of an oscillating bubble. *Physical Review E*, 79:021910, 2009.

Scientific publications and communications

Publications

- M. Fauconnier, C. Mauger, J.-C. Béra and C. Inserra, Nonspherical dynamics and microstreaming of a wall- attached microbubble;;k, *Journal of Fluid Mechanics*, (accepted).
- M. Fauconnier, J. Ngo, J.-C. Béra and C. Inserra, Mechanical response of a megakaryocyte acoustically coupled with a tethered microbubble, Forum Acusticum, December 2020, Lyon, France, pp.1085-1087.
- M. Fauconnier, J.-C. Béra and C. Inserra, Nonspherical modes nondegeneracy of a tethered bubble, *Physical Review E* **102**(3), 033108, 2020.
- M. Fauconnier, J.-C. Béra and C. Inserra, Dynamics of a wall-attached bubble undergoing asymmetric oscillations, *Proceedings of Meetings on Acoustics* **38**(1), 020011, 2019.

Oral communications

- Microstreaming induced by a nonspherical bubble attached to a wall. *6 ^{e} Journées Scientifiques Ultrasons et Procédés*, 5-7 July 2021, Lille, France.
- Experimental investigation of fluid flows induced by aspherical bubbles. *11th International Symposium on Cavitation Acusticum*, 10-13 May 2021, Daejeon, Korea (virtual conference).
- Deformation of megakaryocytes mechanically coupled with an ultrasound-driven microbubble. *Forum Acusticum*, 7-11 December 2020, Lyon, France (virtual conference).
- Dynamics of a wall-attached bubble undergoing asymmetric oscillations. *International Congress on Ultrasonics*, 3-6 September 2019, Bruges, Belgique.
- Dynamique de microbulles sur substrat et interaction bulle-cellule dans un champ ultrasonore. *5 ^{e} Journées Scientifiques Ultrasons et Procédés*, 19-21 May 2019, Orange, France.

Poster

- Micro-scale bubble-cell interaction under an acoustic field. *8th biennal European Cell Mechanics Meeting*, 3-6 June 2019, Italy, Milan.

Awards

- EAA Best Applied Contribution Award awarded during the 2020 Forum Acusticum for the oral presentation entitled “Deformations of megakaryocytes mechanically coupled with an ultrasound-driven microbubble”.
- Premier Prix du Jury of scientific Game Jam 2020, organized by Lyon Game Dev, and awarded for the development of the science-themed video game “Sonobulle”.
- R.W.B. Stephens Prize - Honorable Mention, awarded during the 2019 International Congress on Ultrasonics for the oral presentation entitled “Dynamics of a wall-attached bubble undergoing asymmetric oscillations”.

Abstract

Sources of significant acoustic, mechanical and thermal effects, gas microbubbles are widely used for industrial and medical purposes. Among others, the acoustic oscillation of microbubbles make it possible to internalize products in living cells, which opens the way to numerous therapeutic applications. Large amplitude oscillatory regimes necessary for there to be a significant interaction with cells can be synonymous with the appearance of instability of the bubble interface and of the so-called nonspherical modes of bubble oscillation, but also to bubble collapse and cell destruction. It seems therefore necessary to control their dynamics in order to minimize the harmful effects and maximize the therapeutic action.

With the view to study the action of the oscillating bubble at the cellular level, this thesis manuscript presents an experimental work in three stages. First, the oscillatory dynamics of a single bubble attached to a wall is studied, in particular through the conditions for the appearance of its nonspherical modes. Second, the appearance of fluid flows, also called microstreaming, induced by such a nonspherical bubble is analyzed on the basis of a quantitative description of its interface. Lastly, this knowledge acquired on an oscillating bubble is transposed to the configuration of a bubble-cell pair. The bubble-induced mechanical effects that apply on the cell are assessed at both the acoustic and the fluidic time scales.

Keywords: ultrasound, microbubble, nonspherical modes, modal nondegeneracy, microstreaming, sonoporation, bubble-cell interaction.

Résumé

Sources d’effets acoustiques, mécaniques et thermiques importants, les microbulles de gaz sont largement utilisées à des fins industrielles et médicales. Entre autres, l’oscillation acoustique des microbulles permet d’internaliser des produits dans des cellules vivantes, ce qui ouvre la voie à de nombreuses applications thérapeutiques. Les régimes oscillatoires de grande amplitude nécessaires pour qu’il y ait une interaction significative avec les cellules peuvent être synonymes d’apparition d’instabilité de l’interface bulle et de modes dits non-sphériques d’oscillation de bulle, mais aussi d’implosion de bulle et de destruction cellulaire. Il semble donc nécessaire de contrôler leur dynamique afin de minimiser les effets néfastes et de maximiser l’action thérapeutique.

Dans l’optique d’étudier l’action de la bulle oscillante à l’échelle cellulaire, ce manuscrit de thèse présente un travail expérimental en trois temps. Premièrement, la dynamique oscillatoire d’une bulle unique accrochée à une paroi est étudiée, notamment au travers des conditions d’apparition de ses modes non-sphériques. Dans un deuxième temps, les écoulements fluides, également appelés microstreaming, induits par une telle bulle non-sphérique sont analysés à partir d’une description quantitative de l’interface de bulle. Enfin, cette connaissance acquise sur une bulle oscillante est transposée à la configuration d’un couple bulle-cellule. Ces effets mécaniques induits s’appliquant sur une cellule à proximité sont analysés à la fois aux échelles de temps acoustique et fluidique.

Mot-clés: ultrasons, micro-bulle, modes non-sphériques, non-dégénérescence modale, microstreaming, sonoporation, interaction bulle-cellule.